



ScuDo

Scuola di Dottorato ~ Doctoral School
WHAT YOU ARE, TAKES YOU FAR

Doctoral Dissertation
Doctoral Program in Structural Engineering (29th Cycle)

Ductility of lightly reinforced and fiber-reinforced concrete elements: A unified approach

By

Andrea Gorino

Supervisors:

Prof. Bernardino Chiaia, Supervisor
Prof. Alessandro P. Fantilli, Co-Supervisor

Doctoral Examination Committee:

Prof. Joaquim A.O. Barros, Referee, Universidade do Minho
Prof. Pietro Cornetti, Member, Politecnico di Torino
Prof. Alberto Meda, Member, Università degli Studi di Roma Tor Vergata
Prof. Fausto Minelli, Referee, Università degli Studi di Brescia
Dr. Francesco Tondolo, Member, Politecnico di Torino

Politecnico di Torino
2017

Declaration

I hereby declare that, the contents and organization of this dissertation constitute my own original work and does not compromise in any way the rights of third parties, including those relating to the security of personal data.

Andrea Gorino

2017

* This dissertation is presented in partial fulfillment of the requirements for **Ph.D. degree** in the Graduate School of Politecnico di Torino (ScuDo).

Questa tesi è dedicata a Claudia, la più bella scoperta del mio Dottorato

Ringraziamenti

Voglio ringraziare i miei genitori, Anna Maria ed Aldo, per la guida, il sostegno, l'esempio che sono sempre stati per me, e Paolo per l'allegria e la spensieratezza che porta quotidianamente in famiglia. Grazie a Claudia per ogni giorno condiviso con me, e per tutti i giorni che verranno e che vorremo continuare a condividere. E ancora, grazie a tutti i familiari e gli amici che mi sono stati vicini, durante il percorso del Dottorato di Ricerca e da sempre.

Ringrazio quindi il Prof. Bernardino Chiaia ed il Prof. Alessandro Fantilli per le opportunità che mi hanno voluto dare sin dagli anni della Laurea e della Laurea Magistrale, nonché per il continuo supporto alla mia attività di ricerca durante il Dottorato. Ringrazio altresì Cemex Research Group per la preziosa collaborazione alla conduzione della campagna sperimentale sulle travi di calcestruzzo a rinforzo ibrido. Voglio infine ringraziare la mia Azienda, Rete Ferroviaria Italiana, per avermi scelto per intraprendere un nuovo percorso, al termine del Dottorato di Ricerca che si conclude con questa tesi.

Sommario

Gli elementi inflessi di calcestruzzo debolmente armato (LRC), fibro-rinforzato (FRC) ed a rinforzo ibrido (HRC) mostrano un comportamento simile, funzione della quantità di armatura e/o di fibre presente nella matrice cementizia, quando sono soggetti ad azioni statiche. Infatti, se non viene previsto un idoneo rinforzo, all'atto della fessurazione del calcestruzzo si giunge alla rottura fragile. Nella presente tesi di Dottorato si introduce, quindi, un nuovo approccio unificato per la valutazione della minima quantità di rinforzo a fini statici per gli elementi inflessi di calcestruzzo. Tale approccio si basa sulla definizione dell'indice di duttilità (DI), che è funzione della differenza tra il carico ultimo e quello di fessurazione efficace. Pertanto, DI assume valori positivi per gli elementi debolmente rinforzati aventi risposta duttile, mentre è negativo in caso di comportamento fragile.

Mediante tre modelli generali per gli elementi LRC, FRC e HRC, viene descritta la risposta flessionale di travi di calcestruzzo debolmente rinforzato con barre di armatura, fibre o loro combinazioni, al fine di studiare la transizione fragile/duttile (ovvero il minimo rinforzo). Inoltre, vengono considerati i risultati di sperimentazioni disponibili in letteratura, così come di una specifica campagna di prove. Sia i risultati numerici che quelli sperimentali rivelano l'esistenza di un fuso, valido in generale, che esprime la variazione dell'indice DI al variare del rinforzo in un elemento di calcestruzzo. Si propone, dunque, una procedura di progettazione, assistita da sperimentazione, per determinare il minimo rinforzo di una trave LRC e/o FRC, il quale comporta l'annullamento dell'indice DI . Il minimo rinforzo di un elemento HRC è, invece, una combinazione lineare delle corrispondenti minime quantità di sole barre di armatura e di sole fibre.

L'approccio proposto è adottato per progettare la minima quantità di rinforzo da disporre nei segmenti di calcestruzzo prefabbricato per il rivestimento di una galleria. Esso è applicato ad elementi presso-inflessi LRC, FRC e HRC. L'indice DI è altresì utilizzato come parametro di riferimento in uno studio di sostenibilità semplificato. In altre parole, mediante un'analisi combinata, vengono quantificate le prestazioni ecologiche e meccaniche di piastre unidirezionali di calcestruzzo leggero fibro-rinforzato, adottando un approccio integrato di tipo olistico.

Abstract

Lightly Reinforced Concrete (LRC), Fiber-Reinforced Concrete (FRC), and Hybrid Reinforced Concrete (HRC) elements subjected to static bending actions exhibit a similar behavior, which depends on the amount of rebar and/or fibers added to the cementitious matrix. In all the cases, if a suitable reinforcing system is not provided, the brittle failure occurs at the cracking of concrete. Hence, a new and unified approach is introduced in the present thesis to evaluate the minimum reinforcement for static reasons. Such approach is based on the definition of the ductility index (DI), which is a function of the difference between the ultimate load and the effective cracking load. Therefore, DI is higher than zero when a lightly reinforced member shows a ductile response, whereas it is negative in case of brittle behavior.

To study the brittle/ductile transition (i.e., the minimum reinforcement), the flexural behavior of concrete beams containing low amounts of rebar, fibers, or a combination, is predicted through three general models for LRC, FRC, and HRC members. In addition, test results coming from the available literature and a specific experimental campaign are considered. Both numerical and experimental data reveal the existence of a generally valid linear envelope of DI when the reinforcement varies in a concrete member. Based on these results, a design-by-testing procedure can be established for determining the minimum reinforcement of a LRC and/or FRC element, which corresponds to DI equal to zero. Moreover, the minimum reinforcement of an HRC element is defined by any linear combination of the associated minimum amounts of sole rebar and fibers.

The proposed approach is adopted to design the minimum reinforcement of precast concrete segments for a tunnel lining. It is applied to LRC, FRC, and HRC members, not only subjected to pure flexure but also under combined axial force and bending moment. Finally, the ductility index is used as functional unit of a simplified sustainability analysis. In the specific case of lightweight FRC one-way plates, this new parameter allows to measure the performances of the concrete elements in combined ecological and mechanical analyses, with an integrated holistic approach.

Contents

1. Introduction.....	1
1.1 New trends in concrete industry	1
1.2 State-of-the-art.....	2
1.2.1 Lightly reinforced concrete beams.....	3
1.2.2 Fiber-reinforced concrete beams	5
1.2.3 Hybrid reinforced concrete beams	8
1.3 Proposed approach.....	9
1.4 Research significance	11
2. Minimum area of rebar in LRC beams	13
2.1 Simplified model for LRC beams in bending.....	13
2.2 General model for LRC beams in bending.....	15
2.2.1 Formulation of the problem	15
2.2.2 Material behavior	19
2.2.3 Numerical solution of the problem	21
2.3 Analysis of the numerical results	24
2.4 Comparison with the experimental results	28
2.5 Discussion of the results	33
3. Minimum fiber volume fraction in FRC beams.....	35
3.1 Simplified model for FRC beams in bending.....	35
3.2 General model for FRC beams in bending.....	37
3.2.1 Modelling the fiber pull-out.....	37

3.2.2 Numerical evaluation of the fiber pull-out	41
3.2.3 Modelling the flexural response of FRC beams	44
3.2.4 Numerical evaluation of the flexural response of FRC beams	46
3.3 Analysis of the numerical results	47
3.4 Comparison with the experimental results	52
3.5 Discussion of the results	59
4. Minimum hybrid reinforcement in HRC beams	61
4.1 Simplified model for HRC beams in bending	61
4.2 General model for HRC beams in bending	64
4.3 Analysis of the numerical results	66
4.4 Experimental campaign	74
4.4.1 Materials	74
4.4.2 Specimens	75
4.4.3 Test set-up	75
4.4.4 Experimental results	76
4.5 Comparison with the experimental results	82
4.6 Discussion of the results	90
5. A new and unified approach for concrete beams	95
5.1 General envelope for concrete beams	95
5.2 Three-dimensional interpretation of the proposed approach	98
5.3 Practical application of the proposed approach	101
6. Minimum reinforcement of concrete segments for tunnel linings	105
6.1 Introduction	105
6.2 Concrete segments of the Brenner Base Tunnel	107
6.3 Modelling the flexural behavior of BBT segments	108
6.3.1 LRC segment	109
6.3.2 FRC segment	110
6.4 Minimum reinforcement of concrete segments	111

6.5	Modelling the flexural behavior of HRC segments.....	112
6.6	HRC segments under axial and bending actions	114
6.6.1	Modelling the concrete lining in final conditions	114
6.6.2	Evaluating the interaction diagram of lining cross-sections.....	116
6.7	Discussion of the results	121
7.	Ductility index as functional unit in ecological and mechanical analyses.....	125
7.1	Introduction	125
7.2	Experimental campaign	127
7.2.1	Materials	127
7.2.2	Test set-up.....	128
7.3	Experimental results	129
7.3.1	Uniaxial compression tests	129
7.3.2	Three point bending tests	132
7.4	Comparative analyses	134
7.4.1	Analysis at the material level.....	134
7.4.2	Analysis at the structural level.....	135
7.4.3	Combined ecological and mechanical assessment.....	135
7.5	Discussion of the results	138
8.	Conclusions.....	139
8.1	Final considerations	139
8.2	Further researches.....	142
	References.....	145
	Notations.....	160

List of Figures

Figure 1.1: Flexural behavior of concrete beams (Ruiz et al. 1999): (a) three point bending test; (b) load vs. midspan deflection curves.....	3
Figure 1.2: Ideal load vs. deflection curve suggested by Model Code 2010 (<i>fib</i> 2012a) to measure the ductility of FRC members in the absence of conventional reinforcement.	7
Figure 1.3: Linear approximation of the $DI - r$ relationships.	11
Figure 2.1: Simplified state of stress in a LRC cross-section at ultimate limit state.	14
Figure 2.2: $DI - r$ linear function for LRC beams.....	15
Figure 2.3: General model for LRC beams in bending failing in presence of a single crack: (a) portion of the beam; (b) slips between rebar and concrete in tension; (c) strains of rebar and surrounding concrete; (d) bending moment.	16
Figure 2.4: State of strain and stress at boundaries of the analyzed portion of LRC beam: (a) cracked cross-section 0-0; (b) Stage I cross-section 1-1.....	18
Figure 2.5: Stress vs. strain constitutive relationships of materials (<i>fib</i> 2012a): (a) ascending branch of the Sargin's parabola for concrete in compression, and linear elastic law for uncracked concrete in tension; (b) elastic-perfectly plastic law for steel rebar.	21
Figure 2.6: Stresses on the crack surface and at the interface between rebar and concrete in tension according to Model Code 2010 (<i>fib</i> 2012a): (a) stress vs. crack width relationship; (b) bond-slip model.....	21
Figure 2.7: Flow-chart of the numerical procedure.....	22
Figure 2.8: Ideal LRC beam in three point bending.....	24
Figure 2.9: Application of the general model to the ideal beams of Group L_9: (a) $M - \bar{w}$ curves; (b) $DI - A_s$ relationship and evaluation of $A_{s,min}$	25

Figure 2.10: Proposed $DI - r$ linear relationship [Eq.(2.4)] in comparison with the results of the general model.	28
Figure 2.11: $DI - A_s$ relationships and evaluation of $A_{s,min}$ in LRC beams tested in some experimental campaigns: (a) beams of Group L_III tested by Bosco et al. (1990); (b) beams of Group L_IX tested by Carpinteri (1989).	32
Figure 2.12: Proposed $DI - r$ linear relationship [Eq.(2.4)] in comparison with the results of some experimental campaigns.	32
Figure 3.1: Simplified state of stress in a FRC cross-section at ultimate limit state.	36
Figure 3.2: $DI - r$ linear function for FRC beams.	37
Figure 3.3: Modeling the fiber pull-out: (a) portion of the ideal tie composed by a straight fiber and the surrounding cementitious matrix in presence of a single crack; (b) slip between fiber and matrix; (c) strains in fiber and matrix.	39
Figure 3.4: Stresses on the crack surface and at the interface between fiber and matrix: (a) fictitious crack model proposed by Model Code 2010 (<i>fib</i> 2012a); (b) bond-slip model proposed by Fantilli and Vallini (2003).	41
Figure 3.5: Flow-chart of the numerical procedure for evaluating the fiber pull-out.	42
Figure 3.6: Stresses of FRC in tension: (a) linear elastic stage; (b) cracked stage.	45
Figure 3.7: Modeling FRC beams in three point bending: (a) portion of the beam; (b) cross-section of the beam; (c) strain profile in midsection; (d) bending moment.	45
Figure 3.8: Complete stress <i>vs.</i> strain relationship of FRC.	46
Figure 3.9: Flow-chart of the numerical procedure for evaluating the flexural response of FRC beams.	47
Figure 3.10: Application of the general model to the ideal beams of Group F_6: (a) $M - \bar{w}$ curves; (b) $DI - V_f$ relationship and evaluation of $V_{f,min}$	51
Figure 3.11: Proposed $DI - r$ linear relationship [Eq.(3.4)] in comparison with the results of the general model.	52
Figure 3.12: $DI - V_f$ relationships and evaluation of $V_{f,min}$ in FRC beams tested in some experimental campaigns: (a) beams of Group F_VI tested by Banthia and Gupta (2004); (b) beams of Group F_VII tested by Barros et al. (2005).	57

Figure 3.13: Proposed $DI - r$ linear relationship [Eq.(3.4)] in comparison with the results of some experimental campaigns.	59
Figure 4.1: Experimental investigation performed by Falkner and Henke (2005): (a) four point bending test; (b) applied load vs. midspan deflection curves of FRC beam (i), LRC beam (ii), HRC beam (iii), and difference (iv) = (iii) - (ii).	62
Figure 4.2: Simplified state of stress in an HRC cross-section at ultimate limit state.	63
Figure 4.3: $DI - r$ envelope for HRC beams.	64
Figure 4.4: General model for predicting the flexural response of HRC beams: (a) ideal tie representing the cracked FRC; (b) $\sigma_c - w$ relationship of FRC; (c) HRC beam in three point bending in presence of a single crack; (d) $M - \bar{w}$ curve of an HRC beam in bending.....	65
Figure 4.5: Application of the general model: (a) $M - \bar{w}$ curves of the beams of Group H_9; (b) $DI - r$ relationship of Group H_9; (c) $M - \bar{w}$ curves of the beams of Group H_10; (d) $DI - r$ relationship of Group H_10.....	70
Figure 4.6: Proposed $DI - r$ envelope [Eqs.(4.4)] in comparison with the results of the general model.	74
Figure 4.7: Three point bending test on un-notched prismatic specimen.	76
Figure 4.8: Load vs. deflection curves from three point bending tests.	81
Figure 4.9: Proposed $DI - r$ envelope [Eqs.(4.4)] in comparison with the results of some experimental campaigns.	88
Figure 4.10: Eq.(4.5) for combining rebar and fibers in order to attain the condition of minimum ductility (i.e., $DI = 0$).	92
Figure 5.1: $DI - r$ envelope for concrete beams.	96
Figure 5.2: Comparison between the proposed $DI - r$ envelope for concrete members and the numerical results referred to 198 LRC, FRC, and HRC beams (Table 2.2, Table 3.2, and Table 4.2, respectively).	97
Figure 5.3: Comparison between the proposed $DI - r$ envelope for concrete members and the experimental results referred to 136 LRC, FRC, and HRC beams (Table 2.4, Table 3.5, and Tables 4.7-8, respectively).	97
Figure 5.4: Proposed plane in the $DI - A_s / A_{s,min} - V_f / V_{f,min}$ space [Eq.(5.3)]. .	99

Figure 5.5: Projection of the proposed plane [i.e., Eq.(5.3)] along the bisecting surface of the $DI-A_s/A_{s,min} - V_f/V_{f,min}$ space [i.e., $A_s/A_{s,min} = V_f/V_{f,min}$], in comparison with the numerical results referred to 198 LRC, FRC, and HRC beams (Table 2.2, Table 3.2, and Table 4.2, respectively).	100
Figure 5.6: Projection of the proposed plane [i.e., Eq.(5.3)] along the bisecting surface of the $DI-A_s/A_{s,min} - V_f/V_{f,min}$ space [i.e., $A_s/A_{s,min} = V_f/V_{f,min}$], in comparison with the experimental results referred to 136 LRC, FRC, and HRC beams (Table 2.4, Table 3.5, and Tables 4.7-8, respectively).	101
Figure 5.7: $DI - r$ design relationships for concrete beams.....	103
Figure 6.1: Ring of a precast concrete lining.	106
Figure 6.2: Three point bending test on a precast concrete segment (Caratelli et al. 2011): (a) test set-up; (b) applied load vs. crack width curve.	108
Figure 6.3: Numerical predictions of the $P - \bar{w}$ flexural response referred to two concrete segments in comparison with the experimental curves obtained by Caratelli et al. (2011): (a) LRC segment; (b) FRC segment.	110
Figure 6.4: Numerical predictions of the $P - \bar{w}$ flexural response referred to two ideal concrete segments at brittle/ductile transition, in comparison with the numerical curves reproducing the test results of Caratelli et al. (2011): (a) LRC segments; (b) FRC segments.	113
Figure 6.5: Minimum reinforcement in HRC segments: (a) Eq.(4.5) for combining rebar and fibers; (b) numerical predictions of the $P - \bar{w}$ flexural response of three ideal HRC segments at brittle/ductile transition.....	113
Figure 6.6: Structural analysis of the concrete lining in final conditions: (a) finite element model; (b) axial force; (c) bending moment.	115
Figure 6.7: Evaluation of interaction diagrams: (a) concrete cross-section; (b) limit state configurations.	117
Figure 6.8: Interaction diagrams referred to the LRC and FRC segments compared with the internal actions in final conditions.	119
Figure 6.9: Interaction diagrams referred to the ideal concrete segments at brittle/ductile transition, compared with the internal actions in final conditions.	120
Figure 6.10: Efficiency index of fiber-reinforcement (Fantilli et al. 2016d) as a function of the axial force referred to the ideal concrete segments at brittle/ductile transition.....	121

Figure 6.11: Flow-chart of the proposed procedure for evaluating the optimal hybrid reinforcement in an HRC member.	122
Figure 7.1: Experimental campaign on the six lightweight mixtures: (a) uniaxial compression tests; (b) three point bending tests.	129
Figure 7.2: Stress vs. strain curves obtained from uniaxial compression tests: (a)-(c) TLC mixtures; (d)-(f) RLC mixtures.....	130
Figure 7.3: Load-deflection curves obtained from the three point bending tests: (a)-(c) TLC plates; (d)-(f) RLC plates.....	133
Figure 7.4: Average values of ductility index as a function of the amount of fibers and evaluation of the minimum fiber volume fraction: (a) TLC plates; (b) RLC plates.	134
Figure 7.5: Results of combined ecological and mechanical analyses of TLC and RLC: (a) at material scale with $MI = MI_1$; (b) at structural scale with $MI = MI_2$	137

List of Tables

Table 2.1: Geometrical and mechanical properties of 36 ideal LRC beams...	26
Table 2.2: Evaluation of minimum reinforcement in 36 ideal LRC beams. ...	27
Table 2.3: Geometrical and mechanical properties of 50 LRC beams tested by other Authors.	29
Table 2.4: Evaluation of minimum reinforcement in 50 LRC beams tested by other Authors.	30
Table 3.1: Geometrical and mechanical properties of 54 ideal FRC beams...	48
Table 3.2: Evaluation of minimum reinforcement in 54 ideal FRC beams. ...	50
Table 3.3: Geometrical and mechanical properties of 61 FRC beams tested by other Authors.	53
Table 3.4: Geometrical and mechanical properties of the fiber used in 61 beams tested by other Authors.	55
Table 3.5: Evaluation of minimum reinforcement in 61 FRC beams tested in some experimental campaigns available in literature.	57
Table 4.1: Geometrical and mechanical properties of 108 ideal HRC beams.	67
Table 4.2: Evaluation of minimum reinforcement in 108 ideal HRC beams..	71
Table 4.3: Materials contained in 1 m ³ of the concrete mixtures.....	75
Table 4.4: Amounts of rebar and fibers used to reinforce the tested beams. ...	76
Table 4.5: Geometrical and concrete properties of 54 concrete beams.	83
Table 4.6: Rebar and fibers used in 54 concrete beams.	85
Table 4.7: Evaluation of the ductility index in 54 concrete beams.	87
Table 4.8: Evaluation of the minimum reinforcement in 54 concrete beams.	89

Table 6.1: Experimental and numerical values of effective cracking load and ultimate load, and numerical values of ductility index, referred to concrete segments reinforced with different amounts of rebar and/or fibers.....	111
Table 7.1: Material components referred to 1 m ³ of TLC.....	128
Table 7.2: Material components referred to 1 m ³ of RLC.	128
Table 7.3: Average values of the concrete parameters obtained with the uniaxial compression tests.	131
Table 7.4: Average values of the structural parameters obtained with the three point bending tests on one-way plates.	132
Table 7.5: Environmental impact referred to 1 kg of concrete components.	136
Table 7.6: Ecological and mechanical indexes of the six lightweight concretes.	137

Chapter 1

Introduction

1.1 New trends in concrete industry

Among the innovative challenges nowadays involving the construction industry, resilience and sustainability play an important role (ACI 2016, WEF 2016). The concept of resilience is usually related to the occurrence of extreme events (e.g., earthquakes, flooding, hurricanes, etc.) during the life-cycle of a structure. In such situations, losses should be minimized through the attainment of an enhanced robustness, and more effective recovery strategies as well. On the other hand, environmental, economic, and social aspects are combined in the general concept of sustainability, with the aim of optimizing the use of natural resources (Bocchini et al. 2014). The increasing importance assumed by resilience and sustainability is due to several reasons. Among the others, a larger number of extreme events occurs nowadays with respect to the past, and the construction industry is globally the first consumer of raw materials (WEF 2016).

In the specific case of concrete structures, the central topic for both resilience and sustainability is represented by the problem of cracking (ACI 2016), because of the quasi-brittle nature of the cement-based materials (Bažant and Planas 1998, de Borst 2002, Shah et al. 1995). As a matter of fact, in the absence of suitable reinforcing systems, these materials typically shows a sudden failure, which is incompatible with the required resilience (ACI 2014, CEN 2004a, *fib* 2012a). Moreover, it is well known that crack propagation in serviceability conditions and corrosion of steel rebar are strictly related in conventionally reinforced concrete

structures (Alonso et al. 1998, Giordano and Tondolo 2011, Vidal et al. 2004). Hence, also the durability of such common structures is affected by concrete cracking, and their sustainability in turn. As a result, great care should be devoted to the problem of cracking, especially in lightly reinforced structural members.

In this frame, the present thesis deals with the topic of the brittle/ductile behavior of concrete structural elements containing low amounts of different reinforcing systems (i.e., rebar, fibers, or a combination), under static bending actions. Specifically, in what follows, the state-of-the-art on the subject is presented, and a new and unified design-by-testing approach is proposed. Such unified approach is validated with both numerical and experimental results, in presence of rebar and/or fibers as reinforcing system. Moreover, the proposed approach is also applied in a combined ecological and mechanical comparative analysis (i.e., a simplified sustainability assessment) between two fiber-reinforced cement-based composites to be used in a real application.

1.2 State-of-the-art

Due to the small capability of a cement-based composite to delay the propagation of a crack, only bridged by the inclusions (i.e., stone aggregates), plain concrete behaves as a quasi-brittle material (Bažant and Planas 1998, de Borst 2002, Shah et al. 1995). In other words, when a plain concrete statically determined beam is subjected to increasing static bending actions [Figure 1.1(a)], the sudden failure can be observed in the corresponding load vs. deflection ($P - \delta$) curve [i.e., in the dashed line depicted in Figure 1.1(b)].

Therefore, even if some concrete members can be able to bear the applied loads without any reinforcement (Fantilli et al. 2015), code rules always require the presence of a minimum amount of steel rebar (ACI 2014, CEN 2004a, *fib* 2012a), or fibers randomly dispersed in the cementitious matrix (*fib* 2012a), to bridge the cracks. The aim is to avoid the brittle failure under static bending actions, and this concept is particularly relevant when massive concrete structures are realized (Chiaia et al. 2007, Liao et al. 2016, Rizk and Marzouk 2011).

If a reinforcing system is provided (i.e., rebar, fibers, or a combination), the $P - \delta$ curve of a statically determined concrete beam [i.e., a continuous line in Figure 1.1(b)] shows two relative maximum points (Fantilli et al. 2016a,b,c). The first point defines the effective cracking load P_{cr^*} (Maldague 1965), which corresponds to a bending moment in midsection indicated as M_{cr^*} . In this point, a

maximum of the load P (or a maximum of the bending moment M) is reached during the growth of the first crack. Therefore, as it can be observed in Figure 1.1(b), P_{cr^*} (or M_{cr^*}) is higher than the first cracking load P_{cr} (or the first cracking bending moment M_{cr}) that produces the initiation of the crack at the bottom of the beam (Hillerborg et al. 1976). The effective cracking load is also the single maximum which can be observed in the $P-\delta$ curve of a plain concrete beam [Figure 1.1(b)]. On the other hand, the second maximum point is the ultimate load P_u (or the ultimate bending moment M_u) that corresponds to the failure of the reinforcing system (Fantilli et al. 2016a,b,c).

1.2.1 Lightly reinforced concrete beams

According to Levi (1985), a minimum amount of steel rebar needs to be provided in the tensile zones of concrete beams in bending for two reasons. Firstly, a suitable amount of reinforcement prevents the growth of wide cracks in service, and the penetration of aggressive substances that compromise the durability of reinforced concrete elements. On the other hand, the minimum area of steel rebar $A_{s,min}$ guarantees that cracking of concrete in tension occurs before the yielding of reinforcement. In this way, the flexural response at ultimate limit state of Lightly Reinforced Concrete (LRC) beams is ductile. In other words, M_u (herein assumed to be coincident with the bending moment at the yielding of steel rebar) must be larger than M_{cr^*} . Similarly, to assure the ductile failure, which is evidenced by the presence of more than one flexural crack, the load applied to a beam in bending has to satisfy the following condition [Figure 1.1(b)]:

$$P_u \geq P_{cr^*} \quad (1.1)$$

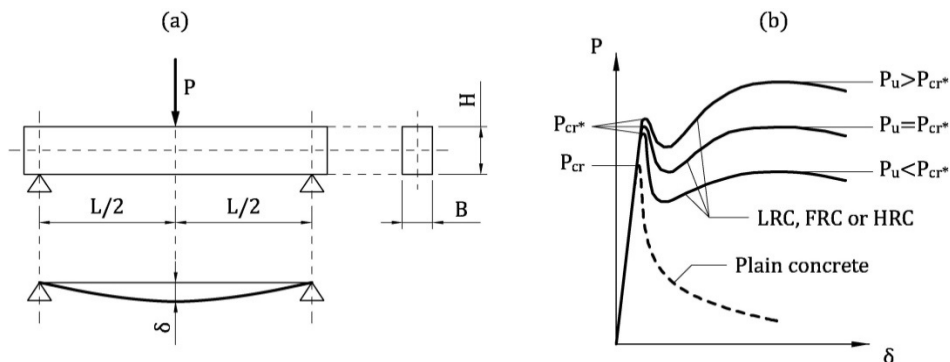


Figure 1.1: Flexural behavior of concrete beams (Ruiz et al. 1999): (a) three point bending test; (b) load vs. midspan deflection curves.

If Eq.(1.1) is satisfied, the bearing capacity of the concrete cross-section is maintained even in the post-cracking stage, because of steel rebar. Conversely, when $M_u < M_{cr^*}$ (or $P_u < P_{cr^*}$), the brittle failure of the beam occurs [Figure 1.1(b)], and a single flexural crack appears. Therefore, at the transition from the brittle to ductile behavior, i.e., when $M_u = M_{cr^*}$ (or $P_u = P_{cr^*}$), the minimum reinforcement for static reasons is defined (Bosco et al. 1990, Fantilli et al. 1999, Ruiz et al. 1999), independently of the midspan deflection δ (Figure 1.1). Indeed, the ductility of LRC beams is defined by the strength, since the yielding of the reinforcement takes place before the sudden failure of concrete in compression, and the collapse of the structural element certainly occurs for sufficiently large deflections. On the other hand, the deformability (i.e., the so-called plastic rotation) measures the ductility of ordinary and over-reinforced concrete members (CEB 1998). In fact, in such cases, the crushing of concrete in compression could take place when the rebar are still in the linear elastic stage, hence the structural element could show small deflections at failure. Anyway, to avoid this brittle failure, not analyzed herein, a maximum area of steel rebar is suggested by Eurocode 2 (CEN 2004a).

For the theoretical evaluation of $A_{s,min}$, some nonlinear models must be applied, taking into account the bond-slip mechanism at the interface between rebar and concrete and the fracture mechanics of cracked concrete in tension (Bažant and Cedolin 1991). Nevertheless, a global and straightforward approach to compute $A_{s,min}$ was not provided by the numerical and experimental analyses performed in the past decades (Bosco et al. 1990, Carpinteri et al. 1999, Fantilli et al. 1999, Lange-Kornbak and Karihaloo 1999, Ruiz et al. 1999), and the topic is still debated (Carpinteri et al. 2014, Fayyad and Lees 2015, Ferro et al. 2007, Rao et al. 2008, Said and Elrakib 2013). As an example, Carpinteri et al. (2014) individuated two non-dimensional parameters as responsible of the brittle/ductile transition in LRC beams. In such parameters, some important mechanical and geometrical properties are taken into account (i.e., concrete tensile strength and toughness, yielding strength of steel rebar, structural size), but other effects, such those of the interaction between rebar and concrete, bar diameter, and concrete cover were neglected.

The same mechanisms, to be considered in the assessment of $A_{s,min}$, are also involved in the evaluation of crack width and crack spacing (*fib* 2000). However, due to the complexity of these topics, a univocally accepted approach, able to predict the crack pattern of reinforced concrete beams, does not exist even if

several studies have been carried out so far (Beeby 2004, 2005, Borosnyói and Balázs 2005, Yasir Alam et al. 2010).

On the other hand, building code rules suggest the use of simplified formulae for determining $A_{s,min}$, in order to satisfy both the serviceability and the ultimate limit state requirements. To be more precise, the following symbolic formula, derived from reinforced concrete ties, is adapted by ACI 318-14 (ACI 2014), Eurocode 2 (CEN 2004a), and Model Code 2010 (*fib* 2012a) to beams in bending:

$$A_{s,min} = \omega \cdot \frac{f_{ct}}{f_y} \cdot B \cdot d \quad (1.2)$$

where ω = coefficient taking into account the model uncertainties, state of stress, and depth of the tensile zone; f_{ct} = tensile strength of concrete; f_y = yielding strength of steel rebar; B and d = width and effective depth, respectively, of a beam cross-section. Similar formulae have also been proposed by other building codes and Researchers (Seguirant et al. 2010).

Some geometrical aspects that affect $A_{s,min}$, such as the size effect produced by the beam depth (Bosco et al. 1990), bar diameter (Fantilli et al. 2005), and non-linear contribution of concrete in tension (Carpinteri et al. 2014), are not taken into account by Eq.(1.2). As a result, this evaluation of the minimum area of rebar to be used in LRC beams under bending actions (ACI 2014, CEN 2004a, *fib* 2012a) is inevitably approximated.

1.2.2 Fiber-reinforced concrete beams

The use of structural fibers made of different materials (e.g., steel, plastic, glass, etc.) as a diffuse reinforcement in the concrete matrix is continuously increasing (di Prisco et al. 2009). Its origin goes back to ancient times (Brandt 2008), and nowadays a wide number of structural applications of Fiber-Reinforced Concrete (FRC) can be found in the literature (Burgers et al. 2007, de la Fuente et al. 2013, di Prisco et al. 2008, Salehian and Barros 2015, Winkler et al. 2014).

Depending on the fiber volume fraction V_f used to reinforce the cementitious matrix, FRC members in bending behave differently (Fantilli et al. 2015, Naaman 2003, Salehian and Barros 2017). To be more precise, when low values of V_f are involved, the beam depicted in Figure 1.1(a) exhibits $P_u < P_{cr*}$ in the $P - \delta$ diagram of Figure 1.1(b), with a brittle response, herein called deflection-softening

(Naaman and Reinhardt 2006, Wille et al. 2014). Conversely, the so-called deflection-hardening [i.e., $P_u > P_{cr^*}$ in Figure 1.1(b)] is shown by the FRC beams containing high amounts of fibers (Naaman and Reinhardt 2006, Wille et al. 2014). Accordingly, at the brittle/ductile transition, [i.e., when $P_u = P_{cr^*}$ in Figure 1.1(b)], the minimum level of ductility is attained and a critical amount of fibers can be defined (Naaman 2003). As this quantity of fibers has the same mechanical role of the minimum area of rebar in LRC beams, it can be defined as the minimum fiber volume fraction $V_{f,min}$ (Fantilli et al. 2016b).

Until now, a univocal approach able to predict the minimum fiber volume fraction in FRC beams does not exist. Some years ago, Naaman (2003) proposed a formula to compute $V_{f,min}$ based on the condition $P_u = P_{cr^*}$, where the values of such loads are functions of the flexural and residual tensile strengths of FRC, respectively. However, the relationship between the strengths and the fiber volume fraction cannot be easily defined, hence the analytical prediction of $V_{f,min}$ is not always effective.

On the other hand, referring to a FRC element, Model Code 2010 (*fib* 2012a) firstly recommends the classification of the material, consisting on the evaluation of residual tensile strengths with three point bending tests on notched beams, according to the standard EN 14651 (CEN 2007). Then, the structural ductility is verified by means of the experimental or numerical load vs. deflection curve (Figure 1.2) referred to the full-scale FRC member under investigation (*fib* 2012a). Specifically, in the absence of conventional reinforcement, the ductility requirement in bending (and the corresponding $V_f \geq V_{f,min}$) is expressed in terms of deformability:

$$\delta_u \geq 20 \cdot \delta_{sls} \quad (1.3).a$$

$$\delta_{peak} \geq 5 \cdot \delta_{sls} \quad (1.3).b$$

where δ_u = ultimate deflection related to the ultimate load P_u ; δ_{peak} = deflection at the maximum load P_{max} ; and δ_{sls} = deflection at the service load P_{sls} , computed with a linear elastic analysis (Figure 1.2).

Moreover, two further conditions are required (*fib* 2012a):

$$P_u \geq P_{sls} \quad (1.4).a$$

$$P_u \geq P_{cr} \quad (1.4).b$$

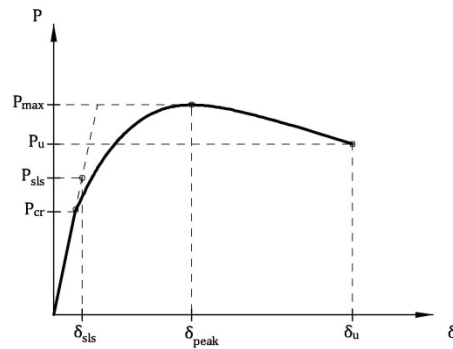


Figure 1.2: Ideal load vs. deflection curve suggested by Model Code 2010 (*fib* 2012a) to measure the ductility of FRC members in the absence of conventional reinforcement.

Although this approach for evaluating the brittle/ductile behavior of FRC beams seems to be very simple, it presents some drawbacks. In particular, as a first approximation, Eq.(1.4).b could be considered equivalent to Eq.(1.1) (Liao et al. 2015), but the first cracking load P_{cr} is taken into account by Model Code 2010 (*fib* 2012a) instead of the effective cracking load P_{cr*} [Figure 1.1(b)]. It is worth noting that this assumption is not conservative, as the presence of reinforcement in the concrete matrix determines a growth of the load during the formation of the first crack, beyond the value of P_{cr} (Hillerborg et al. 1976, Maldague 1965). In addition, Model Code 2010 (*fib* 2012a) does not provide a clear definition for δ_u (or P_u) (Faconi et al. 2016, Faconi and Minelli 2017), hence different interpretations have been adopted by several Authors (Caratelli et al. 2012, di Prisco and Colombo 2012, Faconi et al. 2016, Fantilli et al. 2014).

Despite the similar behavior of LRC and FRC beams, a different approach is proposed by Model Code 2010 (*fib* 2012a) for these two types of concrete members. Specifically, in LRC beams the ductility requirement takes into account only the strength, whereas that for FRC members is mainly based on the deformability, regardless of the effective capability of the structural element to maintain the load after the effective cracking.

More recently, Faconi and Minelli (2017) proposed a new approach for analyzing the brittle/ductile behavior of FRC members, based on an elastic-perfectly plastic idealization of the structural load-deflection curves. This approach certainly represents an improvement of the recommendations given by Model Code 2010, as some additional conditions on the strength are introduced.

1.2.3 Hybrid reinforced concrete beams

When a continuous reinforcement is combined with discrete fibers randomly dispersed in the cementitious matrix, the so-called Hybrid Reinforced Concrete (HRC) is obtained (di Prisco et al. 2016, Massicotte et al. 2014, Pouillon and Vitt 2014). Beyond the several applications in which fibers have not a structural function, as industrial pavements (Barros and Figueiras 1998, Pujadas et al. 2012), HRC is often adopted in massive members, as precast and cast-in-situ tunnel linings, with the aim of reducing the amount of conventional rebar (Caratelli et al. 2012, Chiaia et al. 2009, de la Fuente et al. 2012).

Although many research works were focused on the flexural behavior of HRC structural elements, few attentions have been dedicated to the minimum amount of hybrid reinforcement (i.e., rebar and fibers) to be provided in lightly reinforced members for static reasons. As an example, the experimental campaigns recently performed by Barros et al. (2008), Blanco et al. (2013), de Montaignac et al. (2012), Meda et al. (2012), Ning et al. (2015), and those carried out in the last decades by Kormeling et al. (1980), Lim et al. (1987), Oh (1992), Swamy and Al-Ta'an (1981), Vandewalle (2000) as well, showed cases of prominent hardening behavior. Conversely, Carpinteri et al. (2015), Dancygier and Berkover (2012), di Prisco et al. (2014), Dupont (2003), Falkner and Henke (2005), You et al. (2011) used low amounts of rebar and fibers to reinforce several concrete beams, but the study of a minimum amount of hybrid reinforcement was disregarded. Nevertheless, the transition from the brittle to ductile flexural behavior in HRC members was investigated by Chiaia et al. (2007), Liao et al. (2016) and Mobasher et al. (2015), which showed that a reduction of the minimum amount of rebar is possible in concrete elements containing fibers. For instance, Liao et al. (2016) proposed an analytical approach based on the equilibrium equations at the ultimate limit state of HRC members. As a result, a linear relationship linking the geometrical reinforcement ratio of the rebar, evaluated with Eq.(1.2) (*fib* 2012a), and the residual strength of the FRC matrix, was obtained.

On the other hand, according to building codes (ACI 2014, CEN 2004a, *fib* 2012a), the presence of fibers in the concrete matrix does not reduce, in general, the minimum amount of steel rebar required for static reasons. However, a specific formula to compute the minimum reinforcement for crack control is proposed by Model Code 2010 (*fib* 2012a) in the case of an HRC cross-section:

$$A_{s,\min} = \kappa \cdot (f_{ct} - f_{Ft}) \cdot \frac{A_{ct}}{f_y} \quad (1.5)$$

where κ = coefficient related to the effective state of stress in the HRC cross-section; f_{Ft} = residual tensile strength of FRC, computed from the results of a bending test on a beam specimen performed according to the standard EN 14651 (CEN 2007); and A_{ct} = portion in tension of the concrete cross-section, evaluated at the limit of elasticity.

The minimum reinforcement computed with Eq.(1.5) is the area of rebar, working at a stress equal to f_y , which generates a resultant of tensile stresses equal to that of the cementitious matrix before cracking. When no fibers are added to the cementitious matrix (i.e., $f_{Ft}=0$ in LRC beams), a formula equivalent to Eq.(1.2) can be found. On the other hand, in HRC beams the presence of fibers is related to a residual strength $f_{Ft} \neq 0$, hence Eq.(1.5) allows to reduce $A_{s,\min}$ for increasing values of V_f . However, based on the definition of f_{Ft} given by Model Code 2010 (*fib* 2012a), it is practically impossible to have the equality $f_{Ft}=f_{ct}$. Therefore, even if the sole presence of fibers in concrete members is admitted by Model Code 2010 (*fib* 2012a), according to Eq.(1.5) $A_{s,\min}$ cannot be completely substituted by a suitable amount of fibers. Hence, further researches are necessary to define a univocal method for computing the minimum combined reinforcement in HRC members. Such method must be coherent with those adopted in both LRC and FRC structural elements.

1.3 Proposed approach

Similar mechanical responses, i.e., analogous load *vs.* deflection diagrams, can be observed in LRC, FRC, and HRC beams in bending (Figure 1.1). In particular, the load P_u increases with the amount of rebar and/or fibers, whereas P_{cr^*} , which is mainly a property of the cementitious matrix, remains almost constant. To be more precise, a small variation of the effective cracking load with the area of rebar and/or the fiber volume fraction exists, because P_{cr^*} is reached during the growth of the first crack (Hillerborg et al. 1976, Maldague 1965). Hence, the reinforcing system made of rebar and/or fibers plays its role by bridging the crack surfaces, and the load P_{cr^*} slightly increases with the amount of reinforcement (Gorino et al. 2016).

The ductile behavior of LRC, FRC, and HRC beams, as defined by Eq.(1.1), can also be evinced by the positive value of the following non-dimensional ductility index (DI), whereas DI is lower than zero when brittle failure occurs:

$$DI = \frac{P_u - P_{cr^*}}{P_{cr^*}} = \frac{M_u - M_{cr^*}}{M_{cr^*}} \quad (1.6)$$

As a consequence, the minimum amount of rebar and/or fibers, to be used for reinforcing concrete beams, can be evaluated by imposing $DI=0$. Nevertheless, none additional information is provided by a positive, or negative, value of DI .

It is worth noting that, in agreement with the definition of ductile behavior in lightly reinforced elements reported in Section 1.2.1 [i.e., Eq.(1.1)], DI is a ratio between values of structural strength. Accordingly, it cannot be used in ordinary and over-reinforced concrete members, where the ductility is related to the deformability (CEB 1998).

In analogy with the non-dimensional definition of DI , a normalized reinforcement ratio r can be introduced to define the cross-sectional area of rebar and/or the fiber volume fraction. Since P_u (or M_u) and P_{cr^*} (or M_{cr^*}) depend on the amount of reinforcement, DI is in turn a function of r . In addition, based on the analogous behavior in bending, it is assumed that LRC, FRC, and HRC beams have similar $DI-r$ functions. To be more precise, as illustrated in Figure 1.3, such functions are assumed to be linear, and the slope ζ is equal to the opposite of the intercept:

$$DI = \zeta \cdot (r - 1) \quad (1.7)$$

In other words, $DI=0$ if $r=1$, which should represent the condition of minimum reinforcement. Therefore, the proposed function can be assumed as the linear approximation of a more complex $DI-r$ relationship, in correspondence of the central value $r=1$.

The coefficient ζ , which can differ for LRC, FRC, and HRC beams, is computed by substituting Eq.(1.7) into Eq.(1.6), and deriving both the members with respect to the reinforcement ratio when $r = 1$:

$$\zeta = \frac{\partial}{\partial r} \left(\frac{M_u}{M_{cr^*}} \right)_{r=1} \quad (1.8)$$

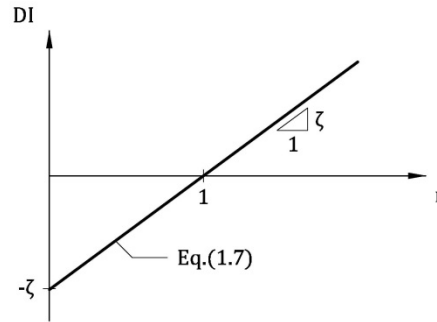


Figure 1.3: Linear approximation of the $DI - r$ relationships.

In the following Chapters, simply formulae for calculating M_u and M_{cr*} are substituted into Eq.(1.8), in order to compute the values of ζ in the three cases of LRC, FRC, and HRC structural elements.

1.4 Research significance

Despite the similar behavior of concrete beams reinforced with rebar and/or fibers, different approaches to quantify $A_{s,min}$ and $V_{f,min}$ in the case of LRC and FRC, respectively, are suggested by code rules (ACI 2014, CEN 2004a, *fib* 2012a). Moreover, in the case of HRC beams, the formula proposed by Model Code 2010 (*fib* 2012a) to evaluate $A_{s,min}$ for crack control [i.e., Eq.(1.5)] does not represent the general case for both LRC and FRC members. On the other hand, the nonlinear fracture mechanics of concrete in tension and the pull-out mechanism of rebar or fibers (Bažant and Cedolin 1991, Naaman 2003) make the theoretical computation of $A_{s,min}$ and $V_{f,min}$ too complicated. Therefore, it is not a valid alternative to the empirical formulae of building codes. Thus, to address that research gap, a unified approach is proposed herein for defining the minimum reinforcement (in terms of rebar, fibers, or a combination) of concrete elements.

As it is illustrated in next Chapters, the proposed approach is based on the results of bending tests on few full-scale members, containing a trial amount of reinforcement (Fantilli et al. 2016a,b,c). Obviously, this strategy makes the proposed approach more appropriate for the field of structural precasting, with respect to a method requiring to perform bending tests on small beam specimens (e.g., Liao et al. 2016). Nevertheless, when FRC beam specimens are tested in three or four point bending, small fracture areas linked by few fibers are involved, especially if low amounts of macro-fibers are used (Minelli and Plizzari 2011).

For this reason, a high experimental scatter typically appears in small beam tests (di Prisco et al. 2009). Thus, for instance, round determined panel tests have been proposed by ASTM C1550-10 (ASTM 2010) as a new characterization method. In this case, i.e., when large concrete elements are tested, a remarkably lower scatter occurs, because of the larger fracture areas involved (Minelli and Plizzari 2015).

In addition, the translation of results between the small scale of FRC beam specimens and the full-scale of real structures is not trivial, and several parameters (e.g., geometrical size, rheological properties, casting conditions, etc.) have to be considered (Grünewald et al. 2014). This concept is well clarified by the words used by Grünewald et al. (2014) to conclude the work of *fib* Task Group 4.3: *“Further development and validation are required to link fiber orientation, the test response of small test specimens and structural response as a basis for reliable design guidelines”*. As a result, until now, the need to perform some full-scale bending tests when fibers are added to the cementitious matrix (i.e., in FRC and HRC members) appears still unavoidable. As a matter of fact, it cannot be excluded that a certain amount of reinforcement, which guarantees a ductile flexural behavior at the specimen scale, corresponds to a brittle failure when used in a real application.

Beyond the brittle/ductile assessment, the proposed ductility index is also adopted in the present thesis as a parameter for measuring the combined ecological and mechanical performances of concrete members in bending. This strategy follows the more general statement of Bocchini et al. (2014), according which *“resilience and sustainability are complementary and should be used in an integrated perspective”*.

Chapter 2

Minimum area of rebar in LRC beams

2.1 Simplified model for LRC beams in bending

Referring to the ultimate limit state of the LRC cross-section illustrated in Figure 2.1, if the contribution of concrete in tension is neglected, the ultimate bending moment M_u can be computed through the classical formula of the moment capacity (Leonhardt and Mönnig 1973, McCormac and Brown 2013, Nilson et al. 2015):

$$M_u = A_s \cdot f_y \cdot Z_{LRC} \quad (2.1)$$

where A_s = cross-sectional area of steel rebar; f_y = yielding strength of steel rebar; and Z_{LRC} = lever arm of the LRC cross-section. According to the results of several experimental tests performed in the last Century (Torroja 1958), it is commonly assumed $Z_{LRC} = 0.9 \cdot d$, with d = effective depth of the concrete cross-section, as depicted in Figure 2.1 (Leonhardt and Mönnig 1973).

On the other hand, considering the effective cracking conditions of the same LRC cross-section, a simple and general formula for M_{cr*} cannot be established. As a matter of fact, the resultant force of the tensile stresses is affected by the nonlinear behavior of concrete in tension, and by the bond-slip mechanism between steel rebar and surrounding concrete (Bažant and Cedolin 1991).

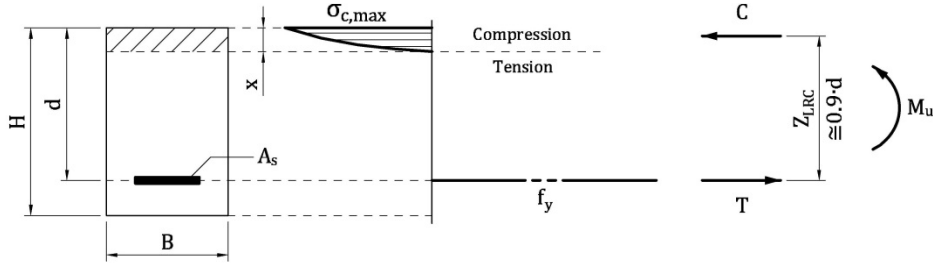


Figure 2.1: Simplified state of stress in a LRC cross-section at ultimate limit state.

However, when the area A_s approaches the minimum reinforcement $A_{s,min}$, the following approximation of the effective cracking moment can be obtained from Eq.(2.1) (Fantilli et al. 2016c):

$$M_{cr^*} = A_{s,min} \cdot f_y \cdot Z_{LRC} \quad (2.2)$$

For the sake of simplicity, in Eq.(2.2) M_{cr^*} is assumed to be independent on the area of reinforcement, regardless of the opening of the crack which occur at the effective cracking (Hillerborg et al. 1976, Maldaque 1965).

Assuming $r = A_s / A_{s,min}$ in the case of LRC beams (Fantilli et al. 2016c), if Eq.(2.1) and Eq.(2.2) are substituted into Eq.(1.8), the coefficient ζ can be evaluated as follows:

$$\zeta = \frac{\partial}{\partial r} \left(\frac{A_s}{A_{s,min}} \right)_{r=1} = 1 \quad (2.3)$$

Accordingly, a single and unitary slope can be obtained for the linear relationship between the ductility index DI and the reinforcement ratio r of LRC beams, which is illustrated in Figure 2.2. The proposed function [i.e., Eq.(1.7)] can be simply described by the following equation:

$$DI = r - 1 \quad (2.4)$$

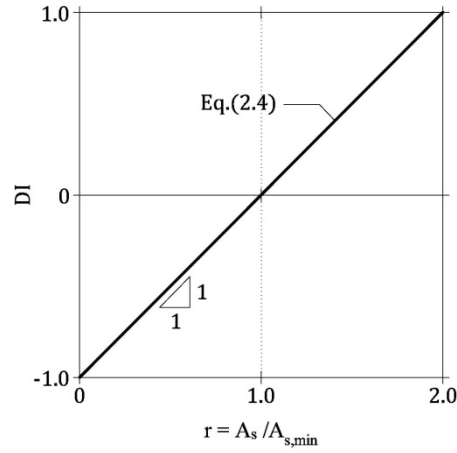


Figure 2.2: $DI - r$ linear function for LRC beams.

2.2 General model for LRC beams in bending

In order to verify the consistency of Eq.(2.4), the general model proposed by Fantilli et al. (1999) for predicting the flexural behavior of LRC members is applied to 36 ideal beams. Then, when the value of $A_{s,min}$ is known for each member, the $[DI - r]$ points are reported in the non-dimensional diagram of Figure 2.2 and compared with Eq.(2.4). Part of the work described in this and next Sections has been previously published in Fantilli et al. (2016a).

2.2.1 Formulation of the problem

A block of LRC beam in three point bending, failing in presence of a single flexural crack, is modelled herein. As shown in Figure 2.3(a), this portion of the beam is delimited by the cracked cross-section [i.e., midsection 0-0 in Figure 2.4(a)] and by the so-called Stage I cross-section [i.e., cross-section 1-1 in Figure 2.4(b)], in which the perfect bond between steel rebar and concrete is re-established. Within the length of such block (i.e., l_{tr} = transfer length), as the horizontal coordinate z increases, stresses and deformations move from rebar to concrete in tension, due to the bond-slip mechanism acting at the interface of the materials. At the level of reinforcement, the slip s vanishes in the Stage I cross-section [Figure 2.3(b)], where concrete strain ε_c equates steel strain ε_s [Figure 2.3(c)].

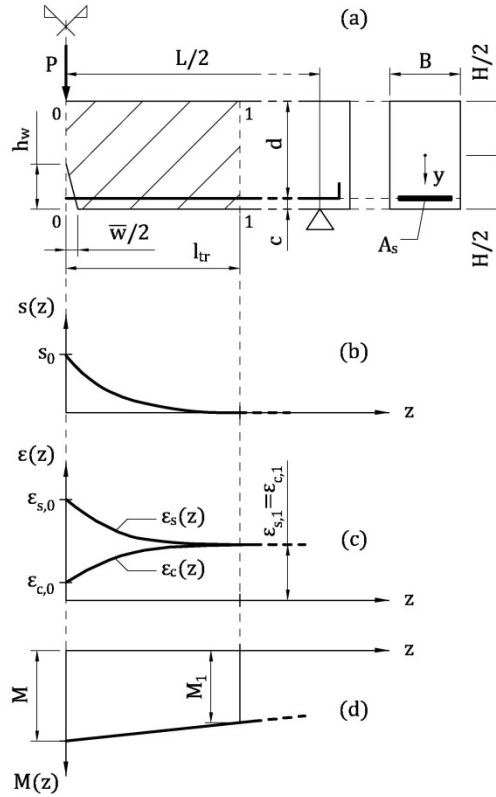


Figure 2.3: General model for LRC beams in bending failing in presence of a single crack: (a) portion of the beam; (b) slips between rebar and concrete in tension; (c) strains of rebar and surrounding concrete; (d) bending moment.

In the cross-section 0-0, a linear strain profile along uncracked concrete and steel rebar is assumed [Figure 2.4(a)]. Conversely, in the cracked zone of depth h_w , crack width w is supposed to linearly decrease from the bottom of the beam (where $w = \bar{w}$) to the tip (where $w = 0$), even if the presence of rebar bridges the crack at level of reinforcement (Giuriani and Plizzari 1989). On the other hand, in the Stage I cross-section [Figure 2.4(b)], the hypothesis of perfect bond makes possible to evaluate the strains of rebar and surrounding concrete $\varepsilon_{s,1} = \varepsilon_{c,1}$ by means of the well-known linear elastic formulation (de Saint-Venant 1856, Timoshenko and Goodier 1970):

$$\varepsilon_{s,1} = \varepsilon_{c,1} = \frac{M_1}{E_o \cdot I_o} \cdot (d - x_1) \quad (2.5)$$

where M_1 = bending moment in the Stage I cross-section; $E_o \cdot I_o$ = flexural rigidity of the composite cross-section (i.e., rebar and concrete) of the LRC beam; and x_1 = distance from the top edge to neutral axis in cross-section 1-1. Within the transfer length, if the value of l_{tr} is small, $M_1 = M$ can be assumed, where M = internal bending moment in the cracked cross-section [Figure 2.3(d)].

In such zone of the LRC beam, the interaction between steel reinforcement and concrete in tension is described by the two following equilibrium and compatibility equations:

$$\frac{d\sigma_s}{dz} = -\frac{p_s}{A_s} \cdot \tau[s(z)] = -\frac{4}{\phi_s} \cdot \tau[s(z)] \quad (2.6)$$

$$\frac{ds}{dz} = -[\varepsilon_s(z) - \varepsilon_c(z)] \quad (2.7)$$

where σ_s = stress of steel rebar; p_s , ϕ_s = perimeter and nominal diameter of rebar, respectively; and τ , s = bond stress and corresponding slip between steel and concrete in tension.

In the absence of external axial loads, the resultant R of axial stresses in cross-section 0-0 becomes equal to zero:

$$R = \int_{A_c} (\sigma_{c,0}) dA + \sigma_{s,0} \cdot A_s = 0 \quad (2.8)$$

where $\sigma_{c,0}$, $\sigma_{s,0}$ = stresses of concrete and steel rebar in the cracked cross-section, respectively; A_c = cross-sectional area of concrete.

Assuming y as the vertical coordinate [Figure 2.3(a)], the internal bending moment M can be computed as follows:

$$M = \int_{A_c} (\sigma_{c,0} \cdot y) dA + \sigma_{s,0} \cdot A_s \cdot \left(\frac{H}{2} - c \right) \quad (2.9)$$

where H = depth of the beam; and c = concrete cover (i.e., distance from the centroid of rebar to the bottom edge of the cross-section).

In accordance with Fantilli and Chiaia (2013a), strain decrements in steel rebar and strain increments in concrete at the level of reinforcement can be assumed as similar:

$$\varepsilon_s(z) = \varepsilon_{s,0} - \chi(z) \cdot (\varepsilon_{s,0} - \varepsilon_{s,1}) \quad (2.10).a$$

$$\varepsilon_c(z) = \varepsilon_{c,0} - \chi(z) \cdot (\varepsilon_{c,0} - \varepsilon_{c,1}) \quad (2.10).b$$

where $\varepsilon_{s,0}$ and $\varepsilon_{c,0}$ = steel and concrete strains at level of reinforcement in the cracked cross-section; and χ = similarity coefficient. It should be remarked that the strain $\varepsilon_{c,0}$ can be obtained from the corresponding stress $\sigma_{c,0}$ [Figure 2.4(a)], by assuming the linear elastic behavior of uncracked concrete (Section 2.2.2) also for the crack surfaces.

To solve the system of Eqs.(2.6)-(2.10), the following boundary conditions are needed:

$$s_0 = \frac{\bar{w}}{2} \cdot \frac{h_w - c}{h_w} \quad (2.11).a$$

$$s(z = l_{tr}) = 0 \quad (2.11).b$$

$$\frac{ds}{dz}(z = l_{tr}) = 0 \quad (2.11).c$$

In Eq.(2.11).a, the slip s_0 in the cracked cross-section is equal to half of crack width at the level of reinforcement. Conversely, in the Stage I cross-section, Eq.(2.11).b and Eq.(2.11).c impose, respectively, the absence of slip and its stationary state [i.e., $\varepsilon_s = \varepsilon_c$ in Eq.(2.7)].

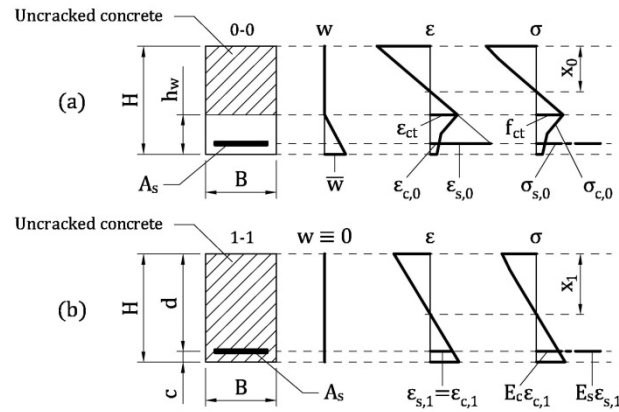


Figure 2.4: State of strain and stress at boundaries of the analyzed portion of LRC beam: (a) cracked cross-section 0-0; (b) Stage I cross-section 1-1.

2.2.2 Material behavior

To model the stress vs. strain ($\sigma_c - \varepsilon_c$) relationship of concrete in compression, the ascending branch of the Sargin's parabola (*fib* 2012a) is used [Figure 2.5(a)]:

$$\sigma_c = -f_c \cdot \left[\frac{k \cdot \eta - \eta^2}{1 + (k - 2) \cdot \eta} \right] \quad \text{for } -\varepsilon_{c1} < \varepsilon_c \leq 0 \quad (2.12)$$

where f_c = cylindrical compressive strength of concrete; $k = E_c / E_{c1}$ = plasticity number; $E_c = 21,500 \cdot (f_c / 10)^{1/3}$ = tangent modulus of elasticity of concrete, at the origin of the $\sigma_c - \varepsilon_c$ diagram, in MPa (f_c in MPa); $E_{c1} = f_c / \varepsilon_{c1}$ = secant modulus from the origin to the peak of compressive stress; ε_{c1} = strain at the peak of stress in compression; and $\eta = |\varepsilon_c / \varepsilon_{c1}|$ = normalized compressive strain.

Moreover, the following linear elastic constitutive law [Figure 2.5(a)] is adopted for the uncracked concrete in tension (i.e., up to the strain at the peak of stress in tension $\varepsilon_{ct} = f_{ct} / E_c$, where f_{ct} = tensile strength of concrete):

$$\sigma_c = E_c \cdot \varepsilon_c \quad \text{for } 0 < \varepsilon_c \leq \varepsilon_{ct} \quad (2.13)$$

According to Model Code 2010 (*fib* 2012a), the mean tensile strength of concrete can be estimated from f_c (expressed in MPa):

$$f_{ct} = 0.3 \cdot (f_c - 8)^{2/3} \quad \text{for } f_c \leq 58 \text{ MPa} \quad (2.14).a$$

$$f_{ct} = 2.12 \cdot \ln(1 + 0.1 \cdot f_c) \quad \text{for } f_c > 58 \text{ MPa} \quad (2.14).b$$

As M_u is assumed to be the moment at the yielding of steel in tension, the stress vs. strain relationship $\sigma_s - \varepsilon_s$ of the rebar is modeled with the elastic-perfectly plastic constitutive law illustrated in Figure 2.5(b) (*fib* 2012a):

$$\sigma_s = E_s \cdot \varepsilon_s \quad \text{for } 0 < \varepsilon_s \leq \varepsilon_y \quad (2.15).a$$

$$\sigma_s = f_y \quad \text{for } \varepsilon_y \leq \varepsilon_s < \varepsilon_u \quad (2.15).b$$

where E_s = modulus of elasticity of steel rebar; f_y and $\varepsilon_y = f_y / E_s$ = yielding strength and strain, respectively; and ε_u = ultimate strain.

Beyond the linear elastic behavior in tension [i.e., Eq.(2.13)], the fictitious crack model is adopted to reproduce the response of cracked concrete (*fib* 2012a). It consists on the following bilinear stress *vs.* crack width $\sigma_c - w$ curve [Figure 2.6(a)]:

$$\sigma_c = f_{ct} \cdot \left(1.0 - 0.8 \cdot \frac{w}{w_1} \right) \quad \text{for } 0 < w \leq w_1 \quad (2.16).a$$

$$\sigma_c = f_{ct} \cdot \left(0.25 - 0.05 \cdot \frac{w}{w_1} \right) \quad \text{for } w_1 < w \leq w_c \quad (2.16).b$$

where $w_1 = G_F/f_{ct}$; $w_c = 5 \cdot G_F/f_{ct}$; and $G_F = 0.073 \cdot f_c^{0.18}$ = fracture energy of concrete in tension (f_c in MPa, G_F in N/mm).

Finally, the following bond *vs.* slip relationship $\tau - s$, proposed by Model Code 2010 (*fib* 2012a) and depicted in Figure 2.6(b), is applied at the interface between concrete in tension and steel rebar:

$$\tau = \tau_{\max} \cdot \left(\frac{s}{s_1} \right)^\alpha \quad \text{for } 0 \leq s < s_1 \quad (2.17).a$$

$$\tau = \tau_{\max} \quad \text{for } s_1 \leq s < s_2 \quad (2.17).b$$

$$\tau = \tau_{\max} - (\tau_{\max} - \tau_f) \cdot \frac{s - s_2}{s_3 - s_2} \quad \text{for } s_2 \leq s < s_3 \quad (2.17).c$$

$$\tau = \tau_f \quad \text{for } s_3 \leq s \quad (2.17).d$$

where $\tau_{\max} = 2.5 \cdot f_c^{0.5}$ = bond strength (f_c in MPa); $\tau_f = 0.4 \cdot \tau_{\max}$ = residual bond stress; $\alpha = 0.4$; $s_1 = 1.0$ mm; $s_2 = 2.0$ mm; and $s_3 = c_{\text{clear}}$ = clear distance between the ribs of the rebar (in mm).

To take into account the possibility of the splitting failure at the interface between rebar and concrete (Gambarova and Rosati 1996, Giuriani and Plizzari 1998), the reduced bond strength $\tau_{u,\text{split}}^2$ (*fib* 2012a), and the associated bond-slip relationship [represented with the dashed line in Figure 2.6(b)], is considered when necessary.

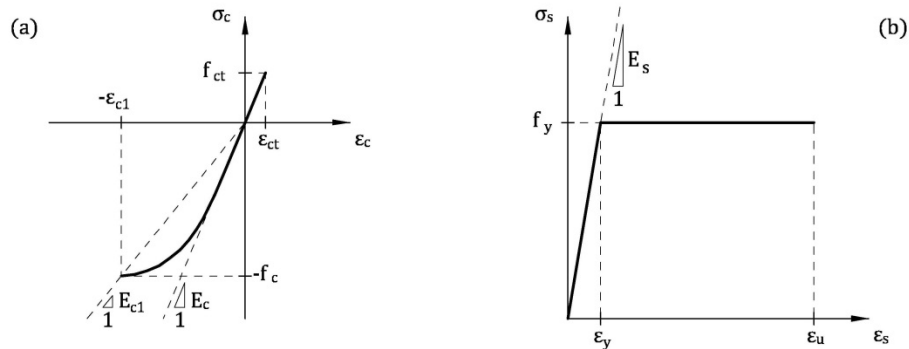


Figure 2.5: Stress vs. strain constitutive relationships of materials (*fib* 2012a): (a) ascending branch of the Sargin's parabola for concrete in compression, and linear elastic law for uncracked concrete in tension; (b) elastic-perfectly plastic law for steel rebar.

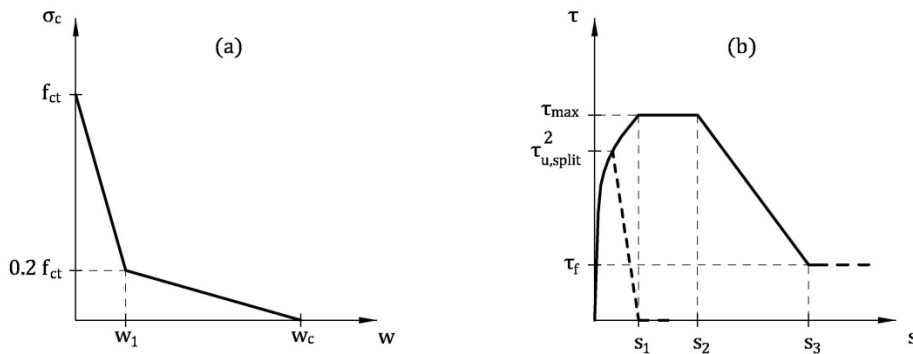


Figure 2.6: Stresses on the crack surface and at the interface between rebar and concrete in tension according to Model Code 2010 (*fib* 2012a): (a) stress vs. crack width relationship; (b) bond-slip model.

2.2.3 Numerical solution of the problem

All the equations previously introduced define the so-called tension-stiffening problem, which has to be solved within the one-dimensional domain of length l_{tr} (Fantilli et al. 1999). This is possible by applying the iterative procedure illustrated in Figure 2.7 and described by the following points, in which the subscript i refers to the abscissa $0 \leq z_i \leq l_{tr}$:

1. Assign a value to \bar{w} in the cracked cross-section [Figure 2.3(a) and Figure 2.4(a)].

2. Assume a trial value for the crack depth h_w [where $c < h_w < H$ in Figure 2.3(a) and Figure 2.4(a)].

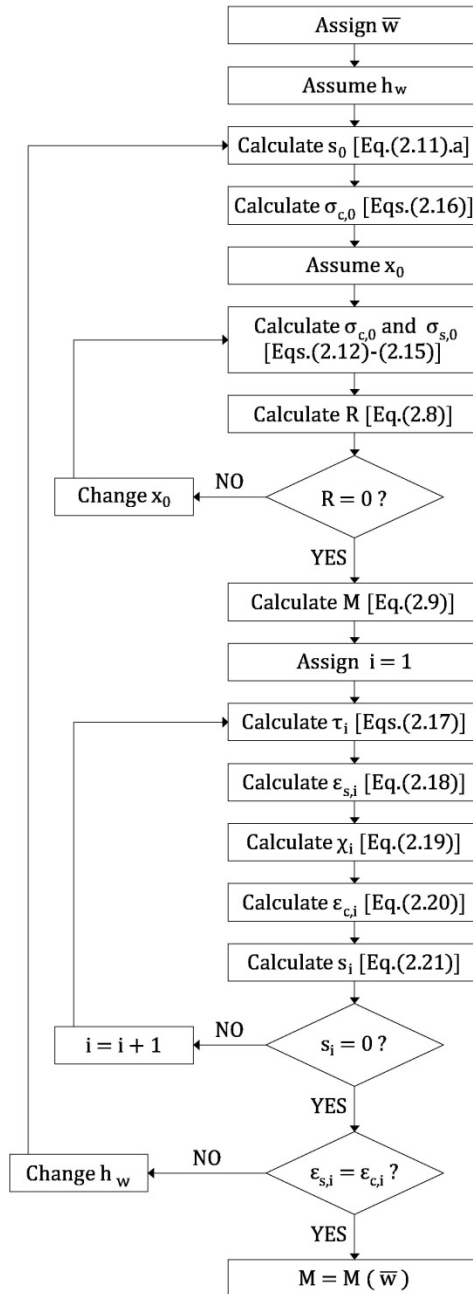


Figure 2.7: Flow-chart of the numerical procedure.

3. Calculate the slip s_0 in the cracked cross-section 0-0 (where $z_i = 0$) [Eq.(2.11).a].
4. By assuming a linear crack profile [Figure 2.4(a)], calculate the cohesive stresses in cracked concrete of cross-section 0-0 by means of Eqs.(2.16).
5. Assume a trial value for x_0 [i.e., the distance from the top edge to the neutral axis in the cracked cross-section of Figure 2.4(a)].
6. By assuming the linearity of the strain profile, define the state of stress referred to uncracked concrete and steel rebar in the cross-section 0-0 [Figure 2.4(a)] through Eqs.(2.12)-(2.15).
7. Calculate the resultant R [Eq.(2.8)].
8. If $R \neq 0$, then change x_0 and go back to step 6.
9. Compute the internal bending moment M in the cracked cross-section [Eq.(2.9)].
10. By considering Δl as a small part of the unknown $l_{tr} < L$ (where $L = \text{span}$ of the beam), define $z_i = i \cdot \Delta l$ (where $i = 1, 2, 3, \dots$).
11. For each i (or z_i) calculate:
 - The bond stress τ_i , related to the slip s_{i-1} [Eqs.(2.17)].
 - The strain $\varepsilon_{s,i}$ in the reinforcement, with Eq.(2.6) written in the finite difference form [and Eq.(2.15).a]:

$$\varepsilon_{s,i} = \varepsilon_{s,i-1} - \frac{4}{\phi_s \cdot E_s} \cdot \tau_i \cdot \Delta l \quad (2.18)$$

- The similarity coefficient χ_i by using Eq.(2.10).a:

$$\chi_i = \frac{\varepsilon_{s,0} - \varepsilon_{s,i}}{\varepsilon_{s,0} - \varepsilon_{s,1}} \quad (2.19)$$

- The strain of concrete at the level of rebar $\varepsilon_{c,i}$, [Eq.(2.10).b]:

$$\varepsilon_{c,i} = \varepsilon_{c,0} - \chi_i \cdot (\varepsilon_{c,0} - \varepsilon_{c,1}) \quad (2.20)$$

- The slip s_i by means of the finite difference form of Eq.(2.7):

$$s_i = s_{i-1} - (\varepsilon_{s,i} - \varepsilon_{c,i}) \cdot \Delta l \quad (2.21)$$

12. When $s_i = 0$, if $\varepsilon_{s,i} \neq \varepsilon_{c,i}$, change h_w and go back to step 3.

For a given \bar{w} , such procedure calculates the corresponding internal moment M . Thus, by varying the assigned crack width, the complete $M - \bar{w}$ curve can be obtained. The starting point of this curve is fixed at M_{cr} (elastically evaluated), which corresponds to $\bar{w} = 0$.

2.3 Analysis of the numerical results

The proposed procedure is used to plot the $M - \bar{w}$ curves of 36 ideal LRC beams in three point bending. They are divided into 12 groups of three beams, having the same geometrical and material properties, but with different amounts of reinforcement in tension. As illustrated in Figure 2.8, the width B and the span L of the beams are one half and six times the depth H , respectively (where $H = 200$ and 400 mm). Compressive strength of concrete varies (i.e., $f_c = 30, 45$ and 60 MPa), whereas the steel of rebar, having diameter ϕ_s , is the same (i.e., $f_y = 450$ MPa and $E_s = 210$ GPa).

Table 2.1 summarizes the geometrical and mechanical characteristics of all the beams. They are labelled with the acronym $SX_CYY_Z_W$, in which X depends on the beam depth ($X = 1$ for 200 mm, and $X = 2$ for 400 mm), YY is the concrete strength ($30, 45$ or 60 MPa), Z is the rebar diameter, and W is a number ($1, 2$, or 3) associated to the value of A_s .

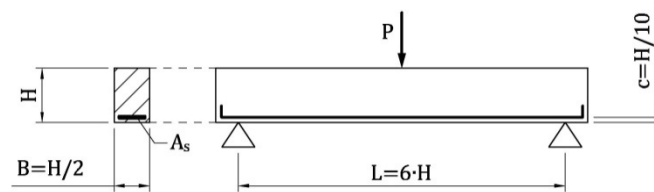


Figure 2.8: Ideal LRC beam in three point bending.

As an example, the $M - \bar{w}$ curves of Group L_9 are reported in Figure 2.9(a). Two stationary points, concerning the effective cracking moment (M_{cr^*}) and the ultimate bending moment (M_u), are clearly evident in all the curves. The beam S1_C60_φ5_1 is under-reinforced (i.e., $M_u < M_{cr^*}$), whereas S1_C60_φ5_2 shows the brittle/ductile transition (i.e., $M_u \cong M_{cr^*}$), and S1_C60_φ5_3 is reinforced with $A_s > A_{s,min}$ (i.e., $M_u > M_{cr^*}$). The values of M_{cr^*} and M_u , taken on the $M - \bar{w}$ curves of the 36 ideal LRC beams, are collected in Table 2.2.

Table 2.2 also reports the values of DI for all the ideal beams [Eq.(1.6)]. Within each group of beams, a linear relationship between DI and A_s is attained [e.g., Figure 2.9(b)]. In other words, referring to Eq.(1.6), if M_{cr^*} is assumed to be independent on the area of rebar, the linear increment of M_u with A_s [Eq.(2.1)] can be recognized in Figure 2.9(b). Thus, $A_{s,min}$ can be detected for each group with the intersection between the line $DI - A_s$ and the horizontal axis $DI = 0$. All the values of $A_{s,min}$ and $r = A_s / A_{s,min}$ are reported in Table 2.2.

Even if beams with different properties are analyzed, the proposed procedure [i.e., Figure 2.9(b)] is capable of properly computing $A_{s,min}$, regardless of size effect and material properties. Indeed, all the $[DI - r]$ couples previously computed are close to the linear function of Eq.(2.4), as shown in Figure 2.10. Hence, due to the non-dimensional definition of Eq.(1.6), the ductility index, previously introduced for a single group of beams, can be generally applied to all the LRC members.

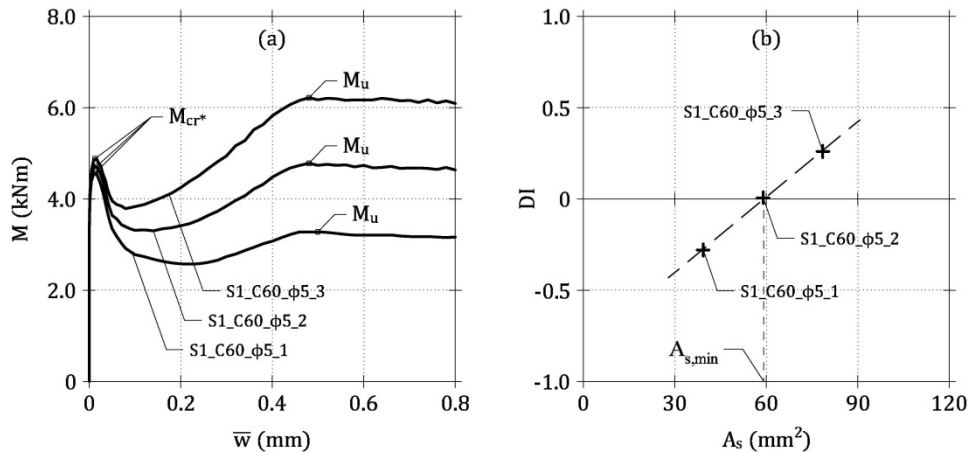


Figure 2.9: Application of the general model to the ideal beams of Group L_9: (a) $M - \bar{w}$ curves; (b) $DI - A_s$ relationship and evaluation of $A_{s,min}$.

Table 2.1: Geometrical and mechanical properties of 36 ideal LRC beams.

Group	Beam	H (mm)	f_c (MPa)	ϕ_s (mm)	A_s (mm ²)
L_1	S1_C30_φ4_1	200	30	4	25
	S1_C30_φ4_2				38
	S1_C30_φ4_3				50
L_2	S1_C30_φ5_1	200	30	5	20
	S1_C30_φ5_2				39
	S1_C30_φ5_3				59
L_3	S2_C30_φ8_1	400	30	8	101
	S2_C30_φ8_2				151
	S2_C30_φ8_3				201
L_4	S2_C30_φ10_1	400	30	10	79
	S2_C30_φ10_2				157
	S2_C30_φ10_3				236
L_5	S1_C45_φ5_1	200	45	5	39
	S1_C45_φ5_2				59
	S1_C45_φ5_3				79
L_6	S1_C45_φ6_1	200	45	6	28
	S1_C45_φ6_2				57
	S1_C45_φ6_3				85
L_7	S2_C45_φ8_1	400	45	8	101
	S2_C45_φ8_2				201
	S2_C45_φ8_3				302
L_8	S2_C45_φ10_1	400	45	10	157
	S2_C45_φ10_2				236
	S2_C45_φ10_3				314
L_9	S1_C60_φ5_1	200	60	5	39
	S1_C60_φ5_2				59
	S1_C60_φ5_3				79
L_10	S1_C60_φ6_1	200	60	6	28
	S1_C60_φ6_2				57
	S1_C60_φ6_3				85
L_11	S2_C60_φ8_1	400	60	8	201
	S2_C60_φ8_2				251
	S2_C60_φ8_3				302
L_12	S2_C60_φ10_1	400	60	10	157
	S2_C60_φ10_2				236
	S2_C60_φ10_3				314

Table 2.2: Evaluation of minimum reinforcement in 36 ideal LRC beams.

Group	Beam	M_{cr^*} (kNm)	M_u (kNm)	DI	$A_{s,min}$ (mm ²)	r
L_1	S1_C30_φ4_1	2.88	2.15	-0.25	36	0.69
	S1_C30_φ4_2	2.98	3.13	0.05		1.04
	S1_C30_φ4_3	3.11	4.02	0.29		1.39
L_2	S1_C30_φ5_1	2.80	1.68	-0.40	37	0.53
	S1_C30_φ5_2	2.92	3.16	0.08		1.07
	S1_C30_φ5_3	3.10	4.60	0.49		1.60
L_3	S2_C30_φ8_1	21.54	16.56	-0.23	138	0.73
	S2_C30_φ8_2	22.23	24.23	0.09		1.09
	S2_C30_φ8_3	23.03	31.45	0.37		1.46
L_4	S2_C30_φ10_1	20.98	12.97	-0.38	137	0.57
	S2_C30_φ10_2	21.63	24.93	0.15		1.15
	S2_C30_φ10_3	22.71	36.77	0.62		1.72
L_5	S1_C45_φ5_1	3.80	3.22	-0.15	48	0.81
	S1_C45_φ5_2	3.98	4.69	0.18		1.22
	S1_C45_φ5_3	4.13	6.19	0.50		1.63
L_6	S1_C45_φ6_1	3.69	2.39	-0.35	48	0.58
	S1_C45_φ6_2	3.87	4.49	0.16		1.17
	S1_C45_φ6_3	4.07	6.55	0.61		1.75
L_7	S2_C45_φ8_1	28.29	16.76	-0.41	187	0.54
	S2_C45_φ8_2	29.58	31.92	0.08		1.07
	S2_C45_φ8_3	31.07	47.14	0.52		1.61
L_8	S2_C45_φ10_1	28.61	24.90	-0.13	184	0.84
	S2_C45_φ10_2	29.56	37.09	0.25		1.26
	S2_C45_φ10_3	30.25	48.71	0.61		1.68
L_9	S1_C60_φ5_1	4.59	3.30	-0.28	59	0.66
	S1_C60_φ5_2	4.75	4.78	0.01		0.99
	S1_C60_φ5_3	4.91	6.19	0.26		1.33
L_10	S1_C60_φ6_1	4.42	2.40	-0.46	59	0.48
	S1_C60_φ6_2	4.62	4.53	-0.02		0.96
	S1_C60_φ6_3	4.86	6.66	0.37		1.44
L_11	S2_C60_φ8_1	35.37	32.15	-0.09	224	0.90
	S2_C60_φ8_2	36.15	40.11	0.11		1.12
	S2_C60_φ8_3	37.05	47.45	0.28		1.34
L_12	S2_C60_φ10_1	34.36	25.52	-0.26	221	0.70
	S2_C60_φ10_2	35.34	37.53	0.06		1.05
	S2_C60_φ10_3	36.06	49.17	0.36		1.40

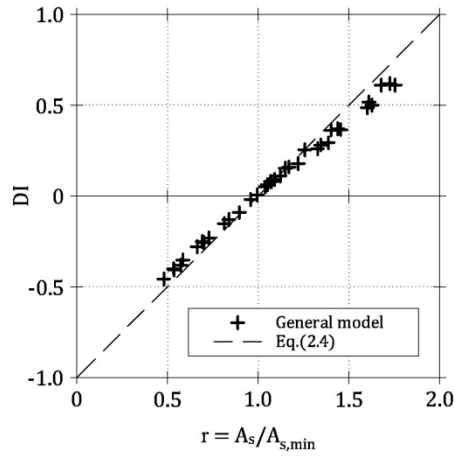


Figure 2.10: Proposed DI - r linear relationship [Eq.(2.4)] in comparison with the results of the general model.

2.4 Comparison with the experimental results

The predictions of DI given by Eq.(2.4) are herein compared with the values computed in 50 LRC beams tested in three point bending by Bosco et al. (1990), Brincker et al. (1999), Carpinteri (1989), Carpinteri et al. (1999, 2015), Hededal and Kroon (1991), Lange-Kornbak and Karihaloo (1999), and Ruiz et al. (1999). Moreover, the four point bending tests performed by Elrakib (2013) are also considered. Specifically, 20 homogeneous groups of at least two beams in bending, unequivocally failing in tension and having the same geometrical and material properties (but different amounts of reinforcement), are taken into consideration (Table 2.3).

As shown in Table 2.3, where the main properties of the 50 beams (labelled with the original names given by the Authors) are reported, a wide range of geometrical sizes and material strengths are analyzed. A certain variation of f_y within groups of homogenous beams is tolerated, especially for the rebar which do not show a well-defined yielding stress.

The experimental values of the effective cracking and ultimate loads, P_{cr*} and P_u , and those of DI [computed by means of Eq.(1.6)] as well, are included in Table 2.4 for all the 50 LRC beams.

Table 2.3: Geometrical and mechanical properties of 50 LRC beams tested by other Authors.

Group	Beam	B (mm)	H (mm)	L (mm)	f_c (MPa)	f_y (MPa)	A_s (mm ²)	References	
L_I	A_1	150	100	600	75.7	637	13	Bosco et al. (1990)	
	A_2						39		
L_II	B_1	150	200	1200	75.7	569	20		
	B_2						59		
L_III	C_1	150	400	2400	75.7	569	637		
	C_2						79		
	C_3						441		
L_IV	NSC_0,14	100	100	1200	64.0	740	13		Brincker et al. (1999)
	NSC_0,25						25		
L_V	HSC_0,14	100	100	1200	98.5	740	13		
	HSC_0,25						25		
L_VI	A_1	150	100	600	24.4	633	20		Carpinteri (1989)
	A_2						39		
L_VII	B_1	150	200	1200	24.4	489	28		
	B_2						57		
	B_3						85		
L_VIII	C_1	150	400	2400	24.4	480	50		
	C_2						101		
L_IX	D_1	200	800	4800	24.4	456	79		
	D_2						157		
	D_3						236		
L_X	A012-06	100	100	600	40.0	604	20	Carpinteri et al. (1999)	
	A025-06						39		
L_XI	A012-12	100	100	1200	40.0	604	20		
	A025-12						39		
L_XII	1 ϕ 8-2	100	200	1400	35.9	484		Carpinteri et al. (2015)	
	1 ϕ 8-3						50		
	1 ϕ 8-4								
	2 ϕ 8-1								
	2 ϕ 8-2						101		
	2 ϕ 8-3								
L_XIII	B501	250	400	3300	43.2	480	157		
	B502						515		
L_XIV	B751	250	400	3300	60.6	495	192	Elrakib (2013)	
	B752						501		
L_XV	B1001	250	400	3300	80.1	480	236		
	B1002						314		

(Table follows in next page)

Group	Beam	B (mm)	H (mm)	L (mm)	f_c (MPa)	f_y (MPa)	A_s (mm ²)	References
L_XVI	A-4-9.8	100	95	800	78.3	588	10	Hededal and Kroon (1991)
	A-4-17.1						17	
L_XVII	A_012_06#1	100	100	600	43	485	13	Lange- Kornbak and Karihaloo (1999)
	A_012_06#3						25	
	A_025_06#1							
	A_025_06#3							
L_XVIII	D1-R2X	50	75	300	39.5	538	5	Ruiz et al. (1999)
	D1-R3X						10	
L_XIX	D2-R1X	50	150	600	39.5	538	5	Ruiz et al. (1999)
	D2-R2X						10	
L_XX	D3-R1X	50	300	1200	39.5	538	10	
	D3-R2X						20	

Referred to the beams of Group L_III tested by Bosco et al. (1990), Figure 2.11(a) reports the values of DI as a function of A_s . Similarly, Figure 2.11(b) shows the test results provided by Carpinteri (1989) for the beams of Group L_IX (Table 2.3 and Table 2.4). For both the groups, comprising three beams with the same geometry and material, but different areas of rebar, Figure 2.11 seems to confirm the existence of a linear relationship between DI and A_s , as numerically obtained in Figure 2.9(b).

Table 2.4: Evaluation of minimum reinforcement in 50 LRC beams tested by other Authors.

Group	Beam	P_{cr}^* (kN)	P_u (kN)	DI	$A_{s,min}$ (mm ²)	r	References	
L_I	A_1	11.8	7.0	-0.41	30	0.42	Bosco et al. (1990)	
	A_2	12.5	15.2	0.22		1.31		
L_II	B_1	19.6	10.3	-0.47	52	0.38		
	B_2	20.9	23.1	0.11		1.14		
L_III	C_1	36.7	15.7	-0.57	138	0.18		
	C_2	38.8	32.4	-0.17		0.57		
	C_3	43.2	54.0	0.25		1.46		
L_IV	NSC_0,14	2.9	3.1	0.08	11	1.12		Brincker et al. (1999)
	NSC_0,25	3.2	5.8	0.84		2.24		
L_V	HSC_0,14	3.5	3.2	-0.07	14	0.91		
	HSC_0,25	3.6	5.9	0.63		1.81		

(Table follows in next page)

Group	Beam	P_{cr*} (kN)	P_u (kN)	DI	$A_{s,min}$ (mm ²)	r	References	
L_VI	A_1	11.3	11.5	0.02	19	1.02	Carpinteri (1989)	
	A_2	11.1	19.8	0.78		2.05		
L_VII	B_1	11.3	10.1	-0.11	37	0.76		
	B_2	14.1	17.7	0.26		1.53		
	B_3	12.1	24.9	1.06		2.29		
L_VIII	C_1	19.9	20.1	0.01	49	1.02		
	C_2	21.7	31.3	0.44		2.05		
L_IX	D_1	35.2	27.8	-0.21	141	0.56		
	D_2	43.4	45.3	0.04		1.11		
	D_3	45.6	60.6	0.33		1.67		
L_X	A012-06	7.1	6.3	-0.11	22	0.89		Carpinteri et al. (1999)
	A025-06	7.0	12.3	0.76		1.77		
L_XI	A012-12	3.2	3.1	-0.03	20	0.97		
	A025-12	3.1	5.7	0.84		1.93		
L_XII	1φ8-2	14.7	19.0	0.30	41	1.23		Carpinteri et al. (2015)
	1φ8-3	17.8	19.4	0.09				
	1φ8-4	16.4	19.6	0.19				
	2φ8-1	17.2	37.1	1.16		2.47		
	2φ8-2	14.7	38.2	1.59				
	2φ8-3	18.5	39.0	1.10				
	2φ8-4	18.4	36.3	0.97				
L_XIII	B501	37.6	44.0	0.17	135	1.17		
	B502	44.5	75.5	0.70		1.68		
L_XIV	B751	39.3	50.5	0.28	140	1.36	Elrakib (2013)	
	B752	46.1	79.4	0.72		1.92		
L_XV	B1001	43.9	65.2	0.49	131	1.80		
	B1002	47.8	88.4	0.85		2.40		
L_XVI	A-4-9.8	6.8	2.92	-0.57	29	0.34	Hededal and Kroon (1991)	
	A-4-17.1	6.8	4.42	-0.35		0.59		
L_XVII	A_012_06#1	6.9	4.4	-0.36	20	0.64	Lange- Kornbak and Karihaloo (1999)	
	A_012_06#3	7.0	4.8	-0.31				
	A_025_06#1	7.0	8.8	0.26		1.28		
	A_025_06#3	7.3	9.2	0.26				
L_XVIII	D1-R2X	3.6	2.7	-0.25	7	0.72		
	D1-R3X	3.6	5.0	0.39		1.44		
L_XIX	D2-R1X	6.8	2.8	-0.59	12	0.41	Ruiz et al. (1999)	
	D2-R2X	6.5	5.3	-0.19		0.81		
L_XX	D3-R1X	11.3	5.9	-0.48	28	0.35		
	D3-R2X	11.3	8.9	-0.22		0.70		

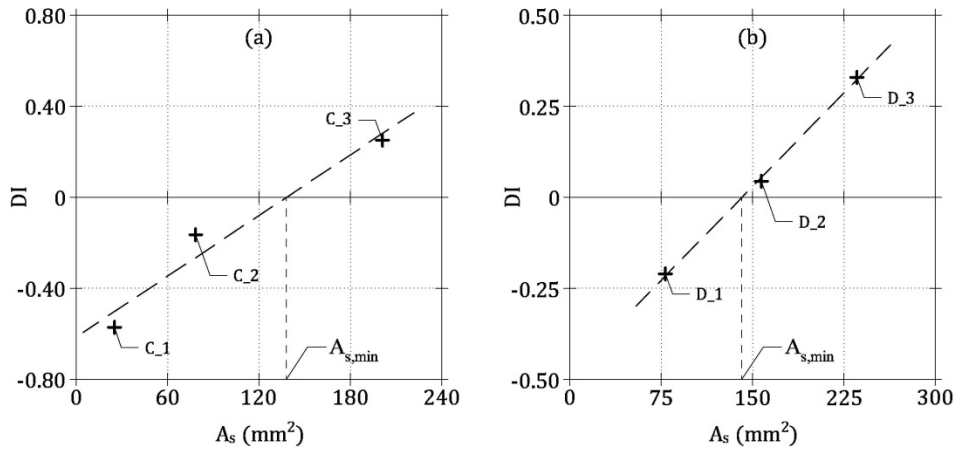


Figure 2.11: $DI-A_s$ relationships and evaluation of $A_{s,min}$ in LRC beams tested in some experimental campaigns: (a) beams of Group L_III tested by Bosco et al. (1990); (b) beams of Group L_IX tested by Carpinteri (1989).

In such situation, $A_{s,min}$ can be evaluated as in Figure 2.9(b), when the values of DI are known from the test results by means of Eq.(1.6). In Table 2.4, the minimum reinforcement area, computed for each homogeneous group of LRC beams, and the corresponding values of $r = A_s / A_{s,min}$, are also collected.

Both the experimental points [$DI-r$], and the proposed linear function [i.e., Eq.(2.4)], are depicted in Figure 2.12. In spite of the dispersion of the results, the tests confirm the linear dependence of DI and r , especially when $DI \cong 0$.

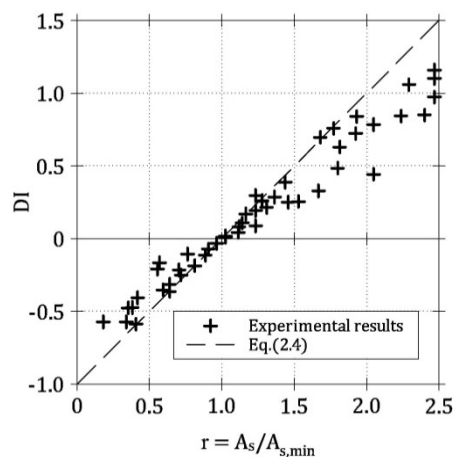


Figure 2.12: Proposed $DI-r$ linear relationship [Eq.(2.4)] in comparison with the results of some experimental campaigns.

However, as for the numerical data reported in Figure 2.10, the unit slope provided by the simplified approach appears too high for fitting the test results. Indeed, the least square approximation of the experimental points reported in Figure 2.12 provides a slope $\zeta = 0.8$. This difference can be ascribed to the approximation in the evaluation of M_{cr*} [Eq.(2.2)].

2.5 Discussion of the results

Both the numerical and experimental results of Figure 2.10 and Figure 2.12, respectively, confirm the existence of a linear dependence of DI on r , even if the slope ζ seems to be smaller than the unit value obtained in Section 2.1. This relationship appears to be generally valid, despite the different geometries and materials of the 36 ideal beams described in Table 2.1, and of the 50 LRC beams tested by other Authors (Table 2.3). In other words, the brittle/ductile behavior of LRC beams can be evaluated by introducing two non-dimensional parameters, i.e., DI and r , without explicitly considering the geometrical size and the mechanical properties of the materials. This means that all the parameters affecting $A_{s,min}$ are included in both numerator and denominator of DI [i.e., Eq.(1.6)] and $r = A_s/A_{s,min}$. Hence, they do not influence the linearity of the proposed DI - r relationship, even if a slope smaller than the unit value obtained in Section 2.1 is shown in both Figure 2.10 and Figure 2.12.

In addition, some simplified hypotheses used in the general model (e.g., the constitutive law of steel rebar, the linear crack profile, the cohesive and the bond-slip models, the constant bending moment inside l_{tr}) seem to have a small relevance in the evaluation of the brittle/ductile behavior of LRC beams. Indeed, they affect in similar manner P_{cr*} and P_u , and, despite the nonlinearities, a linear DI - r function is obtained.

As a consequence, a simple-to-apply procedure, requiring the results of few tests on a single full-scale LRC beam reinforced with a trial area of rebar, can provide the minimum reinforcement for static reasons. In fact, from the average ductility index measured in the tests, the corresponding value of the ratio r can be obtained through the DI - r linear relationship. Then, the calculation of $A_{s,min}$ is possible by inverting the definition of the normalized reinforcement ratio. This procedure can be summarized by the following equation:

$$A_{s,\min} = \frac{\zeta \cdot A_s}{DI + \zeta} \quad (2.22)$$

where A_s , DI = area of reinforcement and ductility index of the tested beam.

Chapter 3

Minimum fiber volume fraction in FRC beams

3.1 Simplified model for FRC beams in bending

In a FRC cross-section at ultimate limit state (Figure 3.1), the volume of fibers V_f added to the concrete matrix works as an amount of traditional rebar (Falkner and Henke 2005). Hence, a simple moment capacity formula to determine the ultimate bending moment M_u can be obtained by modifying the classical formula of Eq.(2.1) as follows:

$$M_u = A_{s,eq} \cdot f_y \cdot Z_{FRC} \quad (3.1)$$

where $A_{s,eq}$ = equivalent area of steel rebar corresponding to V_f ; f_y = yielding strength of the equivalent steel rebar; and Z_{FRC} = lever arm of the FRC cross-section. According to Model Code 2010 (*fib* 2012a), the tensile stresses at ultimate limit state are assumed to be constant and equal to the residual strength f_R in the FRC cross-section of Figure 3.1. Moreover, due to the small value of f_R , the depth of the cross-section which needs to be in compression for assuring the equilibrium vanishes (i.e., $x \rightarrow 0$ in Figure 3.1). Hence, Z_{FRC} can be taken as one half of the beam depth H (*fib* 2012a).

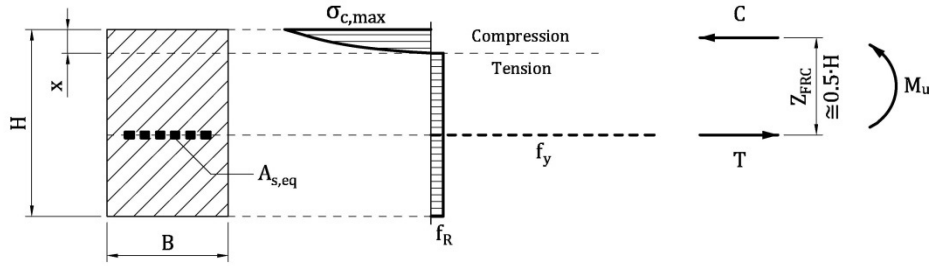


Figure 3.1: Simplified state of stress in a FRC cross-section at ultimate limit state.

Concerning the effective cracking moment M_{cr^*} , a general formula cannot be easily obtained, as for LRC beams. However, when V_f approaches the minimum fiber volume fraction $V_{f,min}$, or equivalently when $A_{s,eq} \rightarrow A_{s,min}$, the effective cracking moment can be estimated as in Section 2.1. According to Fantilli et al. (2016c), M_{cr^*} is assumed to be independent on type and amount of reinforcement, even if a certain influence of V_f exist (Balaguru and Shah 1992, Bentur and Mindess 1990). However, by accepting this approximation, the same formula used in the case of LRC members [i.e., Eq.(2.2)] is still valid for FRC beams:

$$M_{cr^*} = A_{s,min} \cdot f_y \cdot Z_{LRC} \quad (3.2)$$

As in LRC members, the reinforcement ratio $r = V_f / V_{f,min}$ can be introduced. In addition, it can be argued that $A_{s,eq}$ and $A_{s,min}$ are proportional to V_f and $V_{f,min}$, respectively (Fantilli et al. 2016c), thus r is also equal to $A_{s,eq} / A_{s,min}$. As a result, if Eq.(3.1) and Eq.(3.2) are substituted into Eq.(1.8), the coefficient ζ becomes:

$$\zeta = \frac{\partial}{\partial r} \left(\frac{A_{s,eq}}{A_{s,min}} \cdot \frac{Z_{FRC}}{Z_{LRC}} \right)_{r=1} = \frac{Z_{FRC}}{Z_{LRC}} \quad (3.3)$$

Referring to the lever arm of a LRC cross-section (i.e., $Z_{LRC} = 0.9 \cdot d$ as reported in Section 2.1), the effective depth d can be assumed equal to $0.8 \cdot H$ (Fantilli et al. 2016c). By substituting the values of Z_{LRC} and Z_{FRC} in Eq.(3.3), $\zeta = 0.7$ can be obtained, hence the linear relationship between the ductility index DI and the reinforcement ratio r of Eq.(1.7) becomes (Figure 3.2):

$$DI = 0.7 \cdot (r - 1) \quad (3.4)$$

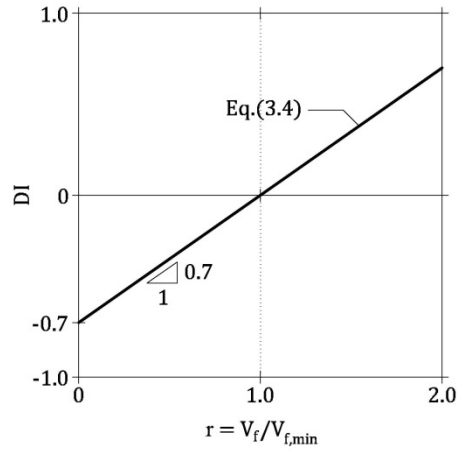


Figure 3.2: $DI - r$ linear function for FRC beams.

3.2 General model for FRC beams in bending

The general model proposed by Fantilli et al. (2016b) is applied herein for predicting the flexural response of 54 ideal FRC beams. The aim is to evaluate the values of $V_{f,min}$, compute the corresponding r , and then compare the $[DI - r]$ points with the proposed linear relationship depicted in the non-dimensional diagram of Figure 3.2 [i.e., Eq.(3.4)]. Part of the work described in this and next Sections has been previously published in Fantilli et al. (2016b).

In the multi-scale general model proposed by Fantilli et al. (2016b), the fiber-reinforcement is modelled with an ideal tie, composed by a straight fiber and the surrounding cementitious matrix, having a crack in the middle. By modelling the pull-out mechanism of this element, the stress *vs.* crack opening relationship of cracked FRC can be evaluated. Then, the latter turns into a stress *vs.* strain law by means of the characteristic length. When the behavior of FRC in tension is known, the flexural response of a beam can be properly defined.

3.2.1 Modelling the fiber pull-out

The ideal tie modelling the fiber-reinforcement consists of a single straight fiber surrounded by the cross-sectional area of cementitious matrix A_m , which is a function of the amount of fibers used in the FRC mixture [Figure 3.3(a)]:

$$A_m = \frac{A_f}{V_f} = \frac{\pi \cdot \phi_f^2}{4 \cdot V_f} \quad (3.5)$$

where A_f , ϕ_f = area and diameter of the fiber cross-section, respectively.

As in the case of an ordinary reinforced concrete tie (Fantilli et al. 1999), a portion of the element, delimited by the cracked cross-section [i.e., cross-section 0-0 in Figure 3.3(a)] and the Stage I cross-section [i.e., cross-section 1-1 in Figure 3.3(a)], is investigated herein. The cracked cross-section is assumed to be in the middle and orthogonal to the fiber. In analogy with the LRC beam, in cross-section 1-1 the perfect bond between steel fiber and concrete is re-established. Moreover, as the horizontal coordinate z increases from zero (in cross-section 0-0) to the transfer length l_{tr} (in cross-section 1-1), stresses and strains move from steel fiber to concrete in tension, due to the bond-slip mechanism acting at the interface of the materials. The slip s between fiber and concrete equates zero in Stage I cross-section [Figure 3.3(b)], where the strain of fiber ε_f and that of concrete matrix ε_m are equal to the value $\varepsilon_{f,1} = \varepsilon_{m,1}$, according to the linear elastic theory [Figure 3.3(c)]:

$$\varepsilon_{f,1} = \varepsilon_{m,1} = \frac{N}{E_o \cdot A_o} \quad (3.6)$$

where N = applied axial load [Figure 3.3(a)]; $E_o \cdot A_o$ = axial rigidity of the composite cross-section (i.e., fiber and concrete matrix) of the ideal tie.

Within the transfer length, the interaction between fiber and matrix is described by equilibrium and compatibility equations, formally identical to Eqs.(2.6)-(2.7):

$$\frac{d\sigma_f}{dz} = -\frac{p_f}{A_f} \cdot \tau[s(z)] = -\frac{4}{\phi_f} \cdot \tau[s(z)] \quad (3.7)$$

$$\frac{ds}{dz} = -[\varepsilon_f(z) - \varepsilon_m(z)] \quad (3.8)$$

where σ_f = stress in the fiber; p_f = perimeter of the fiber cross-section; τ = bond stress corresponding to the slip s between fiber and concrete matrix.

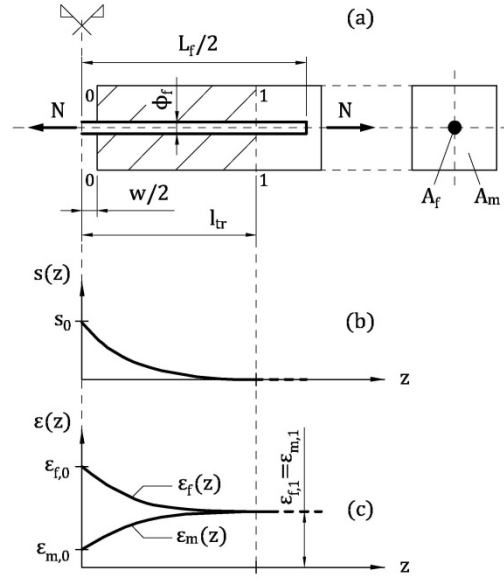


Figure 3.3: Modeling the fiber pull-out: (a) portion of the ideal tie composed by a straight fiber and the surrounding cementitious matrix in presence of a single crack; (b) slip between fiber and matrix; (c) strains in fiber and matrix.

The resultant N of the axial stresses in fiber and cementitious matrix (i.e., σ_f and σ_m , respectively), acting in each cross-section of the ideal tie, can be computed as:

$$N = \sigma_f \cdot A_f + \sigma_m \cdot A_m \quad (3.9)$$

The system of Eqs.(3.7)-(3.9) needs the following boundary conditions:

$$s_0 = \frac{w}{2} \quad (3.10).a$$

$$s(z = l_{tr}) = 0 \quad (3.10).b$$

$$\frac{ds}{dz}(z = l_{tr}) = 0 \quad (3.10).c$$

By means of Eq.(3.10).a, the value of the slip s_0 in the cracked cross-section is equal to the half of crack width w , whereas Eq.(3.10).b states the absence of slip at a distance l_{tr} from the midsection. Only when $l_{tr} < L_f/2$ (where L_f = fiber length), this condition can be considered valid, otherwise the whole fiber slips with respect to the matrix. Eq.(3.10).c is equivalent to consider $\epsilon_f = \epsilon_m$ in Eq.(3.8).

The linear elastic behavior is assumed for both steel fiber and uncracked concrete matrix, according to the following constitutive laws:

$$\sigma_f = E_f \cdot \varepsilon_f \quad (3.11)$$

$$\sigma_m = E_m \cdot \varepsilon_m \quad (3.12)$$

where E_f , E_m = modulus of elasticity of fiber and matrix, respectively.

On the other hand, the cohesive tensile stress on the crack surfaces of the ideal tie can be defined by the fictitious crack model proposed by Model Code 2010 (*fib* 2012a) and already used in Section 2.2 [Figure 3.4(a)]:

$$\sigma_m = f_{ct} \cdot \left(1.0 - 0.8 \cdot \frac{w}{w_1} \right) \quad \text{for } 0 < w \leq w_1 \quad (3.13).a$$

$$\sigma_m = f_{ct} \cdot \left(0.25 - 0.05 \cdot \frac{w}{w_1} \right) \quad \text{for } w_1 < w \leq w_c \quad (3.13).b$$

where $w_1 = G_F / f_{ct}$; $w_c = 5 \cdot G_F / f_{ct}$; $G_F = 0.073 \cdot f_c^{0.18}$ = fracture energy of concrete in tension in N/mm (compressive strength f_c in MPa), f_{ct} = tensile strength of concrete (expressed in MPa), which can be evaluated from f_c through Eqs.(2.14) (*fib* 2012a).

The interaction between fiber and concrete matrix requires the definition of a bond vs. slip (τ - s) relationship. For the sake of simplicity, the model proposed by Fantilli and Vallini (2003), originally developed for smooth steel fibers in a cementitious matrix, is adopted herein [Figure 3.4(b)]:

$$\tau = \tau_{\max} \cdot \left(\frac{s}{s_1} \right)^\alpha \quad \text{for } 0 \leq s < s_1 \quad (3.14).a$$

$$\tau = \tau_f + (\tau_{\max} - \tau_f) \cdot e^{\beta \cdot (s_1 - s)} \quad \text{for } s_1 \leq s \quad (3.14).b$$

where τ_{\max} = bond strength; τ_f = residual bond stress; $s_1 = 0.1$ mm; $\alpha = 0.5$; and $\beta = 2$ / mm.

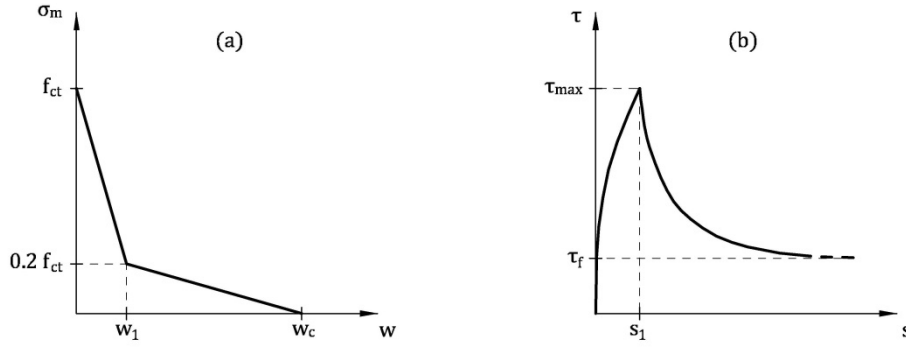


Figure 3.4: Stresses on the crack surface and at the interface between fiber and matrix: (a) fictitious crack model proposed by Model Code 2010 (*fib* 2012a); (b) bond-slip model proposed by Fantilli and Vallini (2003).

The values of τ_{\max} and τ_f can be computed with the following formulae:

$$\tau_{\max} = \frac{1.572}{\sqrt{12.5 + \phi_f}} \cdot \sqrt{f_c} \quad (3.15).a$$

$$\tau_f = 0.1 \cdot \sqrt{f_c} \quad (3.15).b$$

where the compressive strength of concrete must be expressed in MPa and the fiber diameter in mm.

3.2.2 Numerical evaluation of the fiber pull-out

To predict the pull-out behavior of the ideal tie depicted in Figure 3.3(a), the tension-stiffening problem can be solved by means of the iterative procedure illustrated in Figure 3.5. Such a procedure is summarized by the following points (the subscript i refers to the abscissa $0 \leq z_i \leq l_{tr}$):

1. Assign a value to the crack width w in midsection of the ideal tie [Figure 3.3(a)].
2. Compute the slip s_0 in cross-section 0-0 [Figure 3.3(b)] with Eq.(3.10).a.
3. By means of Eqs.(3.13), calculate the tensile stress of the matrix in midsection $\sigma_{m,0}$.

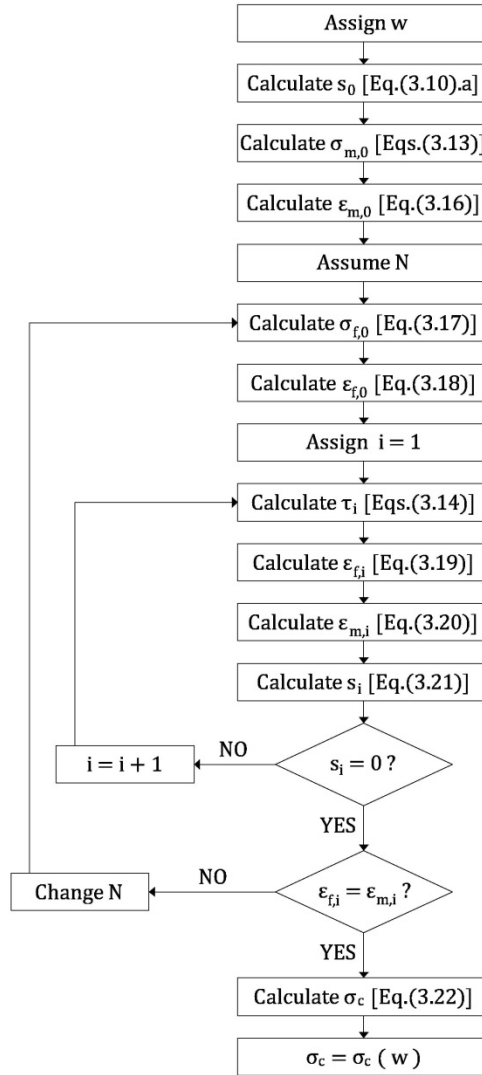


Figure 3.5: Flow-chart of the numerical procedure for evaluating the fiber pull-out.

4. According to Eq.(3.12), determine the strain in midsection $\epsilon_{m,0}$:

$$\epsilon_{m,0} = \frac{\sigma_{m,0}}{E_m} \quad (3.16)$$

5. Assume a trial value for the axial load N [Figure 3.3(a)].
6. According to Eq.(3.9), the stress of the fiber in midsection $\sigma_{f,0}$ can be evaluated with the following equation:

$$\sigma_{f,0} = \frac{N - \sigma_{m,0} \cdot A_m}{A_f} \quad (3.17)$$

In order to exclude the brittle response of the ideal tie, $\sigma_{f,0}$ must be lower than f_u (where f_u = ultimate strength of fiber).

7. Based on the linear elastic behavior of the fiber [Eq.(3.11)], calculate the strain in the midsection $\varepsilon_{f,0}$:

$$\varepsilon_{f,0} = \frac{\sigma_{f,0}}{E_f} \quad (3.18)$$

8. Considering Δl as a small portion of the unknown $l_{tr} < L_f/2$, define $z_i = i \cdot \Delta l$ (where $i = 1, 2, 3, \dots$).
9. For each i (or z_i) calculate:

- The bond stress τ_i , related to the slip s_{i-1} [Eqs.(3.14)].
- The strain of the fiber $\varepsilon_{f,i}$, based on Eq.(3.7) and Eq.(3.11):

$$\varepsilon_{f,i} = \varepsilon_{f,i-1} - \frac{4}{\phi_f \cdot E_f} \cdot \tau_i \cdot \Delta l \quad (3.19)$$

- The strain of the matrix $\varepsilon_{m,i}$, according to Eq.(3.9) and Eq.(3.12):

$$\varepsilon_{m,i} = \frac{N - \varepsilon_{f,i} \cdot E_f \cdot A_f}{E_m \cdot A_m} \quad (3.20)$$

- The slip s_i , by means of the finite difference form of Eq.(3.8):

$$s_i = s_{i-1} - (\varepsilon_{f,i} - \varepsilon_{m,i}) \cdot \Delta l \quad (3.21)$$

10. When $s_i = 0$ [Eq.(3.10).b], if $\varepsilon_{f,i} \neq \varepsilon_{m,i}$, change N and go back to step 6.
11. Calculate the tensile stress σ_c referred to the cross-sectional area of the tie [i.e., $A_m + A_f$ in Figure 3.3(a)]:

$$\sigma_c = \frac{N}{A_m + A_f} \quad (3.22)$$

For a given w , such procedure calculates the corresponding stress of the cracked FRC in tension. The complete $\sigma_c - w$ curve, which follows the linear elastic stage before cracking [Figure 3.6(a)], can be obtained by varying the assigned crack width [Figure 3.6(b)]. It should be remarked that the typical shape of the $\sigma_c - w$ curve provided by the ideal tie, and reported in Figure 3.6(b), is similar to other laws used in the literature to schematize the post-cracking tensile behavior of FRC (e.g., de Montaignac et al. 2012, Facconi and Minelli 2017, Salehian and Barros 2017).

The whole mechanical response of cracked FRC can also be expressed in terms of stress *vs.* strain relationship. Indeed, the crack width w can be smeared into the equivalent strain ε_c as follows (Figure 3.6):

$$\varepsilon_c = \frac{\sigma_{m,0}}{E_m} + \frac{w}{L_f} \quad (3.23)$$

In this way, L_f is assumed to be the characteristic length, or the zone where the inelastic strains localize (Chiaia et al. 2007). In agreement with de Montaignac et al. (2012), the second term of Eq.(3.23) provides the most relevant contribution to ε_c .

3.2.3 Modelling the flexural response of FRC beams

The flexural behavior of FRC beams is defined herein by means of the moment M *vs.* curvature μ relationship referred to the midsection. As depicted in Figure 3.7, to evaluate the $M - \mu$ relationship of a beam cross-section, having a width B and a depth H , the classical hypothesis of linear strain profile is adopted:

$$\varepsilon_c = \lambda + \mu \cdot y \quad (3.24)$$

where ε_c = strain in a generic level of the cross-section; and λ = strain at the origin of coordinate y , located at $H/2$ from the edges of the cross-section (Figure 3.7).

In the absence of an external axial load, the resultant R of the cross-sectional stresses becomes:

$$R = \int_{A_c} (\sigma_c) dA = 0 \quad (3.25)$$

where A_c = cross-sectional area; and σ_c = stress in a generic level.

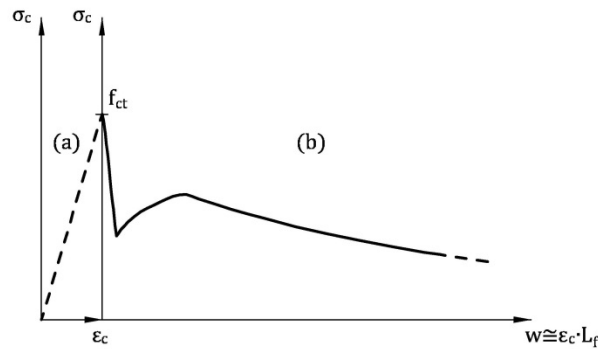


Figure 3.6: Stresses of FRC in tension: (a) linear elastic stage; (b) cracked stage.

Moreover, the internal bending moment M , corresponding to a given state of stress, can be computed as follows:

$$M = \int_{A_c} (\sigma_c \cdot y) dA \tag{3.26}$$

To define the state of stress in the FRC cross-section, in addition to the $\sigma_c - \varepsilon_c$ relationship already obtained in Section 3.2.2 for cracked FRC [Figure 3.6(b)], the constitutive laws of uncracked concrete must be introduced. Specifically, the ascending branch of the Sargin’s parabola (*fib* 2016) is adopted in compression, and the linear elastic law is used in tension (Figure 3.8). In other words, the previous Eq.(2.12) and Eq.(2.13) are also used in the case of FRC beams.

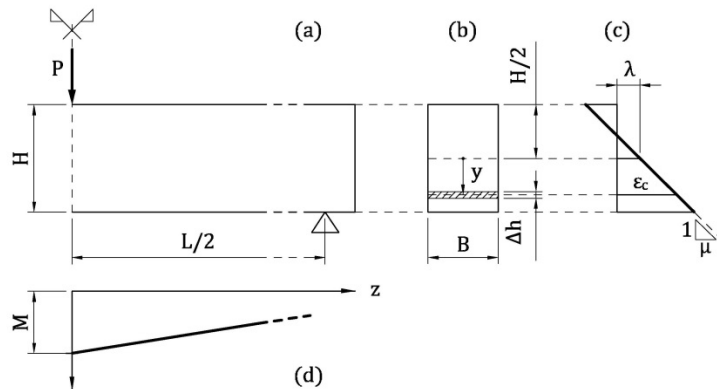


Figure 3.7: Modeling FRC beams in three point bending: (a) portion of the beam; (b) cross-section of the beam; (c) strain profile in midsection; (d) bending moment.

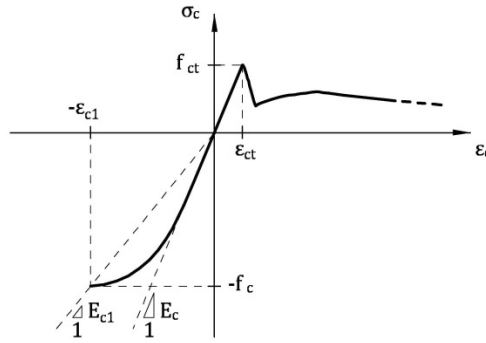


Figure 3.8: Complete stress vs. strain relationship of FRC.

3.2.4 Numerical evaluation of the flexural response of FRC beams

Due to the nonlinear response of FRC (Figure 3.8), the cross-sectional $M-\mu$ relationship of a beam in bending is defined through an iterative procedure. It is illustrated in the flow-chart of Figure 3.9 and summarized by the following points, where the subscript j refers to the coordinate $-H/2 \leq y_j \leq H/2$:

1. Assign a value to the curvature μ [Figure 3.7(c)].
2. Assume a trial value for the strain parameter λ [Figure 3.7(c)].
3. Divide H in n stripes of depth $\Delta h = H/n$ [Figure 3.7(b)], and define the ordinate $y_j = -H/2 + j \cdot \Delta h$ (where $j = 1, 2, \dots, n$).
4. For each j (or y_j) calculate:
 - The strain $\epsilon_{c,j}$ with Eq.(3.24).
 - The stress $\sigma_{c,j}$ corresponding to $\epsilon_{c,j}$ [Figure 3.8].
5. Compute the resultant R of the cross-sectional stresses [Eq.(3.25)].
6. If $R \neq 0$, then change λ and go to step 4.
7. Calculate the internal bending moment M [Eq.(3.26)].

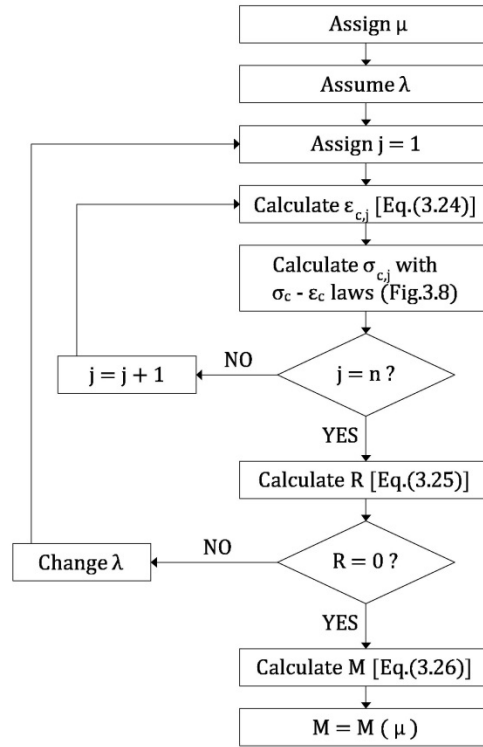


Figure 3.9: Flow-chart of the numerical procedure for evaluating the flexural response of FRC beams.

For a given μ , such procedure provides the corresponding bending moment M . Hence, the complete $M - \mu$ diagram can be obtained by varying the assigned curvature. Moreover, in analogy with the case of LRC beams, the diagram of bending moment vs. crack width at bottom level can also be plotted.

3.3 Analysis of the numerical results

The flexural behavior of 54 ideal FRC beams in three point bending is predicted by means of the procedure introduced in Section 3.2. Such beams, having $B = H/2$ (as in the case of LRC), are divided into 18 groups of three elements, with the same geometrical and material properties, but different fiber volume fractions V_f . Two depths ($H = 200$ and 400 mm) and three concretes ($f_c = 30, 45$ and 60 MPa) are taken into account, and $E_m = E_c$ is imposed. Steel fibers with fixed $L_f = 60$ mm, $f_u = 1,000$ MPa, and $E_f = 210$ GPa are used in each group. However, three different aspect ratios L_f/ϕ_f are considered (i.e., 40, 60, and 80).

Table 3.1 collects all the geometrical and mechanical properties of the 54 FRC beams. Each member is identified by the label SX_CYY_AZZ_W, in which the number X is related to the beam depth ($X = 1$ when $H = 200$ mm, and $X = 2$ when $H = 400$ mm), YY is the concrete compressive strength (in MPa), ZZ is the fiber aspect ratio, and W is a number (1, 2, or 3) related to the different V_f .

Table 3.1: Geometrical and mechanical properties of 54 ideal FRC beams.

Group	Beam	H (mm)	f_c (MPa)	L_f/ϕ_f	V_f (%)
F_1	S1_C30_A80_1	200	30	80	0.30
	S1_C30_A80_2				0.50
	S1_C30_A80_3				0.70
F_2	S1_C30_A60_1	200	30	60	0.40
	S1_C30_A60_2				0.60
	S1_C30_A60_3				0.80
F_3	S1_C30_A40_1	200	30	40	0.70
	S1_C30_A40_2				1.00
	S1_C30_A40_3				1.30
F_4	S1_C45_A80_1	200	45	80	0.30
	S1_C45_A80_2				0.50
	S1_C45_A80_3				0.70
F_5	S1_C45_A60_1	200	45	60	0.40
	S1_C45_A60_2				0.60
	S1_C45_A60_3				0.80
F_6	S1_C45_A40_1	200	45	40	0.70
	S1_C45_A40_2				1.00
	S1_C45_A40_3				1.30
F_7	S1_C60_A80_1	200	60	80	0.30
	S1_C60_A80_2				0.50
	S1_C60_A80_3				0.70
F_8	S1_C60_A60_1	200	60	60	0.40
	S1_C60_A60_2				0.60
	S1_C60_A60_3				0.80
F_9	S1_C60_A40_1	200	60	40	0.70
	S1_C60_A40_2				1.00
	S1_C60_A40_3				1.30
F_10	S2_C30_A80_1	400	30	80	0.35
	S2_C30_A80_2				0.55
	S2_C30_A80_3				0.75
F_11	S2_C30_A60_1	400	30	60	0.45
	S2_C30_A60_2				0.65
	S2_C30_A60_3				0.85

(Table follows in next page)

Group	Beam	H (mm)	f_c (MPa)	L_f/ϕ_f	V_f (%)
F_12	S2_C30_A40_1	400	30	40	0.75
	S2_C30_A40_2				1.05
	S2_C30_A40_3				1.35
F_13	S2_C45_A80_1	400	45	80	0.35
	S2_C45_A80_2				0.55
	S2_C45_A80_3				0.75
F_14	S2_C45_A60_1	400	45	60	0.45
	S2_C45_A60_2				0.65
	S2_C45_A60_3				0.85
F_15	S2_C45_A40_1	400	45	40	0.75
	S2_C45_A40_2				1.05
	S2_C45_A40_3				1.35
F_16	S2_C60_A80_1	400	60	80	0.35
	S2_C60_A80_2				0.55
	S2_C60_A80_3				0.75
F_17	S2_C60_A60_1	400	60	60	0.45
	S2_C60_A60_2				0.65
	S2_C60_A60_3				0.85
F_18	S2_C60_A40_1	400	60	40	0.75
	S2_C60_A40_2				1.05
	S2_C60_A40_3				1.35

The $M - \bar{w}$ curves referred to the beams of Group F_6 are reported in Figure 3.10(a). All the curves exhibit the relative maximum points corresponding to the effective cracking moment M_{cr^*} and the ultimate bending moment M_u . In the case of beam S1_C45_A40_1, the so-called deflection-softening response appears (i.e., $M_u < M_{cr^*}$), whereas the beam S1_C45_A40_2 approximately contains $V_{f,min}$ (i.e., $M_u \cong M_{cr^*}$). Finally, the deflection-hardening behavior can be recognized in the $M - \bar{w}$ diagram of beam S1_C45_A40_3 (i.e., $M_u > M_{cr^*}$). The values of M_{cr^*} and M_u , taken on the $M - \bar{w}$ diagrams of the 54 ideal FRC beams, are collected in Table 3.2.

Table 3.2 also reports the values of DI calculated for the ideal beams investigated herein with Eq.(1.6). Within the generic group of beams [e.g., Group F_6 in Figure 3.10(b)], a linear relationship between DI and V_f is attained, similarly to the linear function $DI - A_s$ obtained for LRC beams in Section 2.3. Hence, $V_{f,min}$ can be determined for each group of beams with the intersection between the $DI - V_f$ line and the axis $DI = 0$. The so-obtained values of minimum fiber volume fraction are reported in Table 3.2.

Table 3.2: Evaluation of minimum reinforcement in 54 ideal FRC beams.

Group	Beam	M_{cr*} (kNm)	M_u (kNm)	DI	$V_{f,min}$ (%)	r
F_1	S1_C30_A80_1	3.06	2.39	-0.22	0.44	0.68
	S1_C30_A80_2	3.29	3.61	0.10		1.13
	S1_C30_A80_3	3.56	4.86	0.36		1.58
F_2	S1_C30_A60_1	3.10	2.43	-0.22	0.59	0.67
	S1_C30_A60_2	3.28	3.33	0.02		1.01
	S1_C30_A60_3	3.49	4.27	0.22		1.35
F_3	S1_C30_A40_1	3.21	2.76	-0.14	0.90	0.77
	S1_C30_A40_2	3.44	3.69	0.07		1.11
	S1_C30_A40_3	3.69	4.65	0.26		1.44
F_4	S1_C45_A80_1	3.87	2.74	-0.29	0.48	0.63
	S1_C45_A80_2	4.09	4.30	0.05		1.05
	S1_C45_A80_3	4.31	5.85	0.36		1.47
F_5	S1_C45_A60_1	3.91	2.77	-0.29	0.64	0.63
	S1_C45_A60_2	4.10	3.93	-0.04		0.94
	S1_C45_A60_3	4.29	5.11	0.19		1.25
F_6	S1_C45_A40_1	4.05	3.18	-0.21	0.98	0.72
	S1_C45_A40_2	4.26	4.36	0.02		1.02
	S1_C45_A40_3	4.47	5.55	0.24		1.33
F_7	S1_C60_A80_1	4.54	3.08	-0.32	0.48	0.62
	S1_C60_A80_2	4.71	4.89	0.04		1.03
	S1_C60_A80_3	4.88	6.69	0.37		1.45
F_8	S1_C60_A60_1	4.58	3.10	-0.32	0.65	0.62
	S1_C60_A60_2	4.72	4.47	-0.05		0.93
	S1_C60_A60_3	4.87	5.83	0.20		1.24
F_9	S1_C60_A40_1	4.69	3.57	-0.24	0.99	0.71
	S1_C60_A40_2	4.87	4.94	0.02		1.01
	S1_C60_A40_3	5.05	6.32	0.25		1.32
F_10	S2_C30_A80_1	24.91	21.51	-0.14	0.44	0.79
	S2_C30_A80_2	26.82	31.39	0.17		1.25
	S2_C30_A80_3	29.12	41.38	0.42		1.70
F_11	S2_C30_A60_1	25.11	21.20	-0.16	0.59	0.76
	S2_C30_A60_2	26.66	28.52	0.07		1.10
	S2_C30_A60_3	28.39	36.10	0.27		1.44
F_12	S2_C30_A40_1	25.95	23.30	-0.10	0.90	0.83
	S2_C30_A40_2	27.82	30.77	0.11		1.17
	S2_C30_A40_3	29.91	38.49	0.29		1.50
F_13	S2_C45_A80_1	31.44	25.01	-0.20	0.48	0.73
	S2_C45_A80_2	33.19	37.51	0.13		1.15
	S2_C45_A80_3	35.56	49.90	0.40		1.57

(Table follows in next page)

Group	Beam	M_{cr^*} (kNm)	M_u (kNm)	DI	$V_{f,min}$ (%)	r
F_14	S2_C45_A60_1	31.70	24.44	-0.23	0.64	0.70
	S2_C45_A60_2	33.16	33.83	0.02		1.02
	S2_C45_A60_3	34.62	43.23	0.25		1.33
F_15	S2_C45_A40_1	32.65	26.97	-0.17	0.98	0.77
	S2_C45_A40_2	34.37	36.42	0.06		1.07
	S2_C45_A40_3	36.02	46.00	0.28		1.38
F_16	S2_C60_A80_1	36.64	28.27	-0.23	0.49	0.72
	S2_C60_A80_2	37.97	42.76	0.13		1.13
	S2_C60_A80_3	40.88	57.09	0.40		1.54
F_17	S2_C60_A60_1	36.86	27.54	-0.25	0.65	0.70
	S2_C60_A60_2	38.08	38.46	0.01		1.01
	S2_C60_A60_3	39.22	49.35	0.26		1.32
F_18	S2_C60_A40_1	37.81	30.39	-0.20	0.99	0.76
	S2_C60_A40_2	39.24	41.39	0.05		1.06
	S2_C60_A40_3	41.08	52.41	0.28		1.36

When $V_{f,min}$ is known for each group, the ratios $r = V_f / V_{f,min}$ can be computed for the 54 ideal FRC beams (Table 3.2). Then, the couples $[DI - r]$ can be compared with those obtained through Eq.(3.4). Also in the case of FRC beams, a linear dependence of DI on r can be noticed in Figure 3.11, which appears well approximated by the proposed relationship. In other words, for all the FRC beams, the evaluation of DI can be performed with Eq.(3.4), regardless of their size and material properties.

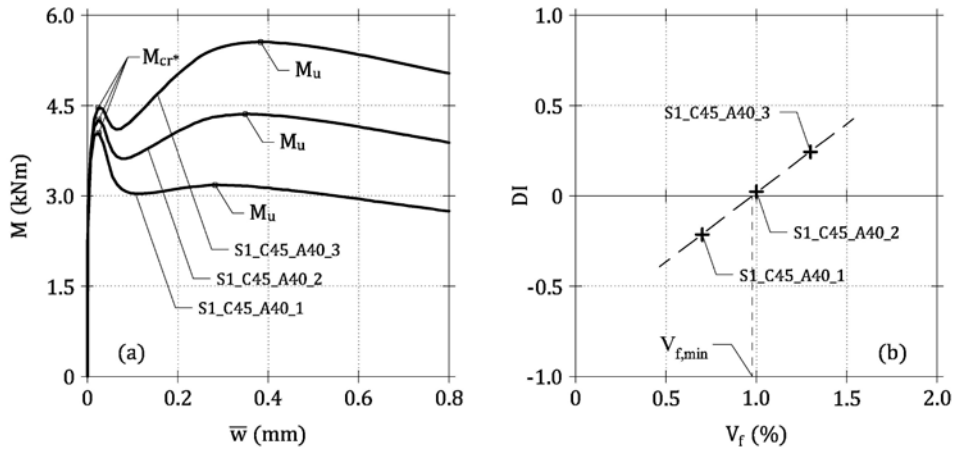


Figure 3.10: Application of the general model to the ideal beams of Group F_6: (a) $M - \bar{w}$ curves; (b) $DI - V_f$ relationship and evaluation of $V_{f,min}$.

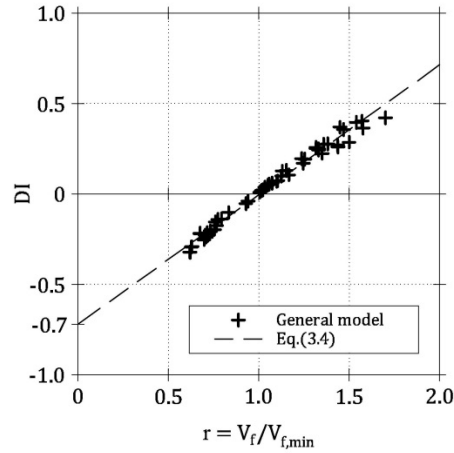


Figure 3.11: Proposed DI - r linear relationship [Eq.(3.4)] in comparison with the results of the general model.

3.4 Comparison with the experimental results

To verify the accuracy of the proposed linear relationship, the values of DI are computed for 61 FRC beams studied in some experimental campaigns available in the literature, and then compared with the predictions of Eq.(3.4). In these experimental investigations, notched beams were tested in three point bending by Alberti et al. (2014a,b), Aydın (2013), Barros et al. (2005), Lee and Barr (2004), and Salvador et al. (2015). Moreover, four point bending tests on un-notched beams were performed by Banthia and Gupta (2004), Jones et al. (2008), Kovar and Foglar (2015), Michels et al. (2013), Mobasher et al. (2014), Soetens and Matthys (2014), and Wu (2002). Finally, one-way un-notched plates were tested in three point bending by Fantilli et al. (2014).

Specifically, 61 FRC members divided into 20 groups (whose B , H , and f_c are collected in Table 3.3) are analyzed. In each single group, at least two FRC elements, having the same geometrical and mechanical properties of material (and without the presence of rebar), are considered. The beams of each group, reinforced with the different fiber volume fractions reported in Table 3.4, always fail in tension. Indeed, when high V_f are used, compressive strains in a FRC cross-section (Figure 3.1) can localize (Uchida et al. 2007), and the sole ascending branch of the Sargin's parabola (Figure 3.8) is no longer representative of the FRC behavior.

Table 3.3: Geometrical and mechanical properties of 61 FRC beams tested by other Authors.

Group	Beam	B (mm)	H (mm)	L (mm)	f_c (MPa)	References
F_I	P3	100	67	300	39	Alberti et al. (2014a)
	P4.5				38	
	P6				37	
	P10a				37	
F_II	S33	100	67	300	42	Alberti et al. (2014b)
	S49				43	
F_III	NSC20NSF	100	67	500	36	Aydın (2013)
	NSC60NSF				37	
F_IV	NSC20HSF	100	67	500	36	Aydın (2013)
	NSC60HSF				36	
F_V	HSC20NSF	100	67	500	81	Banthia and Gupta (2004)
	HSC60NSF				80	
F_VI	N2	100	100	300	97.4	Banthia and Gupta (2004)
	N3				92.6	
	N4				86.6	
F_VII	F80/60_Cf10	150	125	500	33.0	Barros et al. (2005)
	F80/60_Cf20					
	F80/60_Cf30					
F_VIII	Mix_1_1	1000	100	900	21.5	Fantilli et al. (2014)
	Mix_1_2					
	Mix_1_3					
	Mix_2_1				23.4	
	Mix_2_2					
	Mix_2_3					
	Mix_3_1				22.9	
	Mix_3_2					
Mix_3_3						
F_IX	50C(40)	100	50	450	54.0	Jones et al. (2008)
	50C(80)					
F_X	75C(40)	100	75	450	54.0	Jones et al. (2008)
	75C(80)					
F_XI	FRC01	150	150	600	45.4	Kovar and Foglar (2015)
	FRC02				41.9	
F_XII	C25/30(25)	150	125	500	33.0	Lee and Barr (2004)
	C25/30(75)					

(Table follows in next page)

Group	Beam	B (mm)	H (mm)	L (mm)	f_c (MPa)	References
F_XIII	0.20(A)	150	150	600	50.2	Michels et al. (2013)
	0.52(A)				48.7	
	0.65(A)				51.7	
	0.91(A)				52.7	
F_XIV	S13-HL-28d	150	150	450	28	Mobasher et al. (2014)
	S26-HL-28d					
	S39-HL-28d					
F_XV	PPA_0.33	150	125	450	33.4	Salvador et al. (2015)
	PPA_0.50				34.1	
	PPA_0.66				33.3	
F_XVI	PPB_0.33	150	125	450	34.5	Salvador et al. (2015)
	PPB_0.50				33.1	
	PPB_0.66				35.9	
F_XVII	ACO_0.19	150	125	450	35.5	Soetens and Matthys (2014)
	ACO_0.32				32.1	
	ACO_0.45				32.9	
F_XVIII	4P-LN-20	150	150	450	42.7	Soetens and Matthys (2014)
	4P-LN-40				48.8	
F_XIX	DWP_0.2	100	100	300	-	Wu (2002)
	DWP_0.5					
	DWP_1					
	DWP_1.5					
F_XX	FP_0.2	100	100	300	-	Wu (2002)
	FP_0.5					
	FP_1					
	FP_1.5					

Unlike in the numerical analyses described in Section 3.3, fibers of different shapes and materials are taken into account. To describe them, two letters are reported in Table 3.4, referring to geometry (S = straight, H = with hooked ends, F = with flat ends, U = undulated) and material (S = steel, P = plastic).

The experimental values of the effective cracking load P_{cr^*} and of the ultimate load P_u referred to all the FRC beams are collected in Table 3.5. According to Eq.(1.6), these loads are necessary to compute DI , which is also reported in the Table. The ductility indexes calculated for two groups of beams, both comprising three members reinforced with different amounts of fibers, can be observed in the $DI - V_f$ diagrams of Figure 3.12. Specifically, Figure 3.12(a) is referred to the FRC beams of Group F_VI, tested by Banthia and Gupta (2004), and Figure 3.12(b) to those of Group F_VII by Barros et al. (2005). Both the diagrams exhibit a linear increment of DI with V_f , in agreement with the numerical results shown in Figure

3.10(b). Accordingly, for all the groups, $V_{f,\min}$ can be graphically determined [Figure 3.10(b) and Figure 3.12]. The corresponding values, and those of the reinforcement ratio $r = V_f / V_{f,\min}$ as well, are collected in Table 3.5.

Table 3.4: Geometrical and mechanical properties of the fiber used in 61 beams tested by other Authors.

Group	Beam	Fibers	f_u (MPa)	L_f / ϕ_f	V_f (%)	References
F_I	P3	S_P	500	66	0.33	Alberti et al. (2014a)
	P4.5				0.49	
	P6				0.66	
	P10a				1.10	
F_II	S33	H_S	1100	64	0.33	Alberti et al. (2014b)
	S49				0.49	
F_III	NSC20NSF	H_S	1100	55	0.25	Aydm (2013)
	NSC60NSF				0.76	
F_IV	NSC20HSF	H_S	2000	55	0.25	Aydm (2013)
	NSC60HSF				0.76	
F_V	HSC20NSF	H_S	1100	55	0.25	Aydm (2013)
	HSC60NSF				0.76	
F_VI	N2	F_S	1150	50	0.50	Banthia and Gupta (2004)
	N3				0.75	
	N4				1.00	
F_VII	F80/60_Cf10	H_S	1100	80	0.13	Barros et al. (2005)
	F80/60_Cf20				0.25	
	F80/60_Cf30				0.38	
F_VIII	Mix_1_1	S_P	620	113	0.36	Fantilli et al. (2014)
	Mix_1_2				0.36	
	Mix_1_3				0.36	
	Mix_2_1				0.74	
	Mix_2_2				0.74	
	Mix_2_3				0.74	
	Mix_3_1				1.10	
Mix_3_2	1.10					
F_IX	50C(40)	H_S	1150	60	0.51	Jones et al. (2008)
	50C(80)				1.02	
F_X	75C(40)	H_S	1150	60	0.51	Jones et al. (2008)
	75C(80)				1.02	

(Table follows in next page)

Group	Beam	Fibers	f_u (MPa)	L_f/ϕ_f	V_f (%)	References
F_XI	FRC01 FRC02	S_P	600	159	0.50 1.00	Kovar and Foglar (2015)
F_XII	C25/30(25) C25/30(75)	H_S	1160	65	0.32 0.96	Lee and Barr (2004)
F_XIII	0.20(A) 0.52(A) 0.65(A) 0.91(A)	U_S	1450	60	0.20 0.52 0.65 0.91	Michels et al. (2013)
F_XIV	S13-HL-28d S26-HL-28d S39-HL-28d	H_S	2300	167	0.17 0.33 0.50	Mobasher et al. (2014)
F_XV	PPA_0.33 PPA_0.50 PPA_0.66	S_P	570- 660	169	0.33 0.50 0.66	Salvador et al. (2015)
F_XVI	PPB_0.33 PPB_0.50 PPB_0.66	S_P	640	60	0.33 0.50 0.66	
F_XVII	ACO_0.19 ACO_0.32 ACO_0.45	H_S	1100	80	0.19 0.32 0.45	
F_XVIII	4P-LN-20 4P-LN-40	H_S	1236	80	0.25 0.51	Soetens and Matthys (2014)
F_XIX	DWP_0.2 DWP_0.5 DWP_1 DWP_1.5	S_P	400	150	0.20 0.50 1.00 1.50	Wu (2002)
F_XX	FP_0.2 FP_0.5 FP_1 FP_1.5	S_P	400	89	0.20 0.50 1.00 1.50	

A couple of values $[DI, r]$, referred to a single beam, defines a point in the non-dimensional diagram of Figure 3.13, where the proposed linear function [i.e., Eq.(3.4)] is also reported. All the experimental data reveal the existence of a linear relationship between DI and r . Nevertheless, the slope $\zeta = 0.8$ given by the least square approximation of the experimental results is higher than the value obtained in Section 3.1, and reported in Figure 3.13.

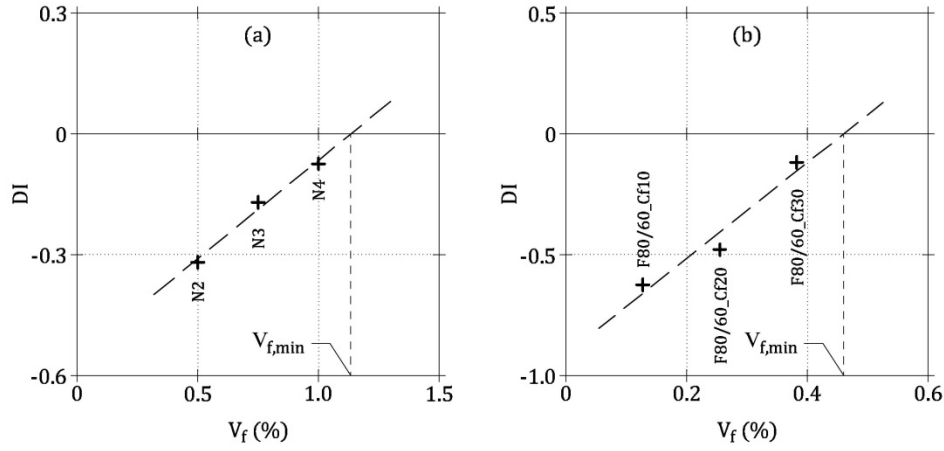


Figure 3.12: $DI-V_f$ relationships and evaluation of $V_{f,min}$ in FRC beams tested in some experimental campaigns: (a) beams of Group F_VI tested by Banthia and Gupta (2004); (b) beams of Group F_VII tested by Barros et al. (2005).

Table 3.5: Evaluation of minimum reinforcement in 61 FRC beams tested in some experimental campaigns available in literature.

Group	Beam	P_{cr^*} (kN)	P_u (kN)	DI	$V_{f,min}$ (%)	r	References
F_I	P3	5.67	0.84	-0.85	1.46	0.23	Alberti et al. (2014a)
	P4.5	5.66	1.94	-0.66		0.34	
	P6	5.99	3.23	-0.46		0.45	
	P10a	5.18	3.65	-0.29		0.75	
F_II	S33	5.975	4.01	-0.33	0.48	0.68	Alberti et al. (2014b)
	S49	5.766	5.83	0.01		1.01	
F_III	NSC20NSF	2.34	1.30	-0.44	0.66	0.39	
	NSC60NSF	2.45	2.74	0.12		1.16	
F_IV	NSC20HSF	2.41	1.36	-0.44	0.59	0.43	Aydm (2013)
	NSC60HSF	2.75	3.38	0.23		1.30	
F_V	HSC20NSF	3.79	1.31	-0.65	0.54	0.47	
	HSC60NSF	3.84	5.76	0.50		1.41	
F_VI	N2	25.0	17.0	-0.32	1.13	0.44	Banthia and Gupta (2004)
	N3	27.5	22.8	-0.17		0.66	
	N4	21.1	19.5	-0.07		0.88	
F_VII	F80/60_Cf10	14.4	5.4	-0.62	0.46	0.28	Barros et al. (2005)
	F80/60_Cf20	15.9	8.3	-0.48		0.55	
	F80/60_Cf30	13.6	12.0	-0.12		0.83	

(Table follows in next page)

Group	Beam	P_{cr*} (kN)	P_u (kN)	DI	$V_{f,min}$ (%)	r	References
F_VIII	Mix_1_1	18.2	11.5	-0.37	1.02	0.36	Fantilli et al. (2014)
	Mix_1_2	18.6	12.4	-0.33		0.36	
	Mix_1_3	20.6	13.2	-0.36		0.36	
	Mix_2_1	21.3	18.8	-0.12		0.72	
	Mix_2_2	22.5	15.6	-0.31		0.72	
	Mix_2_3	23.1	19.5	-0.16		0.72	
	Mix_3_1	22.8	24.0	0.05		1.08	
	Mix_3_2	21.5	23.2	0.08		1.08	
	Mix_3_3	20.4	21.6	0.06	1.08		
F_IX	50C(40)	2.3	1.9	-0.20	0.73	0.70	Jones et al. (2008)
	50C(80)	2.9	3.6	0.26		1.39	
F_X	75C(40)	6.5	5.0	-0.24	0.74	0.69	
	75C(80)	6.9	8.9	0.29		1.38	
F_XI	FRC01	30.6	8.6	-0.72	2.70	0.19	Kovar and Foglar (2015)
	FRC02	29.9	13.3	-0.56		0.37	
F_XII	C25/30(25)	13.8	7.41	-0.46	0.73	0.44	Lee and Barr (2004)
	C25/30(75)	16.2	20.4	0.26		1.31	
F_XIII	0.20(A)	25.8	12.1	-0.53	0.64	0.31	Michels et al. (2013)
	0.52(A)	28.2	29.2	0.03		0.81	
	0.65(A)	29.0	29.8	0.03		1.01	
	0.91(A)	31.6	37.3	0.18		1.42	
F_XIV	S13-HL-28d	23.3	5.8	-0.75	0.56	0.30	Mobasher et al. (2014)
	S26-HL-28d	26.1	15.2	-0.42		0.59	
	S39-HL-28d	25.1	21.9	-0.13		0.89	
F_XV	PPA_0.33	15.6	5.3	-0.66	1.55	0.21	
	PPA_0.50	16.0	6.8	-0.58		0.32	
	PPA_0.66	16.0	8.3	-0.48		0.42	
F_XVI	PPB_0.33	14.0	3.9	-0.72	1.40	0.24	Salvador et al. (2015)
	PPB_0.50	14.7	6.2	-0.58		0.36	
	PPB_0.66	15.8	7.9	-0.50		0.47	
F_XVII	ACO_0.19	14.6	6.4	-0.56	0.50	0.38	
	ACO_0.32	15.0	9.5	-0.37		0.64	
	ACO_0.45	16.4	15.2	-0.07		0.91	
F_XVIII	4P-LN-20	3.6	3.3	-0.06	0.31	0.83	Soetens and Matthys (2014)
	4P-LN-40	4.8	5.9	0.23		1.66	
F_XIX	DWP_0.2	12.0	3.9	-0.67	2.05	0.10	Wu (2002)
	DWP_0.5		5.3	-0.56		0.24	
	DWP_1		8.1	-0.33		0.49	
	DWP_1.5		9.3	-0.23		0.73	
F_XX	FP_0.2	13.6	4.0	-0.71	2.89	0.07	
	FP_0.5		5.7	-0.58		0.17	
	FP_1		6.9	-0.49		0.35	
	FP_1.5		8.8	-0.36		0.52	

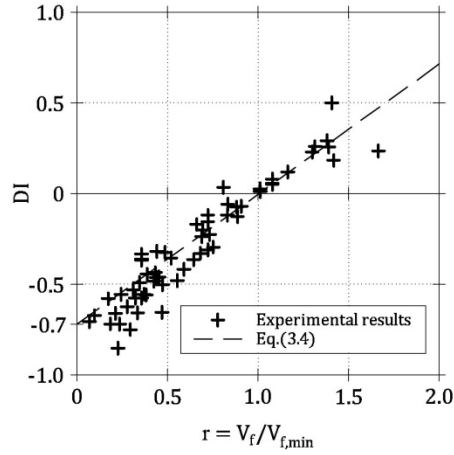


Figure 3.13: Proposed DI - r linear relationship [Eq.(3.4)] in comparison with the results of some experimental campaigns.

3.5 Discussion of the results

Based on the previous numerical and experimental results, the brittle/ductile behavior of FRC beams can be assessed through the non-dimensional parameters DI and r (Figure 3.2), as in the case of LRC beams studied in Chapter 2. Indeed, both Figure 3.11 and Figure 3.13 clearly show the linear dependence of DI on r , with a slope slightly higher than the value 0.7 previously determined.

The proposed linear relationship [i.e., Eq.(3.4)] seems to be generally valid, regardless of geometrical dimensions and material properties, as it fits the numerical results of 54 ideal beams and 61 real members in a wide range of geometrical and mechanical properties. The general applicability of this approach can be ascribed to the non-dimensional definition of both DI and r , as recently observed by Facconi and Minelli (2017) in the case of a displacement ratio used for concrete members reinforced with sole fibers. On the other hand, the present DI - r relationship, in the general form of Eq.(1.7), allows to propose a comprehensive strategy for all the types of concrete elements.

Moreover, it can be asserted that the assumptions previously used to calculate the pull-out response of a fiber (i.e., fiber symmetrically and orthogonally positioned with respect to the crack, L_f taken as the characteristic length of the FRC in tension, and a single bond-slip relationship for all the types of the fiber) have a limited influence on the assessment of DI in FRC beams. Indeed, such parameters seem to have the same effects on both P_{cr}^* and P_u in Eq.(1.6).

As in LRC, Eq.(3.4) can be used in combination with some experimental results on few full-scale beams to compute $V_{f,\min}$, through a design-by-testing approach. Specifically, the procedure for FRC beams can be summarized by a formula formally identical to Eq.(2.22):

$$V_{f,\min} = \frac{\zeta \cdot V_f}{DI + \zeta} \quad (3.27)$$

where V_f , DI = fiber volume fraction and ductility index of the tested beam.

Chapter 4

Minimum hybrid reinforcement in HRC beams

4.1 Simplified model for HRC beams in bending

According to Falkner and Henke (2005), the flexural response of an HRC beam cannot be evaluated, in general, as a simple sum of the effects related to the area of rebar A_s and to the fiber volume fraction V_f . However, the superposition of the effects due to the two reinforcing systems becomes possible at ultimate limit state, when large crack widths are attained in the cementitious matrix. As a matter of fact, in such situation, the fracture mechanics of concrete in tension has no longer influence. This statement has been experimentally verified by Falkner and Henke (2005), which calculated the effect of fiber-reinforcement on the flexural bearing capacity of the HRC beam illustrated in Figure 4.1(a) by subtracting the response of the hybrid beam (iii) and that of the LRC beam (ii) reinforced with the same A_s [Figure 4.1(b)]. Curve (iv) is the result of such subtraction, whereas curve (i) is the flexural response of a FRC beam reinforced with the same V_f used in the previous HRC beam [Figure 4.1(b)]. The words used by Falkner and Henke (2005) clearly describe the phenomenon: “As curve (iv) is derived by subtraction of measured values of combined and pure bar reinforced members, it is free from any fracture mechanical effects. At larger crack widths both curves (i) and (iv) converge”.

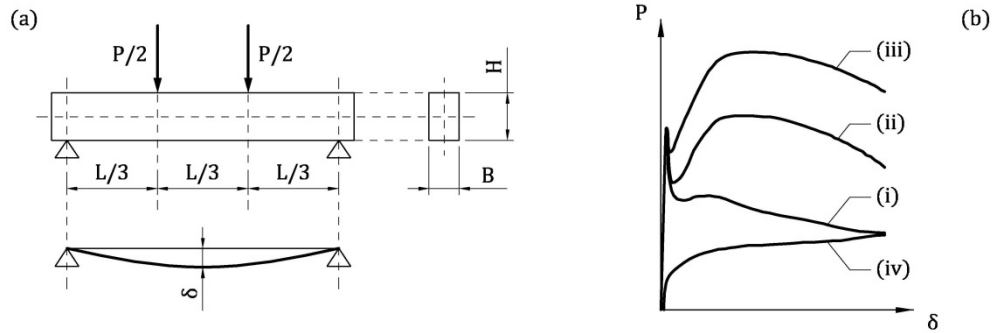


Figure 4.1: Experimental investigation performed by Falkner and Henke (2005): (a) four point bending test; (b) applied load $\nu s.$ midspan deflection curves of FRC beam (i), LRC beam (ii), HRC beam (iii), and difference (iv) = (iii) - (ii).

Thus, by inverting the relationship $(i) = (iii) - (ii)$ [valid for high deflections δ in Figure 4.1(b)], it can be argued that, if the failure in tension occurs, the ultimate bearing capacity of an HRC beam can be evaluated with a superposition of the effects given by the two reinforcing systems [i.e., $(iii) = (ii) + (i)$]. Accordingly, the ultimate bending moment M_u of the HRC cross-section depicted in Figure 4.2 can be easily obtained by superposing the moment capacity formulae already used for LRC and FRC members [i.e., Eq.(2.1) and Eq.(3.1), respectively], as the cohesive stresses of concrete have not influence for large crack widths:

$$M_u = A_s \cdot f_y \cdot Z_{LRC} + A_{s,eq} \cdot f_y \cdot Z_{FRC} \quad (4.1)$$

In other words, the equivalent area of steel rebar $A_{s,eq}$, which represents V_f , is introduced by assuming a unique yielding strength f_y for both real and equivalent rebar (Figure 4.2). Due to the different stress distribution (Figure 4.2), two distinct lever arms for LRC and FRC cross-sections (i.e., Z_{LRC} and Z_{FRC} , respectively), can be recognized in Eq.(4.1).

As in the cases of LRC and FRC beams, the effective cracking moment M_{cr^*} of an HRC cross-section is difficult to assess. Therefore, it is again evaluated through the moment capacity formula of LRC, for $A_s \rightarrow A_{s,min}$ [Eq.(2.2) and Eq.(3.2)]. Accordingly, also in this case, M_{cr^*} is assumed to be constant with respect to the amount of reinforcement (i.e., rebar and fibers). However, the influence of A_s and V_f on the effective cracking moment is significantly lower than that of the same reinforcements on M_u (Gorino et al. 2016), hence the following formula can be also adopted for HRC beams:

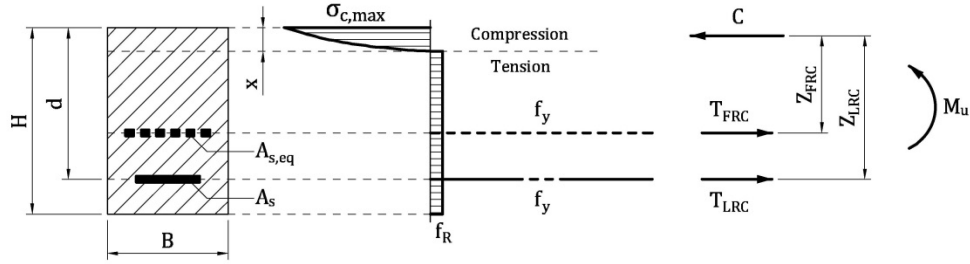


Figure 4.2: Simplified state of stress in an HRC cross-section at ultimate limit state.

$$M_{cr^*} = A_{s,min} \cdot f_y \cdot Z_{LRC} \quad (4.2)$$

Based on the superposition of the effects related to A_s and V_f in ultimate conditions, the reinforcement ratio $r = A_s/A_{s,min} + V_f/V_{f,min}$ is assumed for HRC members (Gorino et al. 2016). By substituting Eq.(4.1) and Eq.(4.2) into Eq.(1.8), the coefficient ζ for HRC beams can be evaluated as follows:

$$\zeta = \frac{\partial}{\partial r} \left(\frac{A_s}{A_{s,min}} + \frac{A_{s,eq}}{A_{s,min}} \cdot \frac{Z_{FRC}}{Z_{LRC}} \right)_{r=1} \quad (4.3)$$

Eq.(4.3) can be considered the general formula of ζ , as it includes the particular cases of LRC and FRC beams [i.e., Eq.(2.3) and Eq.(3.3)]. In fact, if $A_{s,eq} \rightarrow 0$, the slope $\zeta = 1$ of LRC beams can be found [i.e., Eq.(2.3)]. On the other hand, $\zeta = 0.7$ is obtained when $A_s \rightarrow 0$, as it happens in a FRC cross-section [i.e., Eq.(3.3)]. Conversely, in presence of both A_s and $A_{s,eq}$, the slope can vary, depending on the amounts of rebar and fibers. In particular, two reinforcement ratios can be noticed in Eq.(4.3), i.e., $A_s/A_{s,min}$ and $A_{s,eq}/A_{s,min}$ (or, equivalently, $V_f/V_{f,min}$) used in LRC and FRC beams, respectively. Thus, to assess the brittle/ductile behavior of an HRC member in bending, firstly, it is needed to individuate the minimum reinforcements $A_{s,min}$ and $V_{f,min}$ which would be necessary if the same member were reinforced with only rebar [Eq.(2.22)] and with only fibers [Eq.(3.27)], separately.

Since the slopes ζ evaluated in Section 2.1 for LRC beams (i.e., $\zeta = 1$) and in Section 3.1 for FRC beams (i.e., $\zeta = 0.7$) appear as limit cases of the previous Eq.(4.3), the $DI-r$ function of whichever HRC member should fall within the envelope delimited by the following equations (Figure 4.3):

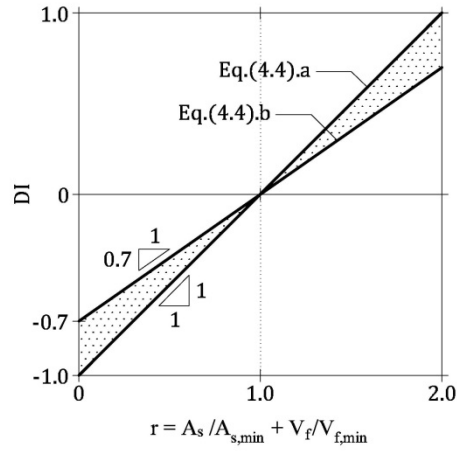


Figure 4.3: $DI - r$ envelope for HRC beams.

$$DI = r - 1 \quad (4.4).a$$

$$DI = 0.7 \cdot (r - 1) \quad (4.4).b$$

4.2 General model for HRC beams in bending

For predicting the flexural behavior of an HRC beam, the general models for LRC and FRC members need to be combined, due to the simultaneous presence of rebar and fibers as a reinforcement. To be more precise, the HRC beam is studied as a LRC member, but the behavior of the cracked cementitious matrix is defined by an ideal tie as in the model for FRC beams (Figure 4.4).

This combined model is similar to that recently proposed by Barros et al. (2015), where the flexural behavior of an HRC element is studied by knowing the stress vs. crack width relationship of FRC in tension, and by assuming a bond-slip model to be applied at the interface between rebar and concrete. However, in the present case it is not necessary to perform direct tensile tests, or a back-analysis on the results of bending tests, to describe the post-cracking tensile behavior of FRC. It must be remarked that, due to the low amounts of rebar and fibers considered in the following analyses, which are comparable with the minimum reinforcement, the concrete crushing failure cannot occur. Accordingly, the softening behavior of concrete in compression, taken into account by Barros et al. (2015), is not considered herein.

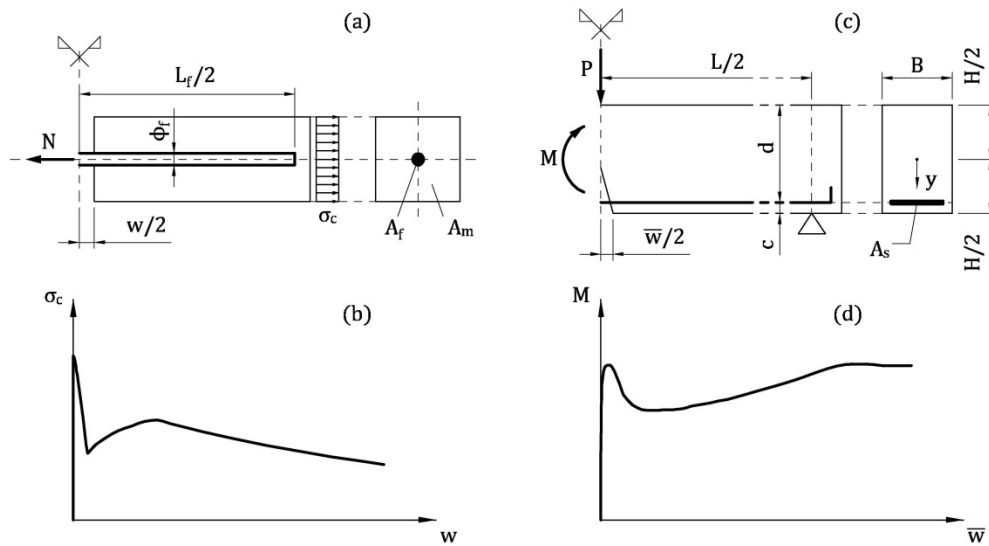


Figure 4.4: General model for predicting the flexural response of HRC beams: (a) ideal tie representing the cracked FRC; (b) $\sigma_c - w$ relationship of FRC; (c) HRC beam in three point bending in presence of a single crack; (d) $M - \bar{w}$ curve of an HRC beam in bending.

The flexural behavior of an HRC member in three point bending, which fails in presence of a single flexural crack, is similar to that of a LRC beam. Thus, it can be predicted with the general model described in Section 2.2.1. Specifically, the stress vs. strain behavior of uncracked concrete is modelled with the ascending branch of the Sargin's parabola in compression and the linear elastic law in tension, whereas an elastic-perfectly plastic constitutive relationship is adopted for steel rebar (*fib* 2012a). The post-cracking tensile behavior of the FRC matrix, which composes the HRC beam, can be evaluated with the same ideal tie already described in Section 3.2.1, and depicted in Figure 4.4(a). The pull-out mechanism of the ideal tie provides the stress vs. crack width relationship of FRC [Figure 4.4(b)]. Finally, the bond-slip mechanism between rebar and concrete is described with the model proposed by Model Code 2010 (*fib* 2012a). By means of an iterative procedure, analogous to that shown in Figure 2.7, the combined model allows to compute the internal bending moment in midsection M associated to a given crack width \bar{w} at the intrados of the beam illustrated in Figure 4.4(c). Therefore, when the crack width is increased, the complete $M - \bar{w}$ curve can be obtained [Figure 4.4(d)].

4.3 Analysis of the numerical results

The general model illustrated in Section 4.2 is adopted to compute the $M - \bar{w}$ curves of 108 ideal HRC beams in three point bending. Table 4.1 summarizes the characteristics of all the beams, which are divided into 36 groups of three members, having the same geometrical and material properties, but different amounts of rebar and fibers. In particular, for 18 groups the area of rebar changes and the fiber volume fraction is constant, whereas in the remaining groups A_s is the same and V_f varies.

As in the case of LRC (Section 2.3), the width B and the span L of the beams are one half and six times the depth H (assuming the values of 200 and 400 mm), respectively. Three compressive strengths of concrete are considered (i.e., $f_c = 30, 45, \text{ and } 60$ MPa), and the same properties of steel rebar are assumed in all the groups (i.e., $f_y = 450$ MPa, and $E_s = 210$ GPa). The fibers, having $L_f = 60$ mm, $f_u = 1,000$ MPa, and $E_f = 210$ GPa, show a variable aspect ratio $L_f / \phi_f = 40, 60, \text{ and } 80$. These geometrical and material properties are the same used to investigate the LRC beams in Section 2.3, and the FRC beams in Section 3.3. Hence, for each group of HRC members, the minimum area of rebar $A_{s,\min}$ and the minimum fiber volume fraction $V_{f,\min}$ are known (Table 2.2 and Table 3.2, respectively).

The 108 ideal beams of Table 4.1 are labelled by means of the acronym SX_CYY_AZZ_φW_K, where X depends on the beam depth ($X = 1$ for $H = 200$ mm, and $X = 2$ for $H = 400$ mm), YY is the concrete strength (in MPa), ZZ is the fiber aspect ratio, W is the rebar diameter (in mm), and K is a number (1, 2, or 3) associated to the different amount of hybrid reinforcement inside a beam.

Figure 4.5(a) reports the $M - \bar{w}$ curves referred to the beams of Group H_9, whereas those of Group H_10 are shown in Figure 4.5(c). In all the curves, the effective cracking moment M_{cr^*} and the ultimate bending moment M_u can be detected. Both the beams S1_C45_A60_φ5_1 and S1_C45_A60_φ6_1 show a brittle response, as $M_u < M_{cr^*}$. On the other hand, in beams S1_C45_A60_φ5_2 and S1_C45_A60_φ6_2 the amounts of rebar and fibers are near to a minimum value of the hybrid reinforcement, because $M_u \cong M_{cr^*}$. Finally, the $M - \bar{w}$ curves of beams S1_C45_A60_φ5_3 and S1_C45_A60_φ6_3 describe a typical ductile behavior with $M_u > M_{cr^*}$.

Table 4.1: Geometrical and mechanical properties of 108 ideal HRC beams.

Group	Beam	H (mm)	f_c (MPa)	L_f/ϕ_f	ϕ_s (mm)	A_s (mm ²)	V_f (%)
H_1	S1_C30_A80_φ4_1	200	30	80	4	13	0.15
	S1_C30_A80_φ4_2					25	0.15
	S1_C30_A80_φ4_3					38	0.15
H_2	S1_C30_A80_φ5_1	200	30	80	5	20	0.05
	S1_C30_A80_φ5_2					20	0.20
	S1_C30_A80_φ5_3					20	0.35
H_3	S1_C30_A60_φ4_1	200	30	60	4	13	0.25
	S1_C30_A60_φ4_2					25	0.25
	S1_C30_A60_φ4_3					38	0.25
H_4	S1_C30_A60_φ5_1	200	30	60	5	20	0.15
	S1_C30_A60_φ5_2					20	0.30
	S1_C30_A60_φ5_3					20	0.45
H_5	S1_C30_A40_φ4_1	200	30	40	4	13	0.30
	S1_C30_A40_φ4_2					25	0.30
	S1_C30_A40_φ4_3					38	0.30
H_6	S1_C30_A40_φ5_1	200	30	40	5	20	0.10
	S1_C30_A40_φ5_2					20	0.40
	S1_C30_A40_φ5_3					20	0.70
H_7	S1_C45_A80_φ5_1	200	45	80	5	20	0.15
	S1_C45_A80_φ5_2					39	0.15
	S1_C45_A80_φ5_3					59	0.15
H_8	S1_C45_A80_φ6_1	200	45	80	6	28	0.10
	S1_C45_A80_φ6_2					28	0.25
	S1_C45_A80_φ6_3					28	0.40
H_9	S1_C45_A60_φ5_1	200	45	60	5	20	0.10
	S1_C45_A60_φ5_2					39	0.10
	S1_C45_A60_φ5_3					59	0.10
H_10	S1_C45_A60_φ6_1	200	45	60	6	28	0.05
	S1_C45_A60_φ6_2					28	0.25
	S1_C45_A60_φ6_3					28	0.45
H_11	S1_C45_A40_φ5_1	200	45	40	5	20	0.15
	S1_C45_A40_φ5_2					39	0.15
	S1_C45_A40_φ5_3					59	0.15
H_12	S1_C45_A40_φ6_1	200	45	40	6	28	0.10
	S1_C45_A40_φ6_2					28	0.40
	S1_C45_A40_φ6_3					28	0.70

(Table follows in next page)

Group	Beam	H (mm)	f_c (MPa)	L_d/ϕ_r	ϕ_s (mm)	A_s (mm ²)	V_f (%)
H_13	S1_C60_A80_φ5_1	200	60	80	5	20	0.15
	S1_C60_A80_φ5_2					39	0.15
	S1_C60_A80_φ5_3					59	0.15
H_14	S1_C60_A80_φ6_1	200	60	80	6	28	0.10
	S1_C60_A80_φ6_2					28	0.25
	S1_C60_A80_φ6_3					28	0.40
H_15	S1_C60_A60_φ5_1	200	60	60	5	20	0.25
	S1_C60_A60_φ5_2					39	0.25
	S1_C60_A60_φ5_3					59	0.25
H_16	S1_C60_A60_φ6_1	200	60	60	6	28	0.10
	S1_C60_A60_φ6_2					28	0.35
	S1_C60_A60_φ6_3					28	0.60
H_17	S1_C60_A40_φ5_1	200	60	40	5	20	0.30
	S1_C60_A40_φ5_2					39	0.30
	S1_C60_A40_φ5_3					59	0.30
H_18	S1_C60_A40_φ6_1	200	60	40	6	28	0.10
	S1_C60_A40_φ6_2					28	0.50
	S1_C60_A40_φ6_3					28	0.90
H_19	S2_C30_A80_φ8_1	400	30	80	8	50	0.10
	S2_C30_A80_φ8_2					101	0.10
	S2_C30_A80_φ8_3					151	0.10
H_20	S2_C30_A80_φ10_1	400	30	80	10	79	0.05
	S2_C30_A80_φ10_2					79	0.20
	S2_C30_A80_φ10_3					79	0.35
H_21	S2_C30_A60_φ8_1	400	30	60	8	50	0.15
	S2_C30_A60_φ8_2					101	0.15
	S2_C30_A60_φ8_3					151	0.15
H_22	S2_C30_A60_φ10_1	400	30	60	10	79	0.05
	S2_C30_A60_φ10_2					79	0.20
	S2_C30_A60_φ10_3					79	0.35
H_23	S2_C30_A40_φ8_1	400	30	40	8	50	0.35
	S2_C30_A40_φ8_2					101	0.35
	S2_C30_A40_φ8_3					151	0.35
H_24	S2_C30_A40_φ10_1	400	30	40	10	79	0.10
	S2_C30_A40_φ10_2					79	0.50
	S2_C30_A40_φ10_3					79	0.90
H_25	S2_C45_A80_φ8_1	400	45	80	8	50	0.15
	S2_C45_A80_φ8_2					151	0.15
	S2_C45_A80_φ8_3					251	0.15

(Table follows in next page)

Group	Beam	H (mm)	f_c (MPa)	L_t/ϕ_r	ϕ_s (mm)	A_s (mm ²)	V_f (%)
H_26	S2_C45_A80_φ10_1	400	45	80	10	79	0.10
	S2_C45_A80_φ10_2					79	0.35
	S2_C45_A80_φ10_3					79	0.60
H_27	S2_C45_A60_φ8_1	400	45	60	8	50	0.10
	S2_C45_A60_φ8_2					151	0.10
	S2_C45_A60_φ8_3					251	0.10
H_28	S2_C45_A60_φ10_1	400	45	60	10	79	0.10
	S2_C45_A60_φ10_2					79	0.45
	S2_C45_A60_φ10_3					79	0.80
H_29	S2_C45_A40_φ8_1	400	45	40	8	50	0.10
	S2_C45_A40_φ8_2					151	0.10
	S2_C45_A40_φ8_3					251	0.10
H_30	S2_C45_A40_φ10_1	400	45	40	10	79	0.10
	S2_C45_A40_φ10_2					79	0.60
	S2_C45_A40_φ10_3					79	1.10
H_31	S2_C60_A80_φ8_1	400	60	80	8	50	0.25
	S2_C60_A80_φ8_2					151	0.25
	S2_C60_A80_φ8_3					251	0.25
H_32	S2_C60_A80_φ10_1	400	60	80	10	79	0.10
	S2_C60_A80_φ10_2					79	0.35
	S2_C60_A80_φ10_3					79	0.60
H_33	S2_C60_A60_φ8_1	400	60	60	8	50	0.10
	S2_C60_A60_φ8_2					151	0.10
	S2_C60_A60_φ8_3					251	0.10
H_34	S2_C60_A60_φ10_1	400	60	60	10	79	0.10
	S2_C60_A60_φ10_2					79	0.50
	S2_C60_A60_φ10_3					79	0.90
H_35	S2_C60_A40_φ8_1	400	60	40	8	50	0.10
	S2_C60_A40_φ8_2					151	0.10
	S2_C60_A40_φ8_3					251	0.10
H_36	S2_C60_A40_φ10_1	400	60	40	10	79	0.10
	S2_C60_A40_φ10_2					79	0.75
	S2_C60_A40_φ10_3					79	1.40

The values of M_{cr^*} and M_u , taken from the $M - \bar{w}$ curves of all the 108 ideal HRC beams, are collected in Table 4.2. Such Table also reports the values of DI [computed with Eq.(1.6)], and the reinforcement ratios $r = A_s/A_{s,min} + V_f/V_{f,min}$. In the latter, the values of $A_{s,min}$ and $V_{f,min}$ are those already computed in the previous Sections, which are collected in the same Table 4.2.

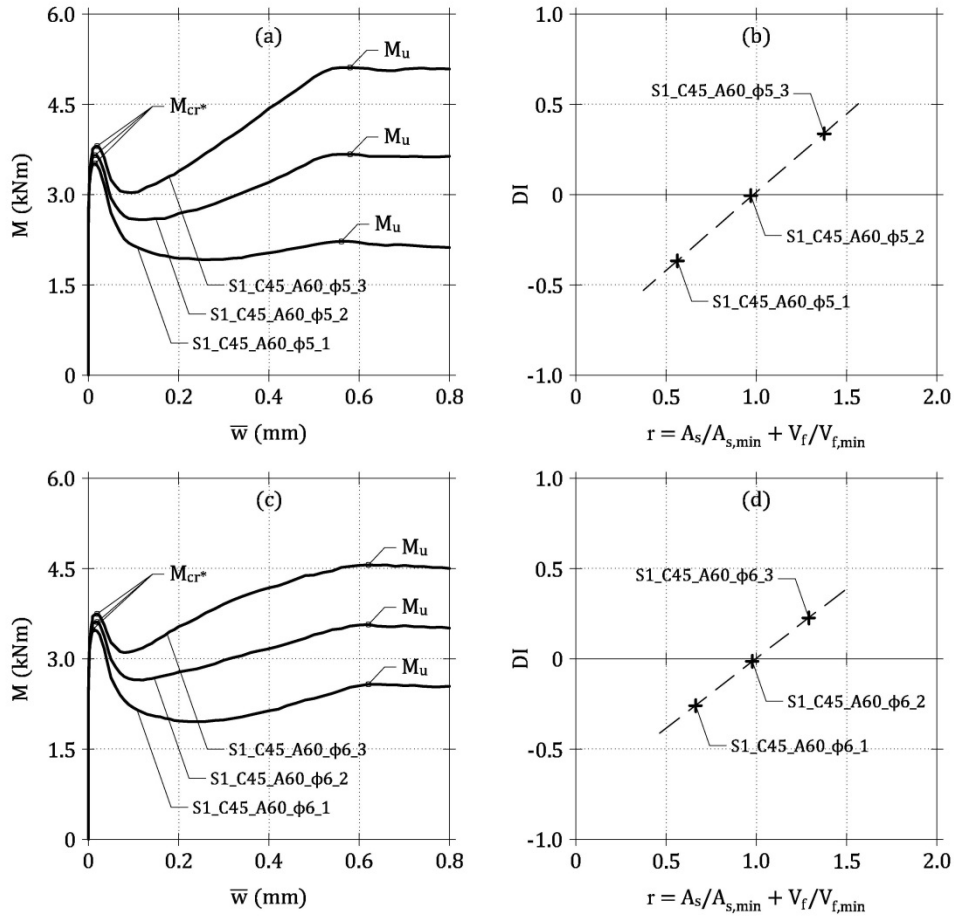


Figure 4.5: Application of the general model: (a) $M - \bar{w}$ curves of the beams of Group H_9; (b) $DI - r$ relationship of Group H_9; (c) $M - \bar{w}$ curves of the beams of Group H_10; (d) $DI - r$ relationship of Group H_10.

Within each group of beams [e.g., those of Group H_9 in Figure 4.5(b) and those of Group H_10 in Figure 4.5(d)], a linear relationship between DI and r is attained and the intersection between the straight line $DI - r$ and the horizontal axis (i.e., $DI = 0$) falls near to $r = 1$. This observation suggests that the ductility condition $DI = 0$ can be attained for different combinations of rebar and fibers (e.g., $A_s \cong 39 \text{ mm}^2$ and $V_f \cong 0.10 \%$ in the case of Group H_9, or $A_s \cong 28 \text{ mm}^2$ and $V_f \cong 0.25 \%$ in the case of Group H_10).

By reporting in a single diagram all the $[DI, r]$ couples computed for the 108 ideal HRC beams (Figure 4.6), it can be observed that almost all the points fall within the envelope described by Eqs.(4.4). Hence, the numerical results of the

proposed model seem to confirm the general validity of the $DI-r$ envelope depicted in Figure 4.6. Also in this general diagram, despite the variability in geometrical size and material properties of the ideal beams (Table 4.1), DI is always zero when the ratio $r \cong 1$. Finally, a unique slope $\zeta = 0.8$ can be obtained by applying a least square approximation to all the $[DI, r]$ numerical points.

Table 4.2: Evaluation of minimum reinforcement in 108 ideal HRC beams.

Group	Beam	M_{cr*} (kNm)	M_u (kNm)	DI	$A_{s,min}$ (mm ²)	$V_{f,min}$ (%)	r
H_1	S1_C30_A80_φ4_1	2.73	2.05	-0.25			0.68
	S1_C30_A80_φ4_2	2.83	2.99	0.06	36	0.44	1.03
	S1_C30_A80_φ4_3	2.95	3.87	0.31			1.38
H_2	S1_C30_A80_φ5_1	2.66	1.96	-0.26			0.65
	S1_C30_A80_φ5_2	2.78	2.78	0.00	37	0.44	0.98
	S1_C30_A80_φ5_3	2.90	3.61	0.24			1.32
H_3	S1_C30_A60_φ4_1	2.76	2.25	-0.19			0.77
	S1_C30_A60_φ4_2	2.89	3.19	0.11	36	0.59	1.11
	S1_C30_A60_φ4_3	3.00	4.12	0.37			1.46
H_4	S1_C30_A60_φ5_1	2.71	2.30	-0.15			0.79
	S1_C30_A60_φ5_2	2.82	2.94	0.04	37	0.59	1.04
	S1_C30_A60_φ5_3	2.93	3.55	0.21			1.29
H_5	S1_C30_A40_φ4_1	2.77	2.04	-0.26			0.68
	S1_C30_A40_φ4_2	2.86	2.98	0.04	36	0.90	1.02
	S1_C30_A40_φ4_3	2.98	3.86	0.29			1.37
H_6	S1_C30_A40_φ5_1	2.66	1.95	-0.27			0.64
	S1_C30_A40_φ5_2	2.81	2.77	-0.02	37	0.90	0.98
	S1_C30_A40_φ5_3	3.00	3.60	0.20			1.31
H_7	S1_C45_A80_φ5_1	3.59	2.77	-0.23			0.72
	S1_C45_A80_φ5_2	3.71	4.19	0.13	48	0.48	1.13
	S1_C45_A80_φ5_3	3.89	5.63	0.45			1.53
H_8	S1_C45_A80_φ6_1	3.56	3.03	-0.15			0.79
	S1_C45_A80_φ6_2	3.64	4.02	0.10	48	0.48	1.11
	S1_C45_A80_φ6_3	3.79	4.98	0.32			1.42
H_9	S1_C45_A60_φ5_1	3.53	2.23	-0.37			0.56
	S1_C45_A60_φ5_2	3.70	3.68	0.00	48	0.64	0.97
	S1_C45_A60_φ5_3	3.83	5.12	0.34			1.38
H_10	S1_C45_A60_φ6_1	3.50	2.59	-0.26			0.66
	S1_C45_A60_φ6_2	3.64	3.59	-0.01	48	0.64	0.98
	S1_C45_A60_φ6_3	3.76	4.60	0.23			1.29

(Table follows in next page)

Group	Beam	M_{cr}^* (kNm)	M_u (kNm)	DI	$A_{s,min}$ (mm ²)	$V_{f,min}$ (%)	r
H_11	S1_C45_A40_φ5_1	3.53	2.23	-0.37			0.56
	S1_C45_A40_φ5_2	3.70	3.68	-0.01	48	0.98	0.97
	S1_C45_A40_φ5_3	3.82	5.12	0.34			1.37
H_12	S1_C45_A40_φ6_1	3.56	2.66	-0.25			0.69
	S1_C45_A40_φ6_2	3.69	3.67	-0.01	48	0.98	0.99
	S1_C45_A40_φ6_3	3.87	4.67	0.21			1.30
H_13	S1_C60_A80_φ5_1	4.30	2.95	-0.31			0.64
	S1_C60_A80_φ5_2	4.45	4.41	-0.01	59	0.48	0.97
	S1_C60_A80_φ5_3	4.60	5.82	0.26			1.31
H_14	S1_C60_A80_φ6_1	4.24	3.17	-0.25			0.69
	S1_C60_A80_φ6_2	4.35	4.34	0.00	59	0.48	1.00
	S1_C60_A80_φ6_3	4.44	5.48	0.23			1.31
H_15	S1_C60_A60_φ5_1	4.31	3.24	-0.25			0.72
	S1_C60_A60_φ5_2	4.46	4.71	0.06	59	0.65	1.05
	S1_C60_A60_φ5_3	4.60	6.10	0.32			1.38
H_16	S1_C60_A60_φ6_1	4.24	2.94	-0.31			0.63
	S1_C60_A60_φ6_2	4.35	4.44	0.02	59	0.65	1.02
	S1_C60_A60_φ6_3	4.52	5.83	0.29			1.41
H_17	S1_C60_A40_φ5_1	4.32	2.96	-0.32			0.64
	S1_C60_A40_φ5_2	4.45	4.40	-0.01	59	0.99	0.97
	S1_C60_A40_φ5_3	4.60	5.80	0.26			1.30
H_18	S1_C60_A40_φ6_1	4.20	2.74	-0.35			0.58
	S1_C60_A40_φ6_2	4.43	4.31	-0.03	59	0.99	0.99
	S1_C60_A40_φ6_3	4.64	5.88	0.27			1.39
H_19	S2_C30_A80_φ8_1	20.21	12.94	-0.36			0.59
	S2_C30_A80_φ8_2	20.79	20.40	-0.02	138	0.44	0.95
	S2_C30_A80_φ8_3	21.53	27.81	0.29			1.32
H_20	S2_C30_A80_φ10_1	20.01	14.81	-0.26			0.69
	S2_C30_A80_φ10_2	20.72	20.78	0.00	137	0.44	1.03
	S2_C30_A80_φ10_3	21.65	26.66	0.23			1.37
H_21	S2_C30_A60_φ8_1	20.40	13.67	-0.33			0.62
	S2_C30_A60_φ8_2	21.11	20.98	-0.01	138	0.59	0.98
	S2_C30_A60_φ8_3	21.66	28.33	0.31			1.34
H_22	S2_C30_A60_φ10_1	19.84	14.31	-0.28			0.66
	S2_C30_A60_φ10_2	20.67	18.73	-0.09	137	0.59	0.91
	S2_C30_A60_φ10_3	21.38	23.06	0.08			1.17
H_23	S2_C30_A40_φ8_1	21.07	16.02	-0.24			0.75
	S2_C30_A40_φ8_2	21.76	23.37	0.07	138	0.90	1.12
	S2_C30_A40_φ8_3	22.25	30.66	0.38			1.48

(Table follows in next page)

Group	Beam	M_{cr^*} (kNm)	M_u (kNm)	DI	$A_{s,min}$ (mm ²)	$V_{f,min}$ (%)	r
H_24	S2_C30_A40_φ10_1	19.98	14.77	-0.26	137	0.90	0.69
	S2_C30_A40_φ10_2	21.58	22.49	0.04			1.13
	S2_C30_A40_φ10_3	23.49	30.45	0.30			1.57
H_25	S2_C45_A80_φ8_1	27.24	16.96	-0.38	187	0.48	0.58
	S2_C45_A80_φ8_2	28.48	31.61	0.11			1.12
	S2_C45_A80_φ8_3	29.79	46.32	0.55			1.66
H_26	S2_C45_A80_φ10_1	26.62	18.23	-0.32	184	0.48	0.64
	S2_C45_A80_φ10_2	28.10	30.77	0.10			1.16
	S2_C45_A80_φ10_3	29.83	43.01	0.44			1.68
H_27	S2_C45_A60_φ8_1	26.70	12.90	-0.52	187	0.64	0.42
	S2_C45_A60_φ8_2	27.95	27.95	0.00			0.96
	S2_C45_A60_φ8_3	29.46	42.65	0.45			1.50
H_28	S2_C45_A60_φ10_1	26.57	16.87	-0.37	184	0.64	0.58
	S2_C45_A60_φ10_2	28.35	30.01	0.06			1.13
	S2_C45_A60_φ10_3	30.25	43.01	0.42			1.68
H_29	S2_C45_A40_φ8_1	26.69	14.68	-0.45	187	0.98	0.37
	S2_C45_A40_φ8_2	27.93	26.47	-0.05			0.91
	S2_C45_A40_φ8_3	29.19	41.37	0.42			1.44
H_30	S2_C45_A40_φ10_1	26.55	15.42	-0.42	184	0.98	0.53
	S2_C45_A40_φ10_2	28.51	28.10	-0.01			1.04
	S2_C45_A40_φ10_3	30.67	40.56	0.32			1.55
H_31	S2_C60_A80_φ8_1	32.73	24.71	-0.25	224	0.49	0.74
	S2_C60_A80_φ8_2	34.24	39.49	0.15			1.19
	S2_C60_A80_φ8_3	35.43	53.65	0.51			1.63
H_32	S2_C60_A80_φ10_1	31.82	19.37	-0.39	221	0.49	0.56
	S2_C60_A80_φ10_2	33.28	34.15	0.03			1.07
	S2_C60_A80_φ10_3	34.87	48.78	0.40			1.59
H_33	S2_C60_A60_φ8_1	32.02	13.77	-0.57	224	0.65	0.38
	S2_C60_A60_φ8_2	33.45	28.80	-0.14			0.83
	S2_C60_A60_φ8_3	34.57	43.44	0.26			1.28
H_34	S2_C60_A60_φ10_1	31.80	17.68	-0.44	221	0.65	0.51
	S2_C60_A60_φ10_2	33.57	35.41	0.06			1.13
	S2_C60_A60_φ10_3	35.68	52.87	0.48			1.75
H_35	S2_C60_A40_φ8_1	31.99	12.19	-0.62	224	0.99	0.32
	S2_C60_A40_φ8_2	33.43	27.28	-0.18			0.77
	S2_C60_A40_φ8_3	34.50	42.10	0.22			1.22
H_36	S2_C60_A40_φ10_1	31.75	17.03	-0.46	221	0.99	0.46
	S2_C60_A40_φ10_2	34.11	35.23	0.03			1.11
	S2_C60_A40_φ10_3	37.14	54.34	0.46			1.76

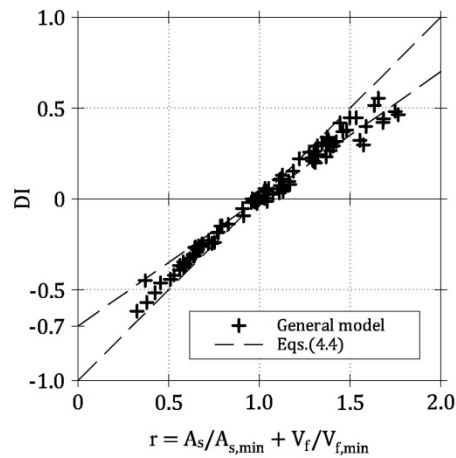


Figure 4.6: Proposed $DI-r$ envelope [Eqs.(4.4)] in comparison with the results of the general model.

4.4 Experimental campaign

To further verify the accuracy of the proposed $DI-r$ envelope [Eqs.(4.4)], an experimental campaign was carried out, in cooperation with CEMEX Research Group AG of Brugg (Switzerland), at the Materials and Structures Experimental Laboratory (MASTRLAB) – Department of Structural, Building and Geotechnical Engineering (DISEG) of Politecnico di Torino (Italy). The study was mainly focused on the flexural behavior of concrete beams reinforced with low amounts of rebar and fibers, separately or in combination. Fresh properties, permeability, and compressive behavior were also evaluated in all the concrete mixtures, and a part of the results is available in Gorino et al. (2016).

4.4.1 Materials

Different combinations of rebar and fibers were adopted to reinforce 30 concrete beams. Specifically, steel rebar having $\phi_s = 6$ mm, $f_y = 527$ MPa, and $f_u = 623$ MPa were employed. Moreover, two types of steel fibers with hooked-ends were used: short fibers SF ($\phi_f = 0.38$ mm, $L_f = 30$ mm, and $f_u = 3,070$ MPa) and long fibers LF ($\phi_f = 0.71$ mm, $L_f = 60$ mm, and $f_u = 2,600$ MPa). The components of six mixtures (i.e., cement CEM I 52.5R, water, sand, gravel, super-plasticizer admixture, and fibers), named with the letters from A to F, are reported in Table 4.3. For both SF and LF, a reference mixture of plain concrete and two FRC mixtures (with $V_f = 0.50$ and 0.75 %) were tailored. The concrete components

were mixed for 180 seconds (i.e., 60 seconds without fibers and 120 seconds after the addition of fibers) by using a planetary mixer with a capacity of 100 liters.

4.4.2 Specimens

With the mixtures described in Table 4.3, 10 series of three un-notched prismatic beams, having a length of 700 mm and a square cross-section of 150×150 mm, were cast (Figure 4.7). The beams, equal to those tested by Falkner and Henke (2005) in four point bending, are labelled by two letters, referred to the concrete mixtures A to F, and to the presence (R), or the absence (P), of a single rebar (having $A_s = 28 \text{ mm}^2$), followed by a number (1, 2, or 3). As shown in Table 4.4, LRC beams were cast with the two mixtures without fibers (i.e., A and D), whereas a series of FRC beams and one of HRC beams were realized for each fiber-reinforced mixture (i.e., B, C, E, and F).

4.4.3 Test set-up

The above-mentioned beams were tested in three point bending by using a MTS testing machine. Two linear supports (with a span of 600 mm) were realized by means of steel cylinders, and a third cylinder was used to apply the load to the beam (Figure 4.7). A load cell of 100 kN measured the applied load, and two transducers determined the midspan deflection on the two sides of the beam (depurated by the support displacements). The bending tests were performed under displacement control, at a velocity of 0.08 mm per minute up to the ultimate load, and then of 0.20 mm per minute.

Table 4.3: Materials contained in 1 m^3 of the concrete mixtures.

Mixture	Cement (kg)	Water (l)	Sand 0-4 (kg)	Gravel 4-8 (kg)	Gravel 8-11 (kg)	Adm. (kg)	SF V_f (%)	LF V_f (%)
A						3.2	0.00	0.00
B						4.0	0.50	0.00
C						4.0	0.75	0.00
D	400	200	864	346	519	3.2	0.00	0.00
E						4.0	0.00	0.50
F						4.0	0.00	0.75

Table 4.4: Amounts of rebar and fibers used to reinforce the tested beams.

Mixture	Beam	A_s (mm ²)	V_f (%)
A	A_R	28	0.00
B	B_P	0	0.50
	B_R	28	
C	C_P	0	0.75
	C_R	28	
D	D_R	28	0.00
E	E_P	0	0.50
	E_R	28	
F	F_P	0	0.75
	F_R	28	

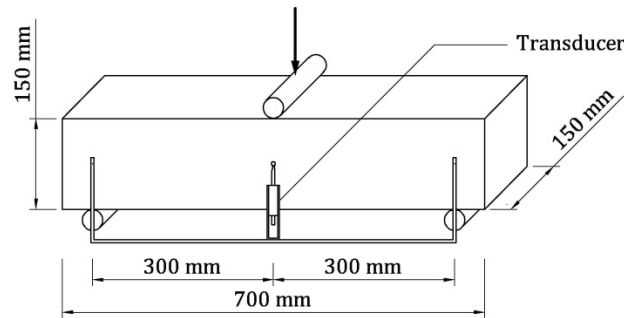
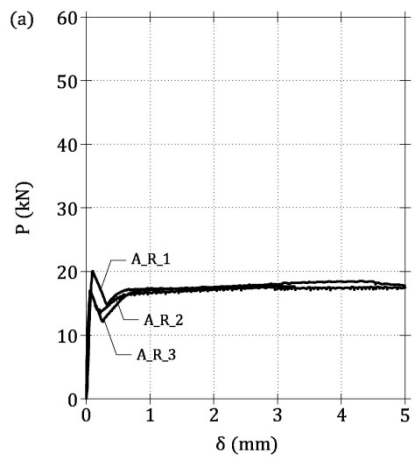


Figure 4.7: Three point bending test on un-notched prismatic specimen.

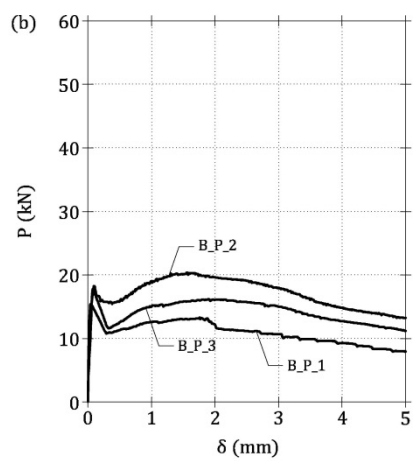
Compression tests were performed on concrete cylinders after 28 days from the casting, and a Galdabini machine (load capacity = 5,000 kN) was employed. The velocity of the stroke was kept constant at 0.60 mm per minute. The compressive strengths of the concrete mixtures are presented in Section 4.5.

4.4.4 Experimental results

The load P vs. midspan deflection δ curves of the concrete beams, and some pictures as well, are illustrated in Figure 4.8, where they are grouped in 10 series of three members with the same concrete mixture and amount of rebar. Figure 4.8(a) represents the experimental curves of the LRC beams cast with mixture A, whereas the curves of the beams containing short fibers (i.e., FRC mixtures B and C), with and without rebar, are shown in Figure 4.8(b-e). Moreover, Figure 4.8(f) reports the P - δ curves of the LRC beams realized with mixture D, and in Figure 4.8(g-j) the responses of the beams containing long fibers (i.e., FRC mixtures E and F), with and without rebar, are shown.

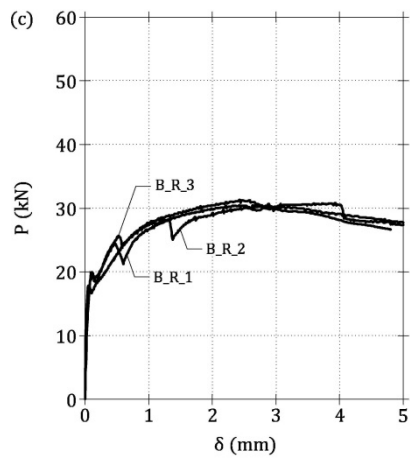


(a) LRC beams series A_R: $A_s = 28 \text{ mm}^2$

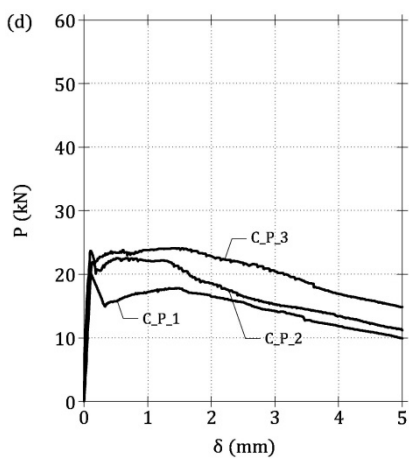


(b) FRC beams series B_P: $V_f = 0.50 \%$ (SF)

(Figure follows in next page)

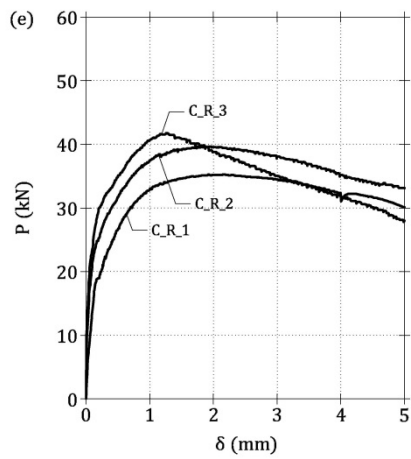


(c) HRC beams series B_R: $A_s = 28 \text{ mm}^2$, $V_f = 0.50 \%$ (SF)

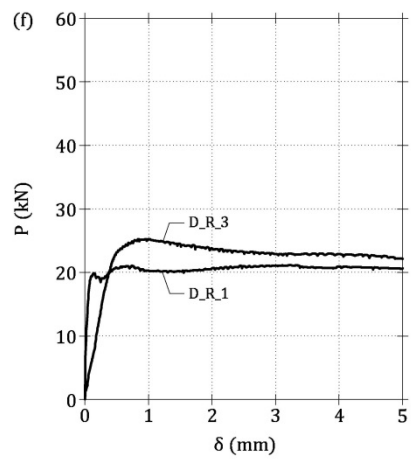


(d) FRC beams series C_P: $V_f = 0.75 \%$ (SF)

(Figure follows in next page)

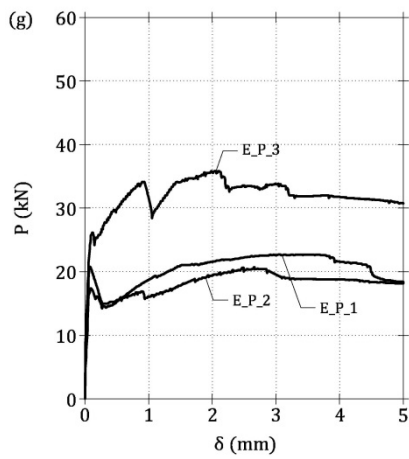


(e) HRC beams series C_R: $A_s = 28 \text{ mm}^2$, $V_f = 0.75 \%$ (SF)

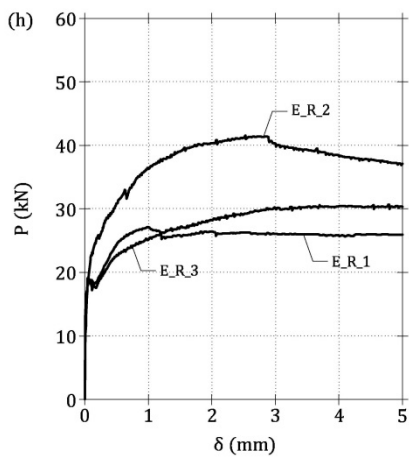


(f) LRC beams series D_R: $A_s = 28 \text{ mm}^2$

(Figure follows in next page)

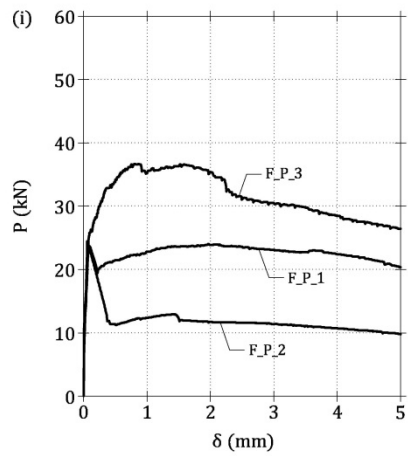


(g) FRC beams series E_P: $V_f = 0.50\%$ (LF)

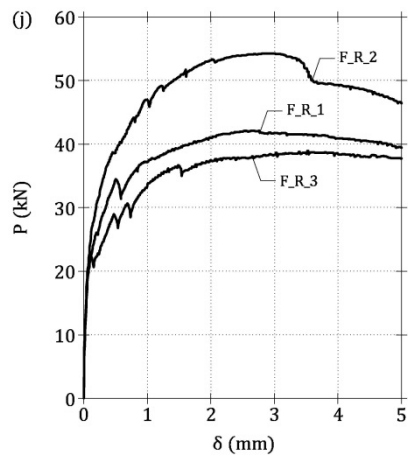


(h) HRC beams series E_R: $A_s = 28 \text{ mm}^2$, $V_f = 0.50\%$ (LF)

(Figure follows in next page)



(i) FRC beams series F_P: $V_f = 0.75\%$ (LF)



(j) HRC beams series F_R: $A_s = 28 \text{ mm}^2$, $V_f = 0.75\%$ (LF)

Figure 4.8: Load vs. deflection curves from three point bending tests.

Concerning the LRC beams A_R and D_R, a ductile response can be observed in the diagrams of Figure 4.8(a,f), as the members maintained the load after the cracking. The same can also be affirmed, in average, for the FRC beams with both short and long fibers B_P, C_P, E_P, and F_P. In these beams, the softening branch after the cracking is followed by an hardening in the $P-\delta$ curves [Figure 4.8(b,d,g,i)]. On the other hand, when a rebar is added to the previous elements, the HRC beams B_R, C_R, E_R, and F_R exhibit a hardening behavior [Figure 4.8(c,e,h,j)].

As the casting of beams was representative of the practical field conditions, a certain dispersion of the experimental results can be noticed in the diagrams of Figure 4.8. This is particularly evident in the cases of FRC beams B_P, C_P, E_P, and F_P, where the random effects of the fiber orientation in the small cross-section of the specimens (Minelli and Plizzari 2011) play an important role on the post-cracking bearing capacity, in the absence of rebar.

4.5 Comparison with the experimental results

In addition to the experimental data reported in the previous Section, some test results available in the literature are also considered. In particular, the bending tests on concrete beams performed by Carpinteri et al. (2015), Dancygier and Berkover (2012), di Prisco et al. (2014), Dupont (2003), Falkner and Henke (2005), and You et al. (2011) are analyzed. With the exception of the three point bending tests by Carpinteri et al. (2015), all the other experimental investigations followed a four point bending protocol. Geometrical and concrete properties of all the beams (reinforced with rebar and/or fibers) are collected in Table 4.5, where the members are indicated with the names originally given by the Authors and divided in 12 homogeneous groups. Moreover, amounts and properties of rebar and fibers are illustrated in the following Table 4.6. The material and the shape of the fibers are described with two letters, as in the previous Table 3.4.

The concrete beams tested in the new experimental campaign presented herein are also described in the same Tables, where they are labelled as Gorino et al. (2016), and regrouped on the basis of the presence of fibers SF (i.e., Group H_I referred to mixtures A, B, and C) or LF (i.e., Group H_II referred to mixtures D, E, and F).

Table 4.5: Geometrical and concrete properties of 54 concrete beams.

Group	Beam	B (mm)	H (mm)	L (mm)	f_c (MPa)	References
H_I	A_R_1	150	150	600	44.93	Gorino et al. (2016)
	A_R_2					
	A_R_3					
	B_P_1				36.33	
	B_P_2					
	B_P_3					
	B_R_1				32.24	
	B_R_2					
	B_R_3					
	C_P_1				40.74	
	C_P_2					
	C_P_3					
	C_R_1				29.20	
	C_R_2					
	C_R_3					
H_II	D_R_1	150	150	600	30.86	Gorino et al. (2016)
	D_R_2					
	D_R_3					
	E_P_1				47.73	
	E_P_2					
	E_P_3					
	E_R_1				45.28	
	E_R_2					
	E_R_3					
	F_P_1				52.16	
	F_P_2					
	F_P_3					
	F_R_1				49.18	
	F_R_2					
	F_R_3					
H_III	0-1 ϕ 8	100	200	1,200	35.88	Carpinteri et al. (2015)
	40-0 ϕ 0				45.90	
	10-1 ϕ 8				50.95	
	20-1 ϕ 8				56.85	
	40-1 ϕ 8				45.90	
H_IV	NF-0-015	240	300	3,200	34.40	Dancygier and Berkover (2012)
	NF-1-015				29.50	

(Table follows in next page)

Group	Beam	B (mm)	H (mm)	L (mm)	f_c (MPa)	References
H_V	Slag Slag R/C	500	125	1,400	43.00	di Prisco et al. (2014)
H_VI	Filler Filler R/C	500	125	1,400	43.00	
H_VII	1+2 13+14	200	200	1,000	$\frac{39.09}{34.28}$	Dupont (2003)
H_VIII	3+4 25	200	200	1,000	$\frac{34.53}{39.43}$	
H_IX	7+8 20	200	200	2,000	$\frac{39.09}{34.28}$	
H_X	9+10 27	200	200	2,000	$\frac{34.53}{39.43}$	
H_XI	RC SFRC RC/SFRC	150	150	600	35.00	Falkner and Henke (2005)
H_XII	A ASF50LD80 ASF40LD65TF4	150	287	910	$\frac{33.80}{30.20}$ 29.60	You et al. (2011)

In some cases, within a single homogeneous group of concrete members, both LRC and FRC beams were tested in addition to one, or more, HRC element. This occurred in the experimental campaigns performed by Carpinteri et al. (2015), Falkner and Henke (2005), and Gorino et al. (2016). In such situations, DI can be computed for all the beams with Eq.(1.6), whereas the values of $A_{s,min}$ and $V_{f,min}$ can be determined for the LRC and FRC beams with Eq.(2.22) and Eq.(3.27), respectively.

However, associated to other HRC beams, data cannot be found for both the LRC and FRC members, but only for one of them. Specifically, reference FRC beams were not tested by Dancygier and Berkover (2012) and You et al. (2011). On the other hand, in the experimental campaigns performed by di Prisco et al. (2014) and Dupont (2003), data on the reference LRC beams were not reported. In all these cases, the load P_u of the missing beam is evaluated by means of the superposition of the effects due to rebar and fibers at ultimate limit state (Falkner and Henke 2005), knowing the ultimate load of the HRC beam. Moreover, P_{cr*} is assumed to be the average of the values measured for the beams of the same group.

Table 4.6: Rebar and fibers used in 54 concrete beams.

Group	Beam	f_y (MPa)	A_s (mm ²)	Fibers	L_f/ϕ_f	V_f (%)	References
H_I	A_R_1	527	28	/	/	0.00	Gorino et al. (2016)
	A_R_2						
	A_R_3						
	B_P_1	/	0			0.50	
	B_P_2						
	B_P_3						
	B_R_1	527	28	H_S	79		
	B_R_2						
	B_R_3						
	C_P_1	/	0			0.75	
	C_P_2						
	C_P_3						
	C_R_1	527	28				
	C_R_2						
	C_R_3						
H_XII	D_R_1	527	28	/	/	0.00	
	D_R_2						
	D_R_3						
	E_P_1	/	0			0.50	
	E_P_2						
	E_P_3						
	E_R_1	527	28	H_S	85		
	E_R_2						
	E_R_3						
	F_P_1	/	0			0.75	
	F_P_2						
	F_P_3						
	F_R_1	527	28				
	F_R_2						
	F_R_3						
H_III	0-1 ϕ 8	484	50	/	/	0.00	Carpinteri et al. (2015)
	40-0 ϕ 0	/	0			0.51	
	10-1 ϕ 8					0.13	
	20-1 ϕ 8	484	50	H_S	81	0.25	
	40-1 ϕ 8					0.51	
H_IV	NF-0-015	496	101	/	/	0.00	Dancygier and Berkover (2012)
	NF-1-015			H_S	64	0.75	

(Table follows in next page)

Group	Beam	f_y (MPa)	A_s (mm ²)	Fibers	L_f/ϕ_f	V_f (%)	References																																																																																			
H_V	Slag	/	0	S_P	50	1.20	di Prisco et al. (2014)																																																																																			
	Slag R/C	559	113					H_VI	Filler	/	0	S_P	50	1.20	Filler R/C	559	113	H_VII	1+2	/	0	H_S	67	0.32	13+14	560	101	H_VIII	3+4	/	0	H_S	67	0.64	Dupont (2003)	25	560	101	H_IX	7+8	/	0	H_S	67	0.32	20	560	101	H_X	9+10	/	0	H_S	67	0.64	27	560	101	H_XI	RC	500	28	/	/	0.00	Falkner and Henke (2005)	SFRC	/	0	H_S	80	0.51	RC/SFRC	500	28	H_XII	A	459	101	/	/	0.00	You et al. (2011)	ASF50LD80	H_S	80	0.64	ASF40LD65TF4	H_S	64
H_VI	Filler	/	0	S_P	50	1.20																																																																																				
	Filler R/C	559	113					H_VII	1+2	/	0	H_S	67	0.32	13+14	560	101	H_VIII	3+4	/	0	H_S	67	0.64	Dupont (2003)	25	560	101	H_IX	7+8	/	0	H_S	67		0.32	20	560	101	H_X	9+10	/	0	H_S	67	0.64	27	560	101	H_XI	RC	500	28	/	/	0.00	Falkner and Henke (2005)	SFRC		/	0	H_S	80	0.51	RC/SFRC		500	28	H_XII	A	459	101	/	/	0.00		You et al. (2011)			ASF50LD80	H_S	80		0.64	ASF40LD65TF4	H_S	64	0.82	S_P	45
H_VII	1+2	/	0	H_S	67	0.32																																																																																				
	13+14	560	101					H_VIII	3+4	/	0	H_S	67	0.64	Dupont (2003)	25	560	101	H_IX	7+8	/	0	H_S	67		0.32	20	560	101	H_X	9+10	/	0	H_S		67	0.64	27	560	101	H_XI	RC	500	28	/	/	0.00	Falkner and Henke (2005)	SFRC		/	0	H_S	80	0.51	RC/SFRC		500	28	H_XII	A	459	101	/	/	0.00	You et al. (2011)	ASF50LD80		H_S			80	0.64	ASF40LD65TF4	H_S		64	0.82	S_P	45									
H_VIII	3+4	/	0	H_S	67	0.64	Dupont (2003)																																																																																			
	25	560	101					H_IX	7+8	/	0	H_S	67	0.32		20	560	101	H_X	9+10	/	0	H_S	67		0.64	27	560	101	H_XI	RC	500	28	/	/	0.00	Falkner and Henke (2005)	SFRC	/	0		H_S	80	0.51	RC/SFRC	500	28		H_XII	A	459	101	/	/	0.00	You et al. (2011)	ASF50LD80	H_S	80		0.64			ASF40LD65TF4	H_S	64		0.82	S_P	45																				
H_IX	7+8	/	0	H_S	67	0.32																																																																																				
	20	560	101					H_X	9+10	/	0	H_S	67	0.64		27	560	101	H_XI	RC	500	28	/	/	0.00	Falkner and Henke (2005)	SFRC	/	0		H_S	80	0.51	RC/SFRC	500	28		H_XII	A	459	101	/	/	0.00	You et al. (2011)	ASF50LD80	H_S	80		0.64			ASF40LD65TF4	H_S	64		0.82	S_P	45																															
H_X	9+10	/	0	H_S	67	0.64																																																																																				
	27	560	101					H_XI	RC	500	28	/	/	0.00	Falkner and Henke (2005)	SFRC	/	0		H_S	80	0.51	RC/SFRC	500	28		H_XII	A	459	101	/	/	0.00	You et al. (2011)	ASF50LD80	H_S	80		0.64			ASF40LD65TF4	H_S	64		0.82	S_P	45																																										
H_XI	RC	500	28	/	/	0.00	Falkner and Henke (2005)																																																																																			
	SFRC	/	0	H_S	80	0.51																																																																																				
	RC/SFRC	500	28					H_XII	A	459	101	/	/	0.00	You et al. (2011)	ASF50LD80	H_S	80	0.64	ASF40LD65TF4	H_S	64	0.82	S_P	45																																																																	
H_XII	A	459	101	/	/	0.00	You et al. (2011)																																																																																			
	ASF50LD80			H_S	80	0.64																																																																																				
	ASF40LD65TF4			H_S	64	0.82																																																																																				
				S_P	45																																																																																					

Hence, for each member, it is possible to calculate DI by using Eq.(1.6), whereas, $A_{s,min}$ and $V_{f,min}$ for LRC and FRC beams are determined with Eq.(2.22) and Eq.(3.27), respectively. For the sake of simplicity, a unique value of the coefficient $\zeta = 0.8$ is used in both Eq.(2.22) and Eq.(3.27) for determining $A_{s,min}$ and $V_{f,min}$, respectively. Therefore, the evaluation of r for all the members of each group, including HRC beams, is in turn possible. The values of DI for all the 54 beams analyzed herein are reported in Table 4.7, whereas the values of r are collected in Table 4.8.

The experimental values of DI obtained from the 25 HRC beams are plotted, as a function of r , in the diagram depicted in Figure 4.9, and put in comparison with the envelope defined by Eqs.(4.4). The data related to the other 29 LRC and FRC members are not reported in the same non-dimensional diagram, because they would not be significant. In fact, all the values of $A_{s,min}$ and $V_{f,min}$ used to compute the ratios r are derived from their DI , assuming a linear relationship. Therefore, the [$DI-r$] points of LRC and FRC members would obviously follow a straight line having a slope $\zeta = 0.8$. In other words, differently from the points referred to the HRC beams, they would not prove the effectiveness of the proposed envelope.

Table 4.7: Evaluation of the ductility index in 54 concrete beams.

Group	Beam	P_{cr}^* (kN)	P_u (kN)	DI	References
H_I	A_R_1	20.09	17.70	-0.12	Gorino et al. (2016)
	A_R_2	16.52	17.71	0.07	
	A_R_3	17.02	18.51	0.09	
	B_P_1	15.44	13.27	-0.14	
	B_P_2	18.26	20.39	0.12	
	B_P_3	17.84	16.17	-0.09	
	B_R_1	17.84	30.44	0.71	
	B_R_2	19.44	30.79	0.58	
	B_R_3	19.92	31.31	0.57	
	C_P_1	20.06	17.82	-0.11	
	C_P_2	21.90	22.58	0.03	
	C_P_3	23.67	24.10	0.02	
	C_R_1	18.78	35.24	0.88	
	C_R_2	17.91	39.65	1.21	
	C_R_3	22.72	41.76	0.84	
H_II	D_R_1	19.84	21.14	0.07	Carpinteri et al. (2015)
	D_R_2		MISSING		
	D_R_3	25.26	22.99	-0.09	
	E_P_1	17.37	22.70	0.31	
	E_P_2	20.79	20.72	0.00	
	E_P_3	26.17	35.83	0.37	
	E_R_1	18.82	27.17	0.44	
	E_R_2	18.86	41.55	1.20	
	E_R_3	19.08	30.69	0.61	
	F_P_1	23.69	24.01	0.01	
	F_P_2	24.47	12.93	-0.47	
	F_P_3	26.31	36.70	0.39	
	F_R_1	26.11	42.13	0.61	
	F_R_2	26.45	54.27	1.05	
	F_R_3	22.63	38.94	0.72	
H_III	0-1 ϕ 8	16.31	19.33	0.19	Dancygier and Berkover (2012)
	40-0 ϕ 0	16.05	15.47	-0.04	
	10-1 ϕ 8	16.70	21.48	0.29	
	20-1 ϕ 8	16.64	25.52	0.53	
	40-1 ϕ 8	14.35	27.22	0.90	
H_IV	NF-0-015	17.25	38.24	1.22	Dancygier and Berkover (2012)
	NF-1-015	17.25	43.24	1.51	

(Table follows in next page)

Group	Beam	P_{cr}^* (kN)	P_u (kN)	DI	References
H_V	Slag	31.12	13.93	-0.55	di Prisco et al. (2014)
	Slag R/C	35.39	48.88	0.38	
H_VI	Filler	32.64	11.93	-0.63	
	Filler R/C	31.07	46.88	0.51	
H_VII	1+2	27.22	21.62	-0.21	Dupont (2003)
	13+14	26.55	68.50	1.58	
H_VIII	3+4	27.56	27.22	-0.01	
	25	32.51	77.60	1.39	
H_IX	7+8	10.32	5.77	-0.44	Falkner and Henke (2005)
	20	11.33	26.56	1.34	
H_X	9+10	14.84	16.90	0.14	
	27	16.40	33.74	1.06	
H_XI	RC	3.77	4.32	0.15	Falkner and Henke (2005)
	SFRC	3.77	2.51	-0.33	
	RC/SFRC	3.77	5.72	0.52	
H_XII	A	54.09	100.90	0.87	You et al. (2011)
	ASF50LD80	57.40	127.17	1.22	
	ASF40LD65TF4	58.76	145.27	1.47	

As shown by Figure 4.9, the proposed envelope [i.e., Eqs.(4.4)] incorporates about all the experimental points, despite the high scatter in the test results described in Section 4.4 (Figure 4.8).

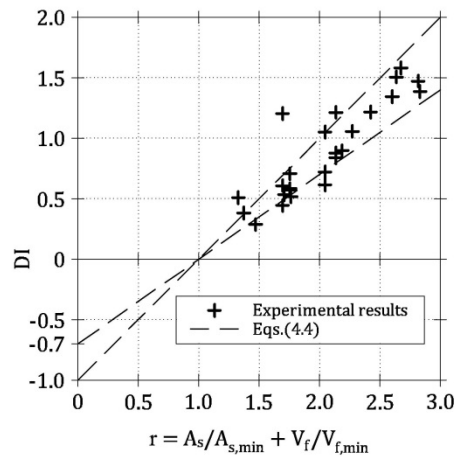


Figure 4.9: Proposed $DI-r$ envelope [Eqs.(4.4)] in comparison with the results of some experimental campaigns.

Since the effective cracking load is experimentally confirmed to remain almost constant with the amount of reinforcement (Table 4.7), an approximately linear increment of P_u with r can be recognized in Figure 4.9. Moreover, the brittle/ductile transition [i.e., the condition $DI = 0$ in Eq.(1.6)] can be observed when $r \cong 1$, confirming the general validity of the proposed approach, and the assumption $\zeta = 0.8$ for both LRC and FRC beams as well.

Table 4.8: Evaluation of the minimum reinforcement in 54 concrete beams.

Group	Beam	$A_{s,min}$ (mm ²)	$V_{f,min}$ (%)	r	References
H_I	A_R_1	29	0.66	0.99	Gorino et al. (2016)
	A_R_2				
	A_R_3				
	B_P_1			0.76	
	B_P_2				
	B_P_3				
	B_R_1			1.75	
	B_R_2				
	B_R_3				
	C_P_1			1.14	
	C_P_2				
	C_P_3				
	C_R_1			2.13	
	C_R_2				
	C_R_3				
H_II	D_R_1	29	0.71	0.99	Gorino et al. (2016)
	D_R_2				
	D_R_3				
	E_P_1			0.70	
	E_P_2				
	E_P_3				
	E_R_1			1.69	
	E_R_2				
	E_R_3				
	F_P_1			1.05	
	F_P_2				
	F_P_3				
	F_R_1			2.04	
	F_R_2				
	F_R_3				

(Table follows in next page)

Group	Beam	$A_{s,min}$ (mm^2)	$V_{f,min}$ (%)	r	References
H_III	0-1 ϕ 8	41	0.53	1.23	Carpinteri et al. (2015)
	40-0 ϕ 0			0.96	
	10-1 ϕ 8			1.47	
	20-1 ϕ 8			1.71	
	40-1 ϕ 8			2.19	
H_IV	NF-0-015	40	6.66	2.52	Dancygier and Berkover (2012)
	NF-1-015			2.63	
H_V	Slag	106	3.88	0.31	di Prisco et al. (2014)
	Slag R/C			1.37	
H_VI	Filler	101	5.80	0.21	
	Filler R/C			1.33	
H_VII	1+2	52	0.43	0.74	
	13+14			2.67	
H_VIII	3+4	54	0.65	0.98	Dupont (2003)
	25			2.83	
H_IX	7+8	47	0.71	0.45	
	20			2.60	
H_X	9+10	92	0.54	1.17	
	27			2.27	
H_XI	RC	24	0.88	1.18	Falkner and Henke (2005)
	SFRC			0.58	
	RC/SFRC			1.76	
H_XII	A	48	/	2.08	You et al. (2011)
	ASF50LD80			2.42	
	ASF40LD65TF4			2.81	

4.6 Discussion of the results

Both the 108 numerically evaluated points of Figure 4.6, and the 25 experimental points of Figure 4.9, corroborate the consistency of the proposed $DI-r$ envelope [Eqs.(4.4)]. To be more precise, this envelope appears generally valid, regardless of geometrical size and material properties of the beams. As a matter of fact, it is based on the adoption of the normalized variables DI and r . Referring to the reinforcement ratio, in particular, the general definition $r = A_s/A_{s,min} + V_f/V_{f,min}$ puts into evidence the possible equivalence between rebar and fibers (i.e., between $A_{s,min}$ and $V_{f,min}$), whereas the influence of size and materials disappears. However, it must be remarked that such influence is included in the terms $A_{s,min}$ and $V_{f,min}$, which are defined for the specific type of beam, with the related concrete strength, rebar and fiber properties, geometrical size, etc. (Gorino et al. 2016). In such a way, the ratio r appears as a non-dimensional reinforcement parameter, normalized with respect to any geometrical and mechanical property. It

is equal to 1 for LRC beams ($V_f = 0$) reinforced with an area of rebar $A_s = A_{s,\min}$, as well as for FRC beams ($A_s = 0$) containing a quantity of fibers $V_f = V_{f,\min}$.

As the numerical results reported in Figure 4.6 and the experimental values of Figure 4.9 are in good agreement with the proposed $DI-r$ envelope, it can be affirmed that the proposed general model can be correctly used to assess the brittle/ductile behavior of HRC beams. Indeed, all the simplified hypotheses adopted in the model (e.g., the fiber symmetrically and orthogonally positioned with respect to the crack in the ideal tie, the cohesive and bond-slip models, the crack with a linear profile in HRC beam, the elastic-plastic constitutive law of steel rebar, the constant bending moment within l_{tr} , etc.) seem to be almost irrelevant with respect to the $DI-r$ relationships.

Additionally, both Figure 4.6 and Figure 4.9 put into evidence the multiple ways to reinforce an HRC beam in order to satisfy the minimum required ductility $P_u = P_{cr^*}$. In particular, it is sufficient to impose $r = 1$ [i.e., $DI = 0$ in Eq.(1.6)] through any linear combination of $A_{s,\min}$ and $V_{f,\min}$, as illustrated in Figure 4.10 (Gorino et al. 2016):

$$\frac{A_s}{A_{s,\min}} + \frac{V_f}{V_{f,\min}} = 1 \quad (4.5)$$

Hence, by combining rebar and fibers, it is possible to reduce the minimum amount of reinforcement $A_{s,\min}$ traditionally required by building codes for LRC beams (ACI 2014, CEN 2004a, *fib* 2012a). This is in accordance with the results of some previous theoretical models (Chiaia et al. 2007, Mobasher et al. 2015) and with the recent recommendations of Model Code 2010 (*fib* 2012a).

The proposed Eq.(4.5) presents a strong analogy with the formulation introduced by Liao et al. (2016) for the problem of the minimum reinforcement in HRC beams. However, $A_{s,\min}$ and $V_{f,\min}$ are herein evaluated with few bending tests on LRC and FRC full-scale members rather than on small beam specimens as performed by Liao et al. (2016). In this way, the present approach is not affected by the size effect (Carpinteri and Cornetti 2002), which could appear when, from the small laboratory scale, one should pass to the real scale of a structural element.

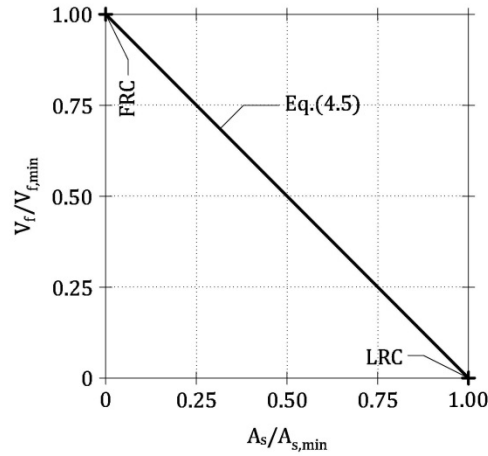


Figure 4.10: Eq.(4.5) for combining rebar and fibers in order to attain the condition of minimum ductility (i.e., $DI = 0$).

Finally, Eq.(4.5) could be usefully applied as a tool for designing the beams of reinforced concrete structures, when seismic actions have to be taken into account. In such situation, to avoid the brittle failure of beams, Eurocode 8 (CEN 2004b) requires a specific minimum area of rebar in tension, which is given by a formula formally equal to the previous Eq.(1.2) for static actions (ACI 2014, CEN 2004a, *fib* 2012a):

$$A_{s,min} = \vartheta \cdot \frac{f_{ct}}{f_y} \cdot B \cdot d \quad (4.6)$$

where ϑ = coefficient greater than ω in Eq.(1.2); f_{ct} = tensile strength of concrete; f_y = yielding strength of steel rebar; B and d = width and effective depth, respectively, of a beam cross-section.

Nevertheless, if a suitable volume of fibers is added to the concrete, the value given by Eq.(4.6) can be reduced in proportion to the ratio $V_f/V_{f,min}$ [i.e., according to Eq.(4.5)]. To be more precise, when Eurocode 8 (CEN 2004b) must be applied, $A_{s,min}$ is given by Eq.(4.6), and $V_{f,min}$ can be obtained with a full-scale bending test performed on FRC beams. Thus, if an amount of fibers $V_f < V_{f,min}$ is assumed, the area of rebar $A_s < A_{s,min}$ can be obtained by combining Eq.(4.5) with Eq.(4.6), and provided in the concrete element:

$$A_s = \vartheta \cdot \frac{f_{ct}}{f_y} \cdot B \cdot d \cdot \left(1 - \frac{V_f}{V_{f,min}} \right) \quad (4.7)$$

As a result, Eq.(4.7) can be used to substitute Eq.(4.6) (CEN 2004b) in the design of reinforced concrete structures under seismic actions, containing an amount of fibers V_f .

Chapter 5

A new and unified approach for concrete beams

5.1 General envelope for concrete beams

Based on the general definition of the normalized reinforcement ratio given in Chapter 4 (i.e., $r = A_s/A_{s,min} + V_f/V_{f,min}$), a unified approach for the brittle/ductile assessment of concrete beams, reinforced with rebar, fibers, or a combination, is proposed herein. Even if such definition is generally referred to an HRC beam, reinforced with an area of rebar A_s and a fiber volume fraction V_f , it is equally valid in the cases of LRC and FRC elements (i.e., when $V_f = 0$, and when $A_s = 0$, respectively). In other words, the reinforcement ratios separately introduced in the previous Chapters, can be considered as a unique non-dimensional variable defining the quantity of rebar and/or fibers present in a concrete member. Accordingly, all the relationships describing the variation of the ductility index DI as a function of the reinforcement ratio r previously introduced for LRC, FRC, and HRC beams in bending can be superposed in the same $DI-r$ diagram of Figure 5.1. In this diagram, for positive values of the ductility index, Eq.(2.4) for LRC members appears as the upper bound of the $DI-r$ envelope valid for HRC beams [Eqs.(4.4)], whereas when $DI < 0$ the upper bound of the envelope is given by Eq.(3.4) for FRC elements. This can be summarized by the following formulae:

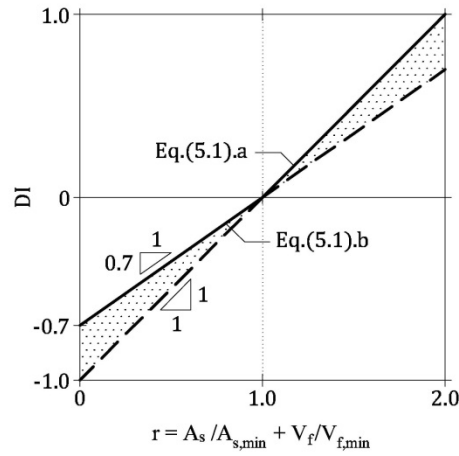


Figure 5.1: $DI-r$ envelope for concrete beams.

$$DI = r - 1 \quad 0 \leq DI \quad (5.1).a$$

$$DI = 0.7 \cdot (r - 1) \quad DI \leq 0 \quad (5.1).b$$

To verify this upper bound functions, the numerical results previously illustrated in Figure 2.10, Figure 3.11, and Figure 4.6 (and reported in Table 2.2, Table 3.2, and Table 4.2) are collected in a unique $DI-r$ diagram (Figure 5.2). Moreover, all the $[DI-r]$ points of Figure 2.12, Figure 3.13, and Figure 4.9 (collected in Table 2.4, Table 3.5, and Tables 4.7-8), obtained from the results of experimental campaigns, are superposed in the general diagram of Figure 5.3.

As it can be observed in the two Figures, all the numerical results (Figure 5.2), and about all the experimental points (Figure 5.3), fall under the previous upper bound. In addition, despite a certain inevitable scatter, the 198 numerical $[DI-r]$ couples of Figure 5.2, and the 136 experimental points reported in Figure 5.3 as well, appear for the most part enveloped by Eqs.(4.4).

This is particularly true when $DI \cong 0$ in Figure 5.2 and in Figure 5.3, as the simplified models adopted in Sections 2.1, 3.1, and 4.1 are more accurate when $A_s \rightarrow A_{s,min}$, $V_f \rightarrow V_{f,min}$, and $A_s/A_{s,min} + V_f/V_{f,min} \rightarrow 1$, respectively. If a least square approximation is separately applied to the numerical points of Figure 5.2, and to the experimental data of Figure 5.3, a linear relationship having the slope $\zeta = 0.8$ is obtained in both the cases:

$$DI = 0.8 \cdot (r - 1) \quad (5.2)$$

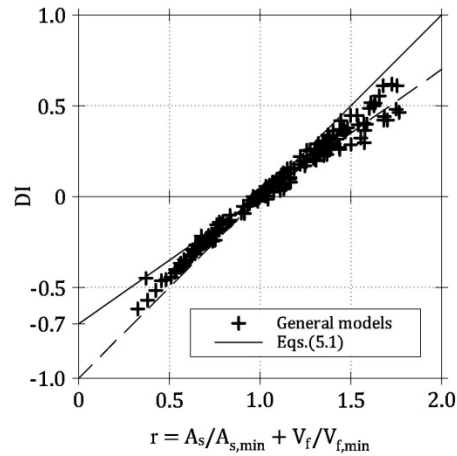


Figure 5.2: Comparison between the proposed $DI-r$ envelope for concrete members and the numerical results referred to 198 LRC, FRC, and HRC beams (Table 2.2, Table 3.2, and Table 4.2, respectively).

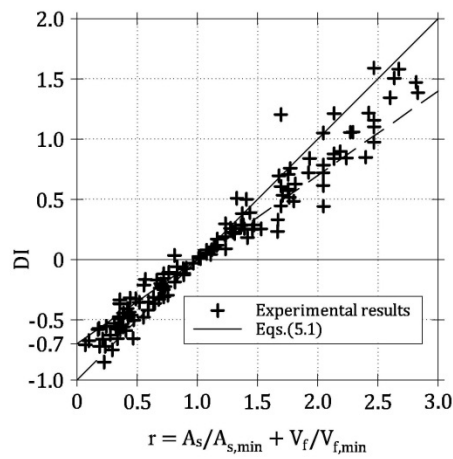


Figure 5.3: Comparison between the proposed $DI-r$ envelope for concrete members and the experimental results referred to 136 LRC, FRC, and HRC beams (Table 2.4, Table 3.5, and Tables 4.7-8, respectively).

5.2 Three-dimensional interpretation of the proposed approach

Since the ductility index of a concrete beam, in the general case, is a function of both $A_s/A_{s,min}$ and $V_f/V_{f,min}$ [Eq.(5.2)], the natural domain where the variation of DI should be studied is a three-dimensional space. However, the three coordinates which define the position of a point that belongs to this space are the non-dimensional variables DI , $A_s/A_{s,min}$, and $V_f/V_{f,min}$. The partial reinforcement ratios $A_s/A_{s,min}$ and $V_f/V_{f,min}$ are defined positive, whereas DI can assume both positive and negative values, for ductile and brittle responses, respectively.

If the ratio $r = A_s/A_{s,min} + V_f/V_{f,min}$ is substituted into Eq.(5.2), the existence of an inclined plane in the $DI - A_s/A_{s,min} - V_f/V_{f,min}$ space can be argued (Figure 5.4):

$$DI = 0.8 \cdot \left(\frac{A_s}{A_{s,min}} + \frac{V_f}{V_{f,min}} - 1 \right) \quad (5.3)$$

Obviously, Eq.(5.3) define a plane only if a unique slope $\zeta = 0.8$ can be assumed for all the LRC, FRC, and HRC beams in bending. Nevertheless, by accepting this approximation, the planar surface depicted in Figure 5.4 describes the variation of DI when the area of rebar and the fiber volume fraction of a concrete beam are differently combined. The interception of such surface with the horizontal plane $DI = 0$ (i.e., the brittle/ductile transition) is the straight line described by Eq.(4.5) and previously represented in Figure 4.10.

To show the effectiveness of the present three-dimensional interpretation, all the numerical $[DI - r]$ couples of Figure 5.2 (also collected in Table 2.2, Table 3.2, and Table 4.2) are reported in the $DI - A_s/A_{s,min} - V_f/V_{f,min}$ space and put in comparison with the function of Eq.(5.3). For the sake of simplicity, Figure 5.5 projects the proposed plane along the bisecting surface $A_s/A_{s,min} = V_f/V_{f,min}$. In addition, all the experimental points of Figure 5.3 (also collected in Table 2.4, Table 3.5, and Tables 4.7-8), are projected on the bisecting plane referred to the $DI - A_s/A_{s,min} - V_f/V_{f,min}$ space, to be compared with the planar surface of Eq.(5.3) (Figure 5.6).

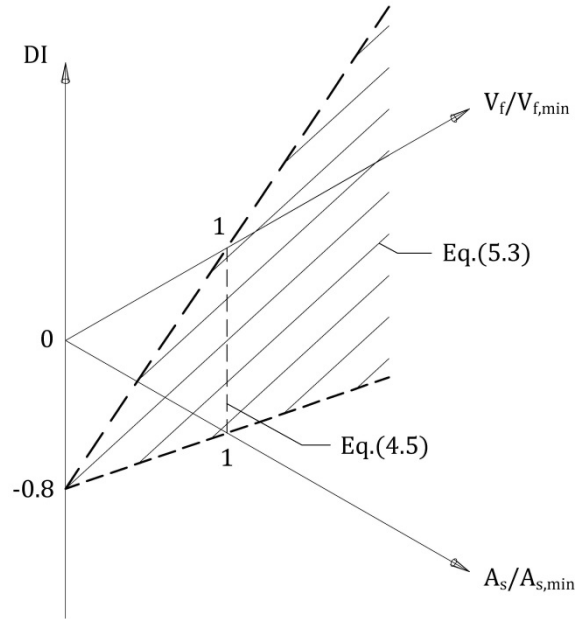


Figure 5.4: Proposed plane in the $DI - A_s/A_{s,min} - V_f/V_{f,min}$ space [Eq.(5.3)].

As it can be observed in Figure 5.5, the function defined by Eq.(5.3) actually approximate the distribution of the ductility indexes referred to all the 198 ideal concrete beams analyzed in Chapters 2, 3, and 4, and reinforced with different combinations of rebar and/or fibers. Moreover, despite the experimental scatter already observed in Figure 2.12, Figure 3.13, and Figure 4.9, the proposed plane also provides an acceptable approximation of the 136 test results collected in Figure 5.6.

With reference to the numerical results of Figure 5.5, and to the experimental data of Figure 5.6 as well, a least square approximation can be applied on the three non-dimensional variables DI , $A_s/A_{s,min}$, and $V_f/V_{f,min}$. Such operation provides the equation of the plane which better approximates the $[DI - r]$ points, i.e., two coefficients referred to the variables $A_s/A_{s,min}$ and $V_f/V_{f,min}$, and the limit value of DI for $A_s/A_{s,min} = V_f/V_{f,min} = 0$. As a result, in both the cases, the two coefficients of $A_s/A_{s,min}$ and $V_f/V_{f,min}$ are equal to 0.8, whereas the intercept of the plane with the vertical axis is -0.8. This means that the plane described by Eq.(5.3) is the better approximation of both the numerical and experimental results referred to all the 334 ideal and real concrete beams taken into account herein.

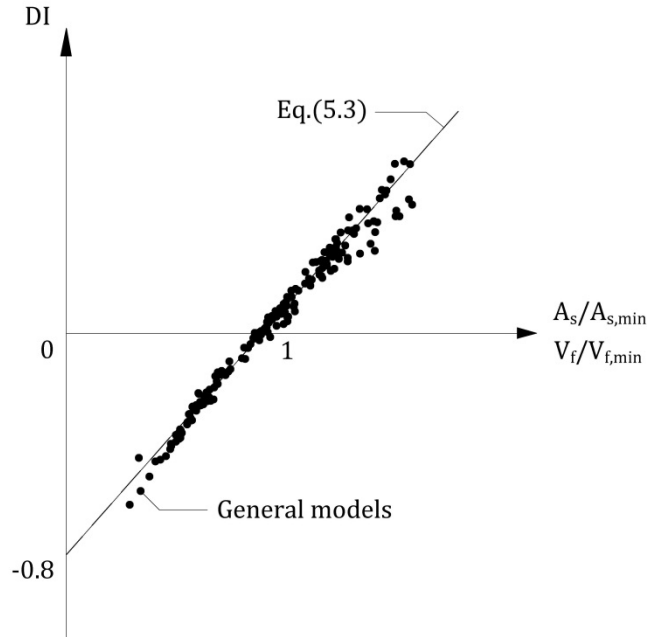


Figure 5.5: Projection of the proposed plane [i.e., Eq.(5.3)] along the bisecting surface of the $DI-A_s/A_{s,min}-V_f/V_{f,min}$ space [i.e., $A_s/A_{s,min} = V_f/V_{f,min}$], in comparison with the numerical results referred to 198 LRC, FRC, and HRC beams (Table 2.2, Table 3.2, and Table 4.2, respectively).

Such finding confirms that a unique value $\zeta = 0.8$ can be assumed, as a first approximation, for describing the linear variation of the ductility index DI with respect to the reinforcement ratio r , in the general case. In other words, the two interceptions of the plane described by Eq.(5.3) with the surfaces $V_f/V_{f,min} = 0$ and $A_s/A_{s,min} = 0$ (Figure 5.4) can be used as $DI-r$ linear relationships for LRC and FRC beams, respectively.

The three-dimensional function of Eq.(5.3) should be considered as the tangent plane of a more complex surface of the $DI-A_s/A_{s,min}-V_f/V_{f,min}$ space, for $r = 1$. As a matter of fact, the proposed plane well approximates the real surface especially when $DI \cong 0$ (Figure 5.5 and Figure 5.6). This because the plane described by Eq.(5.3) is the spatial extension of the two-dimensional $DI-r$ linear relationships previously determined for LRC and FRC beams [i.e., Eq.(2.4) in Chapter 2 and Eq.(3.4) in Chapter 3], which are especially valid for $A_s \rightarrow A_{s,min}$ and for $V_f \rightarrow V_{f,min}$, respectively.

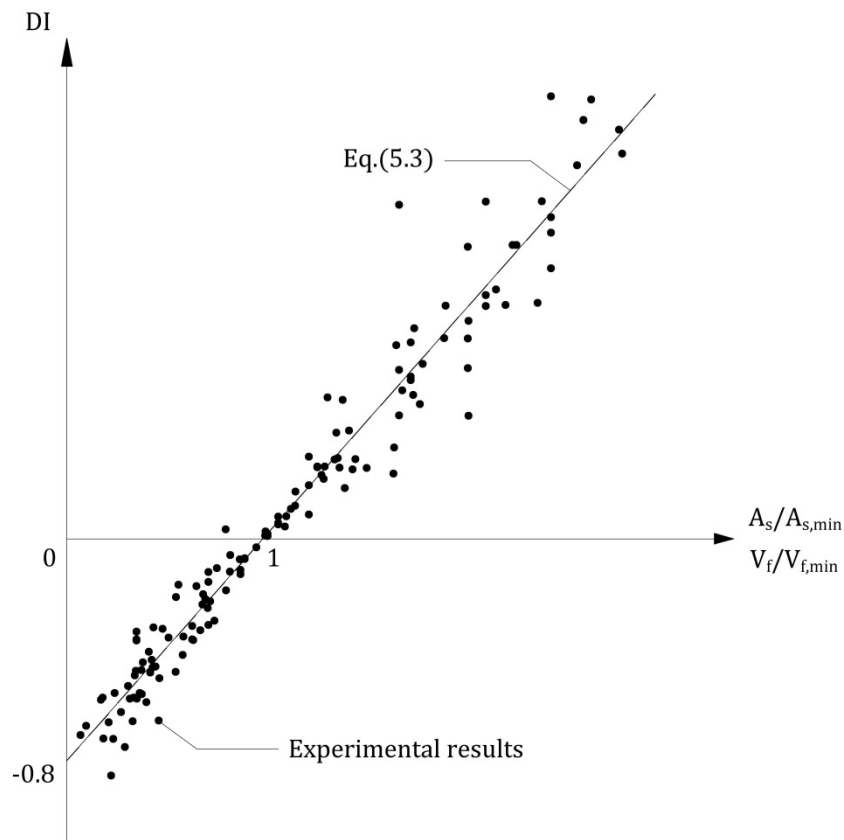


Figure 5.6: Projection of the proposed plane [i.e., Eq.(5.3)] along the bisecting surface of the $DI - A_s/A_{s,min} - V_f/V_{f,min}$ space [i.e., $A_s/A_{s,min} = V_f/V_{f,min}$], in comparison with the experimental results referred to 136 LRC, FRC, and HRC beams (Table 2.4, Table 3.5, and Tables 4.7-8, respectively).

5.3 Practical application of the proposed approach

From a practical point of view, the new design-by-testing approach for evaluating the minimum amount of hybrid reinforcement to be placed in an HRC element in bending can be summarized by the following general procedure:

1. Perform a bending test on the full-scale concrete member reinforced with a trial area of rebar A_s^* .
2. From the so-obtained experimental values of the effective cracking load P_{cr^*} and of the ultimate load P_u , compute the corresponding ductility index DI_s with Eq.(1.6).

3. Perform a bending test on the same full-scale concrete member, but reinforced with a trial fiber volume fraction V_f^* .
4. With the experimental values of P_{cr^*} and P_u , compute the related ductility index DI_f [Eq.(1.6)].
5. Determine the minimum area of rebar $A_{s,min}$ (in the case of LRC) and the minimum fiber volume fraction $V_{f,min}$ (in the case of FRC), with the two following equations [i.e., Eq.(2.22) and Eq.(3.27)]:

$$A_{s,min} = \frac{\zeta \cdot A_s^*}{DI_s + \zeta} \quad (5.4).a$$

$$V_{f,min} = \frac{\zeta \cdot V_f^*}{DI_f + \zeta} \quad (5.4).b$$

According to Eqs.(5.1), the coefficient ζ is equal to 1 or 0.7 for positive or negative values of the ductility index, respectively.

5. Fix an area of rebar $A_s < A_{s,min}$ and determine V_f , or fix an amount of fibers $V_f < V_{f,min}$ and determine A_s , with Eq.(4.5).

If the minimum area of sole rebar is required to be placed in a LRC element, it is sufficient to follow the steps 1-2, and to use Eq.(5.4).a. On the other hand, when the minimum fiber volume fraction of a FRC member is necessary, the steps 3-4 and Eq.(5.4).b have to be applied. This is also necessary when Eq.(4.6) (CEN 2004b) must be applied, before to compute the reduced area of rebar $A_s < A_{s,min}$ with Eq.(4.7). As a first approximation, the slope ζ in Eqs.(5.4) can also be assumed equal to 0.8, for any value of ductility index.

Finally, the proposed approach could also be adapted to the safety format used by building codes (ACI 2014, CEN 2004a, *fib* 2012a). Specifically, the upper bound functions defined by Eqs.(5.1) can be adjusted by means of a partial safety factor $\gamma > 1$, as commonly adopted in the design procedures (Figure 5.7):

$$DI = r - \frac{1}{\gamma} \quad 0 \leq DI \quad (5.5).a$$

$$DI = 0.7 \cdot \left(r - \frac{1}{\gamma} \right) \quad DI \leq 0 \quad (5.5).b$$

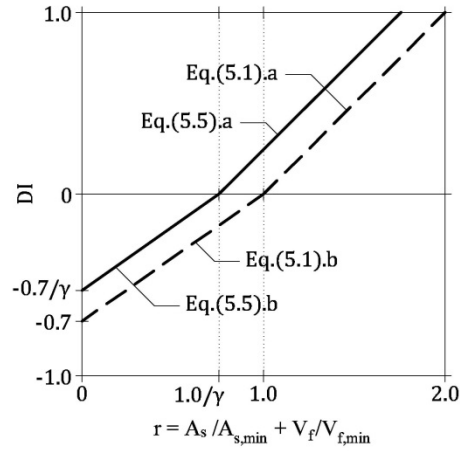


Figure 5.7: $DI-r$ design relationships for concrete beams.

To be more precise, as it can be observed in Figure 5.7, the value of the intercept in Eq.(5.1).b (i.e., -0.7) is increased to $-0.7/\gamma$, whereas the slopes of both Eqs.(5.5) are unchanged (i.e., 1 and 0.7). In other words, the functions depicted in Figure 5.7 are obtained by translating Eqs.(5.1) in the $DI-r$ plane, and they are two design relationships valid for all LRC, FRC and HRC beams.

As a result, the minimum reinforcements $A_{s,min}$ and $V_{f,min}$ could be computed by means of new conservative formulae:

$$A_{s,min} = \frac{\zeta \cdot A_s^*}{DI_s + \zeta/\gamma} \quad (5.6).a$$

$$V_{f,min} = \frac{\zeta \cdot V_f^*}{DI_f + \zeta/\gamma} \quad (5.6).b$$

where the coefficient ζ is equal to 1 or 0.7 for ductility indexes greater or smaller than zero, respectively.

Chapter 6

Minimum reinforcement of concrete segments for tunnel linings

6.1 Introduction

The combined use of continuous rebar and discrete fibers in HRC structural members is nowadays a largely adopted solution in the field of segmental and conventional tunneling (Caratelli et al. 2012, Chiaia et al. 2007, de la Fuente et al. 2012, Meng et al. 2016, Plizzari and Tiberti 2006). In the first case, a Tunnel Boring Machine (TBM) is used both for excavating soil or rock, by means of a rotating head, and for placing precast arch-shaped concrete segments. When a ring made of several precast segments is completed (Figure 6.1), it is used by the TBM as a contrast for advancing, and then a new construction cycle starts (Meda et al. 2016). On the other hand, a permanent lining is realized with cast-in-situ reinforced concrete in the case of conventional tunneling (Tiberti and Plizzari 2008). However, before this phase, the controlled blasting of a new portion of the tunnel cyclically takes place, hence the resulting material is removed, and a temporary lining is cast for stabilizing the excavation, e.g., with sprayed FRC (shotcrete).

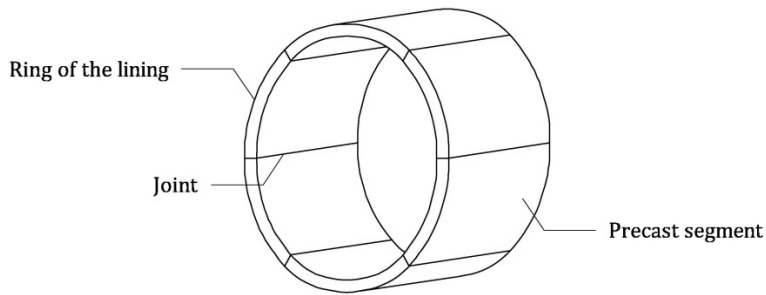


Figure 6.1: Ring of a precast concrete lining.

Since massive cross-sectional areas are common in both precast and cast-in-situ tunnel linings, as well as predominant state of compression in service, often these concrete members only require the minimum reinforcement (Chiaia et al. 2007, de la Fuente et al. 2012). In other words, even if the effects related to the design actions do not produce the cracking of the concrete cross-section, the presence of a certain amount of reinforcement must be assured in order to maintain the bearing capacity if a crack accidentally occurs (i.e., to avoid the brittle failure).

In such elements, where massive cross-sections are reinforced with low amounts of rebar, the addition of fibers may be highly effective, as their tensile contribution can be comparable with that of conventional reinforcement (Fantilli et al. 2016d). This can significantly reduce the amount of rebar in tunnel linings, with a consequent economy of the manufacture costs, both in terms of bare materials and labor, and of the construction times (Chiaia et al. 2009, Meda and Rinaldi 2014). In facts, the circular shape of such structures leads to many difficulties in handling and placing of conventional reinforcement. Moreover, the combined use of rebar and fibers is an optimal solution to carry both diffuses and localized stresses (Tiberti et al. 2014).

Since lightly reinforced HRC members are widely used in tunneling, the design-by-testing approach herein proposed to evaluate the brittle/ductile behavior of concrete elements can be a useful tool in this field. Therefore, the present Chapter deals with an example of structural application, with reference to the real case studied by Caratelli et al. (2011). The aim is to verify the equivalence of HRC segments, obtained combining rebar and fibers according to Eq.(4.5), with other elements reinforced by means of homogeneous solutions (i.e., only rebar or fibers). They are analyzed not only in pure flexure (i.e., in provisional phases), but also under combined axial and bending actions (i.e., in service conditions).

6.2 Concrete segments of the Brenner Base Tunnel

Brenner Base Tunnel (BBT) is an important underground infrastructure currently under construction between Fortezza (Italy) and Innsbruck (Austria). It is a part of the high-speed railway line which will connect Verona (Italy) and Munich (Germany). The path of BBT crosses rock formations made of ordinary granite, at a maximum depth of about 1,300 m, and is 55 km long (Zhao et al. 2014). The infrastructure consists of two single-track tunnels, transversely connected every 333 m, and a central exploratory tunnel, mainly excavated with a TBM.

Some precast concrete segments used in this context for the tunnel linings were studied in an experimental campaign performed by Caratelli et al. (2011). Due to the in-situ geotechnical conditions (rock specific load $\gamma_r = 26.5 \text{ kN/m}^3$, modulus of elasticity $E_r = 14 \text{ GPa}$, Poisson's ratio $\nu_r = 0.3$), the most part of the tunnel lining is subjected to small stresses, hence a light reinforcement is required for the segments (Caratelli et al. 2011). Referring to the lining cross-section, a ring having an external radius of 3 m is composed by six concrete segments (Figure 6.1). The considered segment shows a projected length equal to 3,650 mm, a depth $H = 200 \text{ mm}$, and a width $B = 1,500 \text{ mm}$ [Figure 6.2(a)]. In the experimental campaign carried out by Caratelli et al. (2011), two types of full-scale segments were realized. The LRC-type was cast with concrete having a cubic compressive strength $R_c = 50 \text{ MPa}$, and reinforced by 16 longitudinal steel rebar in tension, with diameter $\phi_s = 8 \text{ mm}$ (i.e., an area of reinforcement $A_s = 804 \text{ mm}^2$). The FRC-type was realized with a concrete having $R_c = 75 \text{ MPa}$, and reinforced with 40 kg/m^3 of steel fibers (i.e., a fiber volume fraction $V_f = 0.51 \%$). The fibers had a length $L_f = 30 \text{ mm}$ and a cross-sectional diameter $\phi_f = 0.35 \text{ mm}$.

Two un-notched LRC and FRC segments were tested in three point bending, along a span of 2,040 mm, as shown in Figure 6.2(a). The aim was to compare the flexural behavior of the two types of concrete segments, evaluated in terms of applied load P vs. crack width at bottom level \bar{w} [Figure 6.2(b)]. The applied force was measured by means of a load cell, whereas the crack width was recorded by two transducers applied to the segment intrados. The tests were performed by increasing the midspan deflection, measured with three vertical wire transducers, and the load was distributed on the whole width of the segments by means of a frame system.

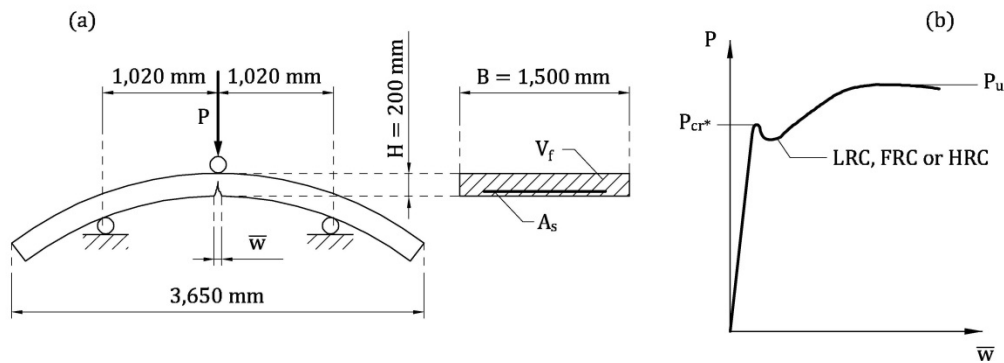


Figure 6.2: Three point bending test on a precast concrete segment (Caratelli et al. 2011): (a) test set-up; (b) applied load vs. crack width curve.

The present elements can be considered as statically determined beams subjected to only flexural actions. Indeed, the linear supports of the elements tested by Caratelli et al. (2011) were kept free to slide, differently from the test conditions presented by Meng et al. (2016), in which horizontal forces proportional to the vertical loads were applied at the ends of segments. Even if the test set-up adopted by Meng et al. (2016) is representative of the service conditions, the conventional loading method adopted Caratelli et al. (2011) reflects the static schemes of provisional phases (e.g., demolding, storage, handling, transportation, etc.), when the segments are typically subjected to bending actions (Meda and Rinaldi 2014). As a matter of fact, the most severe state of stress for the precast elements is usually related to transitory stages (Liao et al. 2015).

In addition to the three point bending tests, both LRC and FRC segments were also subjected to a concentrated force acting along the direction of the tunnel axis, increased up to a design value (Caratelli et al. 2011). The aim was to study the effects of the tensile splitting stresses induced during the construction phase by the trust actions of the TBM jacks (Meda et al. 2016, Plizzari and Tiberti 2006). However, the results of such punctual load tests are not considered herein, and other specific analyses should be performed to define the suitable reinforcement to prevent splitting cracks (Meda et al. 2016, Plizzari and Tiberti 2006).

6.3 Modelling the flexural behavior of BBT segments

By means of the general models presented in Chapters 2 and 3, the $P - \bar{w}$ curves of both LRC and FRC segments tested by Caratelli et al. (2011) are reproduced.

The material parameters used for this purpose are those which minimize the scatters of the predicted effective cracking and ultimate loads P_{cr^*} and P_u with respect to the corresponding experimental values. With these parameters, the flexural response of HRC members, made with the same materials of LRC and FRC elements but combining rebar and fibers, is simulated. As the two segments tested by Caratelli et al. (2011) are cast with different concrete mixtures, only the LRC segment is considered to identify the concrete strength (in addition to the parameters referred to the steel rebar), whereas the FRC element is used to define the properties of the fiber-reinforcement.

6.3.1 LRC segment

Despite the hypothesis of failure in presence of a single crack, the general model described in Section 2.2 is used to compute the flexural response of the LRC segment tested by Caratelli et al. (2011). However, the segment reinforced with an area of rebar $A_s = 804 \text{ mm}^2$ shows an hardening branch in the post cracking stage of the experimental $P - \bar{w}$ curve LRC_1 reported in Figure 6.3(a). The numerical curve LRC_1, depicted in the same Figure, is obtained by assuming a cylindrical compressive strength of concrete $f_c = 36.5 \text{ MPa}$. In addition, the steel of rebar (assumed to be placed only in tension) is defined by a yielding strength $f_y = 450 \text{ MPa}$, an effective depth $d = 180 \text{ mm}$, and good bond conditions at the interface between rebar and concrete (*fib* 2012a). The adopted compressive strength is slightly lower than the theoretical estimation (i.e., $f_c \cong 0.83 \cdot R_c = 41.5 \text{ MPa}$), but this difference can be due to the common experimental scatter.

Even if the numerical curve presents a certain discrepancy with respect to the experimental response [Figure 6.3(a)], the values of the loads P_{cr^*} and P_u reported in Table 6.1 are very similar. Such differences could also be due to a pre-cracking of the LRC segment tested by Caratelli et al. (2011), suggested by the reduced stiffness of the elastic branch in Fig.6.3(a). Nevertheless, the effective cracking is localized on the experimental curve for a load equal to 106 kN, as “*the first cracking occurs at a load level of 70 kN*”, but “*up to about 125 kN only one crack passes for both the instrument*” (Caratelli et al. 2011). Accordingly, P_{cr^*} is assumed to be the higher relative maximum reached during the growth of the first crack (Maldague 1965). On the other hand, P_u is taken at the yielding of reinforcement, according to the elastic-perfectly plastic constitutive law assumed for steel rebar in the general model (Section 2.2.2). Hence, as stated by Caratelli et al. (2011), “*the yielding can be located at 125 kN*”.

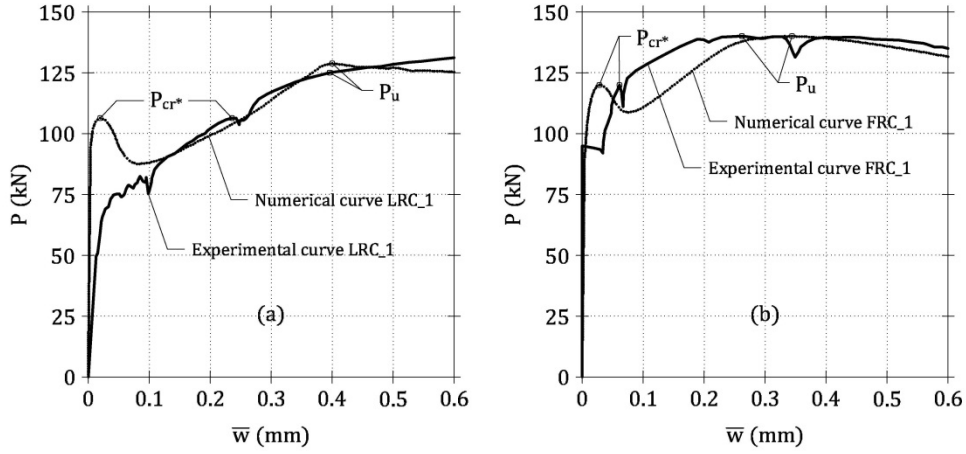


Figure 6.3: Numerical predictions of the P - \bar{w} flexural response referred to two concrete segments in comparison with the experimental curves obtained by Caratelli et al. (2011): (a) LRC segment; (b) FRC segment.

6.3.2 FRC segment

The general model presented in Section 3.2 is used herein to reproduce the experimental P - \bar{w} curve FRC_1 reported in Figure 6.3(b) as obtained by Caratelli et al. (2011). Such curve is the result of a three point bending test on the FRC segment, reinforced with an amount $V_f = 0.51$ % of steel fibers having a tensile strength $f_u = 1,000$ MPa. However, as the flexural response of cracked FRC is mainly affected by the fiber pull-out (Armelin and Banthia 1997, Naaman and Shah 1976, Nammur and Naaman 1989), the bond strength τ_{\max} used in the bond-slip model [i.e., Eqs.(3.14)] is the more significant parameter for describing the fiber-reinforcement. Specifically, in order to obtain the numerical curve FRC_1 of Figure 6.3(b), $\tau_{\max} = 1.765 \cdot f_c^{0.5} / (12.5 + \phi_f)$ is assumed as a variation of the model proposed by Fantilli and Vallini (2003), where a value of bond strength $\tau_{\max} = 1.572 \cdot f_c^{0.5} / (12.5 + \phi_f)$ was originally suggested for smooth steel fibers.

Also in this case, despite the numerical curve FRC_1 does not perfectly superpose the experimental result, the values of the effective cracking and ultimate loads are well fitted (Table 6.1). On the experimental curve, the loads P_{cr*} and P_u are localized at 120 and 140 kN, respectively, in accordance with the words used by Caratelli et al. (2011): “*the first recordable crack was detected at a load level of 95 kN. Following this stage, the stiffness remained almost constant up to 120 kN thanks to the stress transmitted along the cracks by the fiber reinforcement. The maximum bearing capacity was equal to 140 kN*”.

Table 6.1: Experimental and numerical values of effective cracking load and ultimate load, and numerical values of ductility index, referred to concrete segments reinforced with different amounts of rebar and/or fibers.

Segment	A_s (mm ²)	V_f (%)	P_{cr^*} (kN)		P_u (kN)		DI
			Exp.	Num.	Exp.	Num.	
LRC_1	804	0.00	106.45	106.39	125.29	128.82	0.21
FRC_1	0	0.51	119.68	119.98	139.95	139.98	0.17
LRC_0	603	0.00	/	102.31	/	99.69	-0.03
FRC_0	0	0.40	/	114.26	/	113.14	-0.01
HRC_0_1	151	0.30	/	99.08	/	100.04	0.01
HRC_0_2	302	0.20	/	98.25	/	99.12	0.01
HRC_0_3	452	0.10	/	97.42	/	97.90	0.00

6.4 Minimum reinforcement of concrete segments

The flexural response of both LRC and FRC segments as reinforced by Caratelli et al. (2011) can be used to identify the minimum amounts of rebar and fibers strictly necessary to prevent the brittle failure (i.e., $A_{s,min}$ and $V_{f,min}$). Accordingly, the values of the ductility indexes DI related to the numerical curves LRC_1 and FRC_1 are computed with Eq.(1.6) and reported in Table 6.1. Hence, by considering the trial area of rebar $A_s^* = 804 \text{ mm}^2$ in LRC segment and the trial fiber content $V_f^* = 0.51 \%$ in FRC segment, the proposed Eqs.(5.4) can be used by imposing $DI_s = 0.21$ and $DI_f = 0.17$, respectively (Table 6.1). Hence, as a first approximation of $A_{s,min}$, an area of rebar equal to 637 mm^2 is obtained, whereas $V_{f,min}$ is estimated to be 0.42% .

However, for a more precise evaluation of $A_{s,min}$ and $V_{f,min}$, an iterative procedure can be adopted. Specifically, the flexural response of both LRC and FRC segments, reinforced with the previous values of minimum reinforcement, is simulated by using the general models described in Section 2.2 and in Section 3.2, respectively. Hence, from the current values of ductility index, new minimum amounts of reinforcement can be evaluated with Eqs.(5.4). After few iterations, the present procedure allows to identify $A_{s,min} = 603 \text{ mm}^2$ (i.e., 12 steel rebar with $\phi_s = 8 \text{ mm}$) and $V_{f,min} = 0.40 \%$ (i.e., 31 kg/m^3 of steel fibers). Therefore, a small error of about 5% was obtained with the first application of Eqs.(5.4).

Figure 6.4(a) reports the numerical curve of the ideal concrete segment reinforced with $A_{s,min}$ (i.e., LRC_0), whereas that of the ideal segment containing $V_{f,min}$ (i.e., FRC_0), is depicted in Figure 6.4(b). Such curves are obtained with the

over-mentioned general models for predicting the flexural response of LRC and FRC members. As it can also be observed in Table 6.1, both the $P - \bar{w}$ curves show $P_u \cong P_{cr^*}$, then $DI \cong 0$ [Eq.(1.6)].

Having separately determined the values of $A_{s,min}$ and $V_{f,min}$ in LRC and FRC segments, respectively, different amounts of hybrid reinforcement corresponding to the brittle/ductile transition in an HRC member, characterized by the same mechanical and geometrical properties, can be evaluated according to Eq.(4.5) [Figure 6.5(a)]. Among all the possible combinations, the three couples of values $A_s/A_{s,min} = 0.25$ and $V_f/V_{f,min} = 0.75$, $A_s/A_{s,min} = 0.50$ and $V_f/V_{f,min} = 0.50$, $A_s/A_{s,min} = 0.75$ and $V_f/V_{f,min} = 0.25$, are illustrated in Figure 6.5(a). At limits, the minimum amounts of rebar and fibers in the two ideal segments LRC_0 and FRC_0 can be found in Figure 6.5(a), when $V_f/V_{f,min} = 0$ and $A_s/A_{s,min} = 0$, respectively.

6.5 Modelling the flexural behavior of HRC segments

The combined model proposed in Chapter 4 is applied herein to predict the $P - \bar{w}$ curves of three ideal HRC segments, at brittle/ductile transition and identified with the labels HRC_0_1, HRC_0_2, and HRC_0_3. Such concrete segments are similar to those tested by Caratelli et al. (2011), but they are reinforced with both rebar and fibers. The concrete strength assumed for the hybrid members is that of LRC segment (i.e., $f_c = 36.5$ MPa), and the parameters defining the steel rebar as well (i.e., $f_y = 450$ MPa, $d = 180$ mm, and good bond conditions). As in the case of LRC, the conventional reinforcement is assumed to be placed only at the bottom level of the concrete cross-section [Figure 6.2(a)]. On the other hand, the fiber-reinforcement is made with steel fibers having $L_f = 30$ mm, $\phi_f = 0.35$ mm, $f_u = 1,000$ MPa, and $\tau_{max} = 1.765 \cdot f_c^{0.5} / (12.5 + \phi_s)$, in analogy with the case of FRC segment.

The three combinations of $A_s/A_{s,min}$ and $V_f/V_{f,min}$ represented in Figure 6.5(a), which fulfill the condition of minimum ductility $DI = 0$ [i.e., Eq.(4.5)], are considered for reinforcing the segments HRC_0_X, where X = 1, 2, or 3 according to the hybrid reinforcement. In particular, as reported in Table 6.1, in the case of segment HRC_0_1, $A_s = 151$ mm² (i.e., 3 rebar with $\phi_s = 8$ mm) and $V_f = 0.30$ % are used; segment HRC_0_2 contains $A_s = 302$ mm² (i.e., 6 rebar with $\phi_s = 8$ mm) and $V_f = 0.20$ %; and finally segment HRC_0_3 is reinforced with $A_s = 452$ mm² (i.e., 9 rebar with $\phi_s = 8$ mm) and $V_f = 0.10$ %.

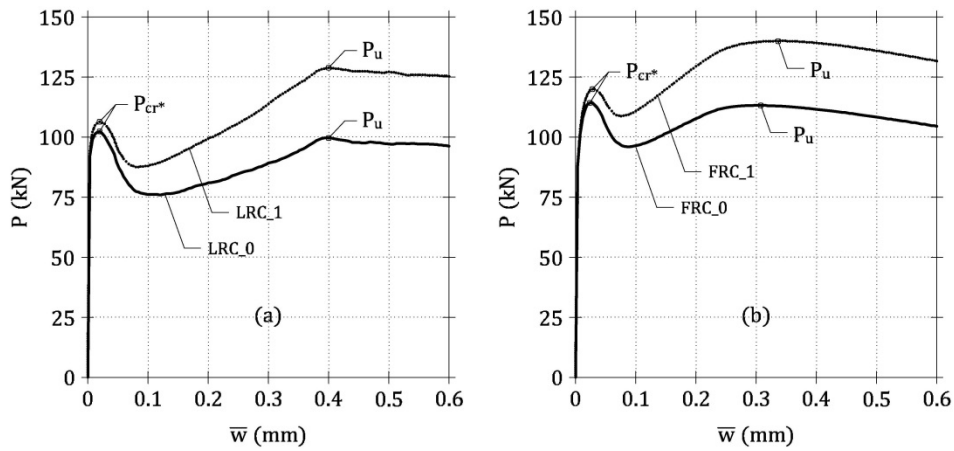


Figure 6.4: Numerical predictions of the $P - \bar{w}$ flexural response referred to two ideal concrete segments at brittle/ductile transition, in comparison with the numerical curves reproducing the test results of Caratelli et al. (2011): (a) LRC segments; (b) FRC segments.

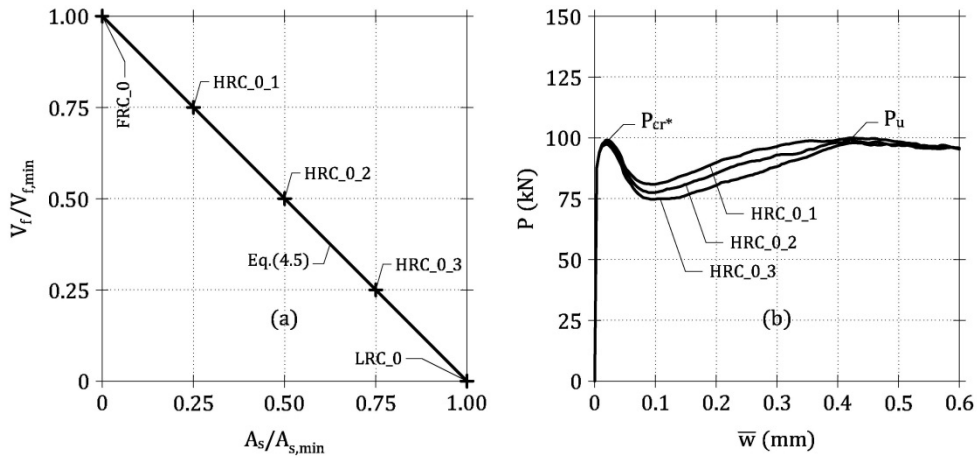


Figure 6.5: Minimum reinforcement in HRC segments: (a) Eq.(4.5) for combining rebar and fibers; (b) numerical predictions of the $P - \bar{w}$ flexural response of three ideal HRC segments at brittle/ductile transition.

The $P - \bar{w}$ curves of these three ideal segments are depicted in Figure 6.5(b). All of them reproduce the brittle/ductile transition, and therefore they are in agreement with Eq.(4.5). This threshold condition can also be recognized in Table 6.1, as all the three segments exhibit $P_u \cong P_{cr^*}$ (i.e., $DI \cong 0$). The reliability of these results is supported by the fact that the prediction of P_u and P_{cr^*} is accurate

in the case of both LRC and FRC segments (Table 6.1), regardless of the shape showed by the $P - \bar{w}$ curves (Figure 6.3).

Furthermore, the load *vs.* deflection curves of Figure 6.5(b) put into evidence the favorable effect of the fibers in reducing the crack width, since in the post-cracking stage, for an assigned P level, the values of \bar{w} decrease with increasing V_f , as in the experimental campaign of Caratelli et al. (2011). On the contrary, for growing A_s , the $P - \bar{w}$ curves show a more clearly defined yielding point in Figure 6.5(b), due to the higher influence of the steel rebar on the total amount of hybrid reinforcement.

6.6 HRC segments under axial and bending actions

As tunnel linings in service are mainly subjected to axial force N and bending moment M , these structures can be designed or assessed by means of interaction diagrams $M - N$ (Chiaia et al. 2009, de la Fuente et al. 2012, Meda and Rinaldi 2014). Specifically, referring to the concrete segments herein considered, the points $[N_{Ed}, M_{Ed}]$ related to the internal actions should fall within the feasible region $M_{Rd} - N_{Rd}$, enveloped by all the couples of resisting bending moment and axial force, in any cross-sections. Hence, to verify if the segments analyzed herein can be used in BBT, it is necessary to model the tunnel lining in final conditions (to estimate the internal actions N_{Ed} and M_{Ed}) and the ultimate limit state response of the concrete cross-sections (for determining the resisting domain $M_{Rd} - N_{Rd}$).

6.6.1 Modelling the concrete lining in final conditions

Since BBT crosses the Alps at a large depth (Zhao et al. 2014), for the sake of simplicity, only a portion of the soil surrounding the tunnel lining is modelled. In addition, the interaction between the three tunnels currently under construction (Zhao et al. 2014) is neglected herein. Due to the predominant longitudinal dimension of the lining, each transverse cross-section can be considered as a symmetry section, and a plain strain problem can be solved (Timoshenko and Goodier 1970). In accordance with the strategy adopted by de la Fuente et al. (2012) in a similar case, a 65×65 m square block of rock surrounding the tunnel cross-section [Figure 6.6(a)] is analyzed by means of the commercial finite element code PRO_SAP (2S.I. 2017).

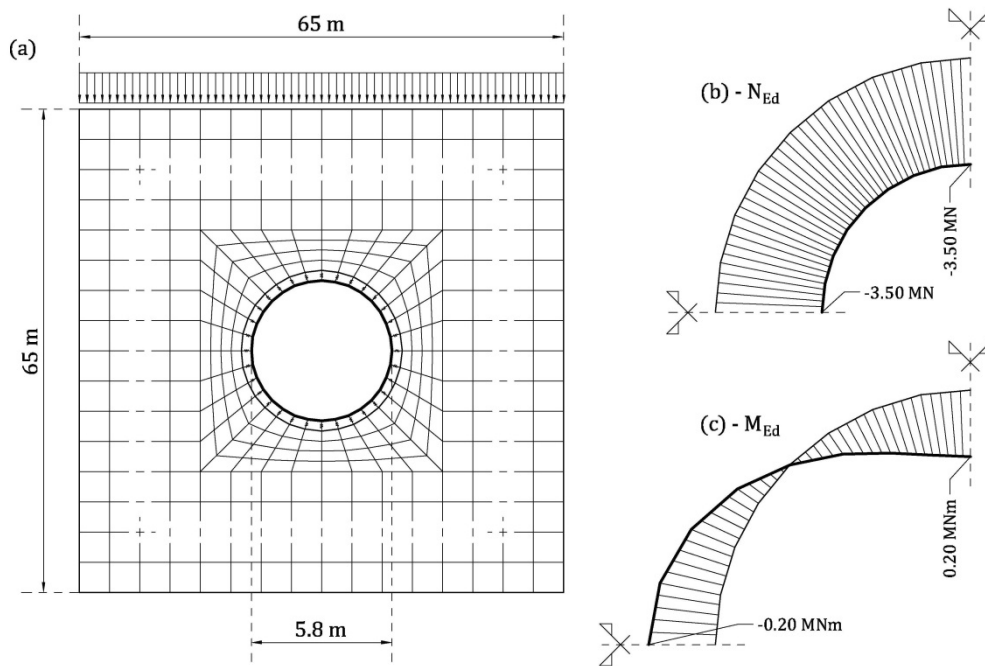


Figure 6.6: Structural analysis of the concrete lining in final conditions: (a) finite element model; (b) axial force; (c) bending moment.

The material behavior of this block, schematized with shell elements, is described by the parameters $E_r = 14$ GPa, and $\nu_r = 0.3$ (Caratelli et al. 2011). The missing depth of the soil up to the ground level is simulated with a uniformly distributed load acting on the top of the block, representing a rock with $\gamma_r = 26.5$ kN/m³ [Figure 6.6(a)]. Concerning the tunnel lining, the circular ring is modelled with beam elements made of concrete [Figure 6.6(a)] and having $E_c = 33$ GPa, $\nu_c = 0.2$, and $\gamma_c = 25.0$ kN/m³ (fib 2012a). To take into account the soil-structure interaction in a simple manner, only compression loads are transferred by the connections between the concrete ring and the block of rock.

By considering only gravity loads in dry conditions (i.e., the self-weights of concrete ring and block of rock, and the load acting at top of the block as well), the internal actions of the tunnel lining can be easily determined. In particular, the diagrams of axial force N_{Ed} and bending moment M_{Ed} on a quarter of the ring, considering $B = 1,500$ mm, are plotted in Figure 6.6(b-c). By means of the finite element analysis, the maximum shear force $V_{Ed} = 134.90$ kN can also be obtained. Since the perfect connection is assumed in the model between the six segments of a ring, the analyzed structure shows a higher stiffness than in reality. Hence, this

prediction of the gravity actions in dry conditions is conservative. However, to fully verify the structural safety of the lining, additional load combinations should be taken into account (e.g., including hydraulic and seismic actions).

The minimum shear capacity $V_{Rd} = 142.69$ kN is evaluated according to Eurocode 2 (CEN 2004a), and by conservatively neglecting the favorable contribution of compressive stresses, but also the improvement in shear strength given by the fibers (*fib* 2010). Therefore, the thickness of the concrete segments given by Caratelli et al. (2011) (i.e., $H = 200$ mm) is sufficient to carry V_{Ed} even in the absence of shear reinforcement, as recommended by the Guidelines for the design of shield tunnel lining (ITA-WG2 2000).

6.6.2 Evaluating the interaction diagram of lining cross-sections

According to Chiaia et al. (2009), the hypothesis of planar strain profile on the whole concrete cross-section is adopted for determining the $M_{Rd} - N_{Rd}$ domain of concrete cross-sections. To compute this interaction diagram, the equivalent strain ε_c is introduced when $w > 0$, i.e., when the strain at peak of tensile stress ε_{ct} is attained (Fantilli et al. 2016b):

$$\varepsilon_c = \varepsilon_{ct} + \frac{w}{L_f} \quad (6.1)$$

In Eq.(6.1), for the sake of simplicity, the first term of Eq.(3.23) is assumed to be constant and equal to the strain at peak of tensile stress. As the most relevant contribution to ε_c is given by w (de Montaignac et al. 2012), this approximation is acceptable.

To define the limit state configurations of a concrete cross-section, strain limits must be imposed to ε_c . In the general case of HRC, the strain at peak of stress ε_{c1} is considered in compression, whereas the ultimate strain in tension ε_{cu} is computed with Eq.(6.1), starting from the crack width corresponding to P_u in the $P - \bar{w}$ diagram. For the ideal segments previously studied, $\varepsilon_{c1} = 2.27$ ‰ (*fib* 2012a), and $\varepsilon_{cu} = 14.08$ ‰ [as the ultimate crack width is 0.42 mm for all the three curves in Figure 6.5(b)]. Since ε_{cu} is smaller than the design strain capability of rebar, i.e., 67.5 ‰ for an hardening steel grade C (CEN 2004a), it is conservative to assume this limit in tension both for fiber-reinforcement and rebar.

The seven limit state configurations, and the consequent six fields, corresponding to positive bending moments acting on the HRC cross-section depicted in Figure 6.7(a), are represented in Figure 6.7(b). Specifically, fields 1-3 are defined when the strain at bottom level is fixed at ε_{cu} , whereas that at top progressively decreases from ε_{cu} to $-\varepsilon_{c1}$. On the other hand, fields 4-6 correspond to the limit state configurations in which strain at top level is fixed at $-\varepsilon_{c1}$, and strain at bottom progressively decreases from ε_{cu} to $-\varepsilon_{c1}$. Six additional fields can be found by inverting the sign of the curvature given to the HRC cross-section.

For each limit state configuration, the distribution of stresses σ_c in the concrete matrix is known by means of the Sargin's parabola described by Eq.(2.12) (*fib* 2012a), when $\varepsilon_c < 0$, and of the linear elastic law [Eq.(2.13)], when $0 \leq \varepsilon_c \leq \varepsilon_{ct}$. In addition, stress σ_c vs. crack width w relationships, obtained with the procedure explained in Section 3.2, are used when $\varepsilon_c > \varepsilon_{ct}$ (i.e., when $w > 0$), and the elastic-perfectly plastic stress σ_s vs. strain ε_s law [Eq.(2.15)] is applied to steel rebar. Accordingly, the resisting axial force N_{Rd} and the resisting bending moment M_{Rd} can be computed by imposing two equilibrium equations to the axial stresses:

$$N_{Rd} = \int_{A_c} (\sigma_c) dA + \sigma_s \cdot A_s \quad (6.2).a$$

$$M_{Rd} = \int_{A_c} (\sigma_c \cdot y) dA + \sigma_s \cdot A_s \cdot \left(d - \frac{H}{2} \right) \quad (6.2).b$$

where A_c = cross-sectional area of concrete, y = vertical coordinate of the concrete cross-section, having the origin at mid-level (even if in an HRC cross-section it does not coincide with the centroid).

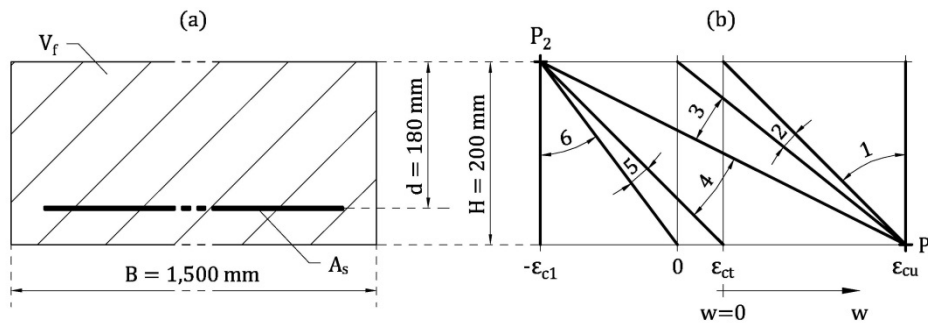


Figure 6.7: Evaluation of interaction diagrams: (a) concrete cross-section; (b) limit state configurations.

The whole resisting domain $M_{Rd}-N_{Rd}$ can be evaluated by varying the assigned strain configuration within the twelve limit strain fields. This procedure is applied to the segments LRC_1 and FRC_1, as tested by Caratelli et al. (2011), by assuming the parameters determined in Section 6.3 and obtaining the curves presented in Figure 6.8. In the same Figure, the interaction diagrams of the ideal segments LRC_0 and FRC_0 are also depicted. On the other hand, the $M_{Rd}-N_{Rd}$ domains referred to the three HRC_0 segments are reported in Figure 6.9, where they are put in comparison with those of segments LRC_0 and FRC_0.

As it can be observed in Figure 6.8, LRC_0 and FRC_0 segments show a $M_{Rd}-N_{Rd}$ diagram slightly smaller than those of LRC_1 and FRC_1 members, respectively, in accordance with the $P-\bar{w}$ curves of Figure 6.4. However, the feasible regions of all the segments are able to contain the points $[N_{Ed}, M_{Ed}]$ (Figure 6.8). For both the LRC segments, an asymmetric resisting domain can be observed in Figure 6.8, as rebar are only placed at the bottom level of the cross-section in Figure 6.2(a). Accordingly, when $N = 0$ in Figure 6.8, a negligible bearing capacity for negative bending moments is shown by LRC segments (i.e., the interceptions of the $M_{Rd}-N_{Rd}$ diagram with the negative vertical axis is near to the origin), unlike when $M > 0$. On the other hand, both the interaction diagrams referred to the FRC cross-sections are perfectly symmetric with respect to the horizontal axis (Figure 6.8), as the response of the fiber-reinforcement alone is equal for both positive and negative bending moments.

Referring to Figure 6.9, the five interaction diagrams substantially coincide for $M > 0$, showing the equivalence of the adopted hybrid reinforcements with respect to the homogeneous reinforcing systems of segments LRC_0 and FRC_0. This is true not only in pure flexure [Figure 6.5(b)] but also under combined axial force and positive bending moment. In other words, the adopted design-by-testing procedure [i.e., Eq.(4.5)] provides suitable combinations of rebar and fibers for maintaining the feasible region of the LRC cross-section, also when the amount of rebar is reduced. Conversely, for negative moments the $M_{Rd}-N_{Rd}$ diagrams are not superposed [Figure 6.9], due to the absence of rebar at the top level of the HRC and LRC cross-sections [Figure 6.2(a)]. In fact, in the case of HRC segments, only the fibers assure a resisting contribution in tension for $M < 0$, because the bottom rebar are in compression, then the effect of different V_f can be recognized in Figure 6.9. This is shown by the different resisting moments in the absence of axial force. When $V_f = 0$, such resisting moment is almost nil for the LRC cross-section, whereas that of the FRC segment is the greatest in absolute value. As a

result, the three resisting domains of the hybrid cross-sections are enveloped by those of LRC and FRC members (Figure 6.9).

On the opposite, the positive resisting moments in the absence of axial force (i.e., M_u in Figure 6.9) appear very similar. In particular, the values 54.85, 53.44, and 52.06 kNm are defined by the interaction domains of the segments HRC_0_1, HRC_0_2, and HRC_0_3, respectively. Since the related ultimate loads are 91.42, 89.06, and 86.87 kN, the proposed procedure for determining the $M_{Rd} - N_{Rd}$ diagrams underestimates P_u of about 10 % (Table 6.1), giving lightly conservative resisting domains. Nevertheless, the feasible regions depicted in Figure 6.9 contain the points $[N_{Ed}, M_{Ed}]$ previously determined for the different finite elements which model the cross-sections of a tunnel like BBT [Figure 6.6(b-c)], as studied by Caratelli et al. (2011).

Since the positive branches of the five $M_{Rd} - N_{Rd}$ diagrams depicted in Figure 6.9 are practically superposed, it can be useful to compare the feasible regions when $M < 0$. To do this, the efficiency index of fiber-reinforcement I_{FRC} , recently proposed by Fantilli et al. (2016d), can be adapted to the present case:

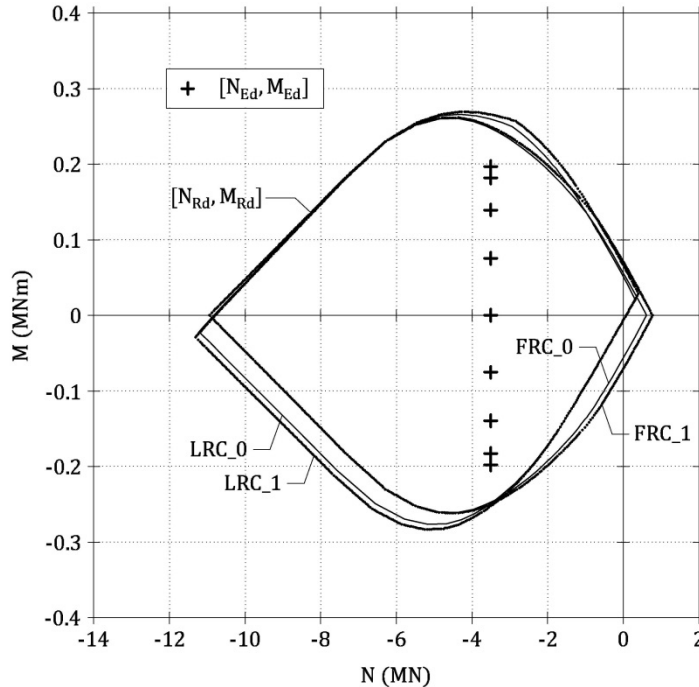


Figure 6.8: Interaction diagrams referred to the LRC and FRC segments compared with the internal actions in final conditions.

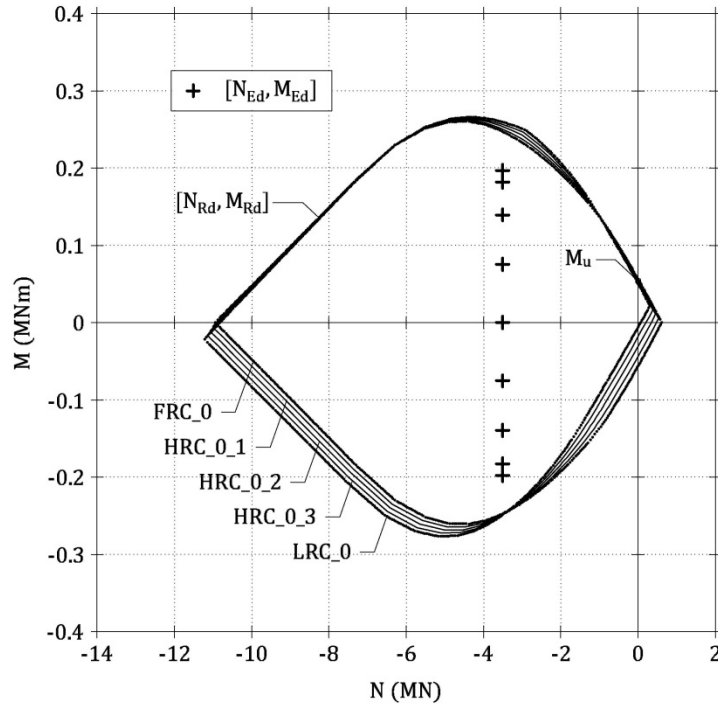


Figure 6.9: Interaction diagrams referred to the ideal concrete segments at brittle/ductile transition, compared with the internal actions in final conditions.

$$I_{\text{FRC}} = \frac{M_{u,2} - M_{u,1}}{M_{u,1}} \quad (6.3)$$

where $M_{u,2}$ = negative resisting bending moment, for a given axial force N , of a concrete cross-section containing rebar and/or fibers; and $M_{u,1}$ = negative resisting bending moment, for a given N , of the corresponding LRC cross-section.

The variation of I_{FRC} as a function of N in the five concrete segments at brittle-ductile transition can be observed in Figure 6.10. When the axial force is increased, growing values of I_{FRC} can be observed in the concrete cross-sections containing fibers (Figure 6.10). This is particularly true in the FRC_0 segment, which shows the smallest values of I_{FRC} for high compressive forces and the higher effectiveness of fiber-reinforcement for $N \rightarrow 0$. Obviously, I_{FRC} is always nil for LRC_0, whereas the $I_{\text{FRC}}-N$ curves of the hybrid segments fall within those of LRC_0 and FRC_0 segments. In all the cases of segments containing fibers, I_{FRC} equates zero for $N \cong 3.5$ MN. Therefore, as $N_{\text{Ed}} = 3.5$ MN is the result of the structural analysis [Figure 6.6(b)], the five solutions herein studied are substantially equivalent in the case of BBT, from a mechanical point of view.

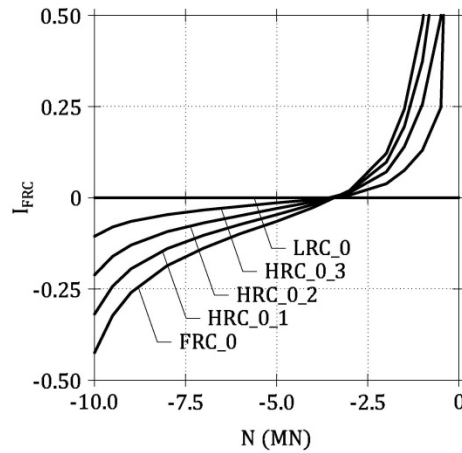


Figure 6.10: Efficiency index of fiber-reinforcement (Fantilli et al. 2016d) as a function of the axial force referred to the ideal concrete segments at brittle/ductile transition.

6.7 Discussion of the results

The resisting domains $M_{Rd} - N_{Rd}$ of Figure 6.9 and the $P - \bar{w}$ curves of Figure 6.5(b) demonstrate that, beyond the homogeneous solutions evaluated by Caratelli et al. (2011) for reinforcing the segments of BBT (i.e., only rebar or fibers in LRC or FRC segments, respectively), many equivalent hybrid reinforcements exist. As a consequence, the reinforcing system for concrete members in bending at brittle/ductile transition, but also in presence of axial force, can be designed by combining rebar and fibers according to Eq.(4.5). If the mechanical responses are equivalent, as in the case of BBT (Figure 6.10), A_s and V_f can be calibrated in the way which optimizes the total manufacture cost (i.e., the costs of bare materials and labor) and the concrete workability, deeply influenced by the fibers (Bayasi and Soroushian 1992). It is worth noting that the use of suitable amounts of fibers allows to avoid an onerous double level of rebar, at bottom and top of the concrete cross-section, when both positive and negative bending moments need to be carried. This could be particularly useful if, differently from the case of BBT (Caratelli et al. 2011), the tunnel lining is located at low depth in the soil, where small axial forces arise in the structure and the resisting domain need to be as large as possible near the origin (Figure 6.9), e.g., in the cast-in-situ tunnel lining designed by Chiaia et al. (2009). In such situation, the limit case of a FRC segment provides the best response for both positive and negative bending

moments. In the case of BBT, this is shown by the curve FRC_0 of Figure 6.10, which exhibits the higher I_{FRC} when $N \rightarrow 0$.

Additionally, the use of Eqs.(5.4) for estimating $A_{s,\text{min}}$ and $V_{f,\text{min}}$ appears really effective in the present structural application, especially if an iterative procedure is adopted. Such procedure requires to know the $P - \bar{w}$ (or the $P - \delta$) curves of trial LRC and FRC members, and is summarized by the following points (Figure 6.11):

1. By means of the general models described in Chapter 2 and Chapter 3, perform a back-analysis in order to determine the mechanical properties of the materials used to cast the two concrete elements.
2. As a first approximation, compute the values of $A_{s,\text{min}}$ and $V_{f,\text{min}}$ with the proposed Eqs.(5.4), by using the amounts of reinforcement and the ductility indexes of the tested elements.

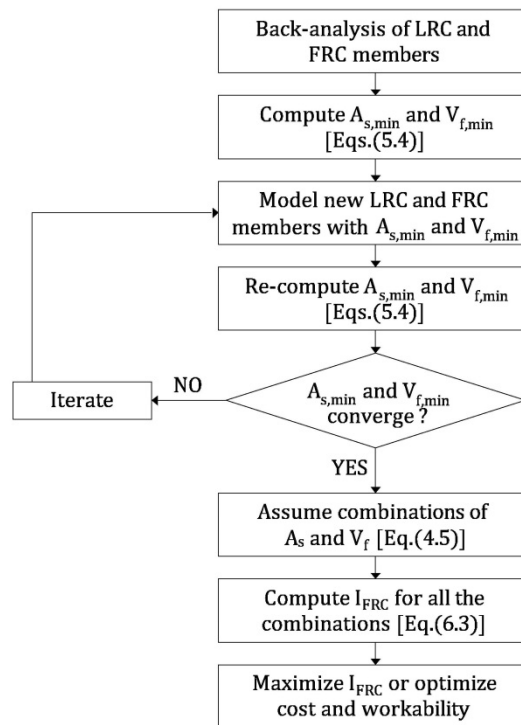


Figure 6.11: Flow-chart of the proposed procedure for evaluating the optimal hybrid reinforcement in an HRC member.

3. Reproduce the flexural response of a LRC member reinforced with the estimation of $A_{s,\min}$ and of a FRC member containing the previous value of $V_{f,\min}$.
4. As in step 2, by means of the amounts of reinforcement and the ductility indexes related to the previous simulations, compute the new values of $A_{s,\min}$ and $V_{f,\min}$ with Eqs.(5.4).
5. Go back to step 3, and then repeat the procedure until the convergence of $A_{s,\min}$ and $V_{f,\min}$ is achieved.
6. Assume different combinations of rebar and fibers [i.e., $A_s < A_{s,\min}$ and $V_f < V_{f,\min}$] which guarantee to respect the condition $DI = 0$ [i.e., Eq.(4.5)].
7. For all the different combinations of rebar and fibers, evaluate the corresponding values of I_{FRC} with Eq.(6.3).
8. Choose the solution with the higher I_{FRC} . If the values of I_{FRC} are the same for different combinations of rebar and fibers, choose that which optimizes the total manufacture cost and the workability of the concrete mixture.

Chapter 7

Ductility index as functional unit in ecological and mechanical analyses

7.1 Introduction

As concrete industry is responsible of high carbon dioxide emissions (Fantilli and Chiaia 2013b), new solutions are needed to obtain more environmental-friendly cement-based composites. Thus, an increasing interest on the study of the ecological performances of concrete structures can be found in the current literature (Damineli et al. 2010, Fantilli and Chiaia 2013c, Habert and Roussel 2009, Kawai et al. 2016, Mueller et al. 2016). However, the improvement of environmental performances often corresponds to a detriment of mechanical properties (Fantilli and Chiaia 2013c), and therefore combined ecological and mechanical analyses should be performed.

In this frame, compressive strength is generally assumed to be the functional unit of concrete, to which the inputs and outputs of a life-cycle assessment must be referred (Damineli et al. 2010). Nevertheless, in several applications the functional unit should take into account more than the mere compressive strength (Fantilli et al. 2016e). For instance, to achieve the best combined ecological and mechanical performances of high-strength but brittle concretes, material ductility needs to be enhanced (Fantilli and Chiaia 2013b). In concrete members subjected to bending actions, flexural strength and fracture toughness are also important properties. In such elements, without modifying the compressive strength,

bending capacity and ductility can be increased if fibers are added to the cementitious matrix (Balaguru and Shah 1992, Bentur and Mindess 1990).

In the present Chapter, three different examples of combined ecological and mechanical analyses between two lightweight cement-based composites (Fantilli et al. 2016e) are proposed. The ecological and mechanical performances of such concretes, some of them reinforced with short plastic fibers, are measured and compared with respect to different functional units, including the ductility index *DI* introduced in Chapter 1. Both the composites, according to the definition given by Model Code 2010 (*fib* 2012a), are lightweight concretes, as they show a density which varies between 800 and 2,000 kg/m³.

The first of the two composites is a Traditional Lightweight Concrete (TLC), where expanded clay particles replace stone aggregates. In fact, the usual way to reduce the mass of normal weight structural concrete is to use cellular particles as aggregates. These aggregates are generally produced by heating raw materials (e.g., shale, clay, slates, fly ashes, etc.) to incipient fusion, and then cooling them in the so-called pyroprocessing method (ACI 2003). TLC is mainly used to reduce the mass, and consequently the dead loads and the seismic actions, of both new and existing structures, and to facilitate transportation and placement of precast elements. In general, to justify the use of TLC, which is more expensive than normal weight concrete, a lower cost of the project and/or an improved functionality must be attained (ACI 2003). This is the case of the precast plates proposed by Fantilli et al. (2015) for maintenance operations on the sidewalks of an existing bridge. Specifically, a TLC containing expanded clay aggregates was tailored to facilitate the lift of the plates, which were reinforced with plastic fibers in place of the traditional steel rebar.

With respect to this solution, a more environmental-friendly lightweight concrete can be realized by using grinded rubber, obtained from end-of-life tires, as non-conventional aggregate (Ganjian and Khorami 2009, Najim and Hall 2010, Siddique and Naik 2004). Indeed, also the density of rubber granulates [with the dimensions of grains comprised between 0.8 and 20 mm according to CEN (2010)] is lower than that of the stone aggregates. The use of rubber in the concrete industry is convenient from an environmental point of view. Specifically, hundreds of millions scrap-tires are generated each year worldwide, and their landfilling is becoming unacceptable due to the rapid depleting of the sites and to the associated environmental risks (Siddique and Naik 2004). Nevertheless, the presence of the non-conventional aggregate reduces the compressive strength of

Rubber Lightweight Concrete (RLC), as evidenced in several studies (Ganjian and Khorami 2009, Najim and Hall 2010, Siddique and Naik 2004). In addition, concrete class reduces with increasing contents of rubber, and sometimes becomes lower than the minimum values required for structural uses (*fib* 2012a).

In the present Chapter, uniaxial compression tests on cylinders and three point bending tests on full-scale one-way plates, referred to both TLC and RLC, are analyzed. Although TLC and RLC mixtures can lead to different compressive strength, they were accurately tailored in order to behave in the same way under the bending actions of a structural application (Fantilli et al. 2015).

7.2 Experimental campaign

The experimental campaign described in this Chapter was carried out at the Materials and Structures Experimental Laboratory (MASTRLAB) – Department of Structural, Building and Geotechnical Engineering (DISEG) of Politecnico di Torino (Italy). Part of such research work has been previously published in Fantilli et al. (2016e).

7.2.1 Materials

Three TLC mixtures, made with expanded clay aggregates and named TLC_0, TLC_7, and TLC_10, are taken into consideration (Table 7.1). A cubic meter of such mixtures, used in a real application (Fantilli et al. 2015), is reinforced with 0, 7, and 10 kg of short plastic fibers, respectively. As the plastic fibers have a density of 910 kg/m^3 , the fiber contents reported in Table 7.1 correspond to the three fiber volume fractions $V_f = 0, 0.77, \text{ and } 1.10 \%$. The fibers (with diameter $\phi_f = 0.48 \text{ mm}$, length $L_f = 54 \text{ mm}$, elastic modulus $E_f = 5.75 \text{ GPa}$, and tensile strength $f_u > 620 \text{ MPa}$) are commercially available and made with a mix of polymers (mainly polypropylene). Due to the selected components reported in Table 7.1, TLC mixtures have a density of about $1,650 \text{ kg/m}^3$.

With respect to these traditional cement-based composites, new and more environmental-friendly lightweight concrete mixtures can be tailored (Fantilli et al. 2016e). In the present case, the content of cement is reduced of about 30 %, and rubber granulates substitute a portion of the aggregates (Table 7.2). Obviously, due to the higher water/cement ratio (twice than that of TLC) and to the presence of rubber, RLC mixtures will show a lower compressive strength. However, this would not alter significantly the behavior of lightly reinforced FRC

members in bending, if the failure in tension occurs. The mixtures RLC_0, RLC_5, and RLC_12 contain 0, 5, and 12 kg/m³ of the same plastic fibers previously used in TLC (Table 7.2), respectively (i.e., $V_f = 0, 0.55, \text{ and } 1.32 \%$). Although the density of these mixtures (i.e., 1,900 kg/m³) is higher than that of TLC, they can still be considered lightweight concretes according to Model Code 2010 (*fib* 2012a).

7.2.2 Test set-up

Three cylindrical specimens, having an height of 300 mm and a base diameter of 150 mm [Figure 7.1(a)], were cast with each of the six mixtures previously described. Such samples were subjected to uniaxial compressive loads through a MTS testing machine (maximum load capacity = 1,000 kN), by imposing a constant velocity of the stroke (i.e., 0.037 mm per minute). In addition to the average displacement measured on the whole height of the specimens, two transducers were placed on the central part of each cylinder to evaluate the local strain on a base of 100 mm [Figure 7.1(a)].

Table 7.1: Material components referred to 1 m³ of TLC.

Component	TLC_0	TLC_7	TLC_10
Water (kg)	140	140	140
Cement Type II A-LL 42.5R (kg)	500	500	500
Stone aggregate (kg)	700	700	700
Expanded clay aggregate 3-8 mm (kg)	300	300	300
Superplasticizer (l)	4.8	4.8	4.8
Polypropylene fibers (kg)	0	7	10

Table 7.2: Material components referred to 1 m³ of RLC.

Component	RLC_0	RLC_5	RLC_12
Water (kg)	168	168	168
Cement Type II A-LL 42.5R (kg)	352	352	352
Stone aggregate (kg)	1,131	1,123	1,110
Rubber granulates 3-20 mm (kg)	243	241	238
Superplasticizer (l)	6	6	6
Polypropylene fibers (kg)	0	5	12

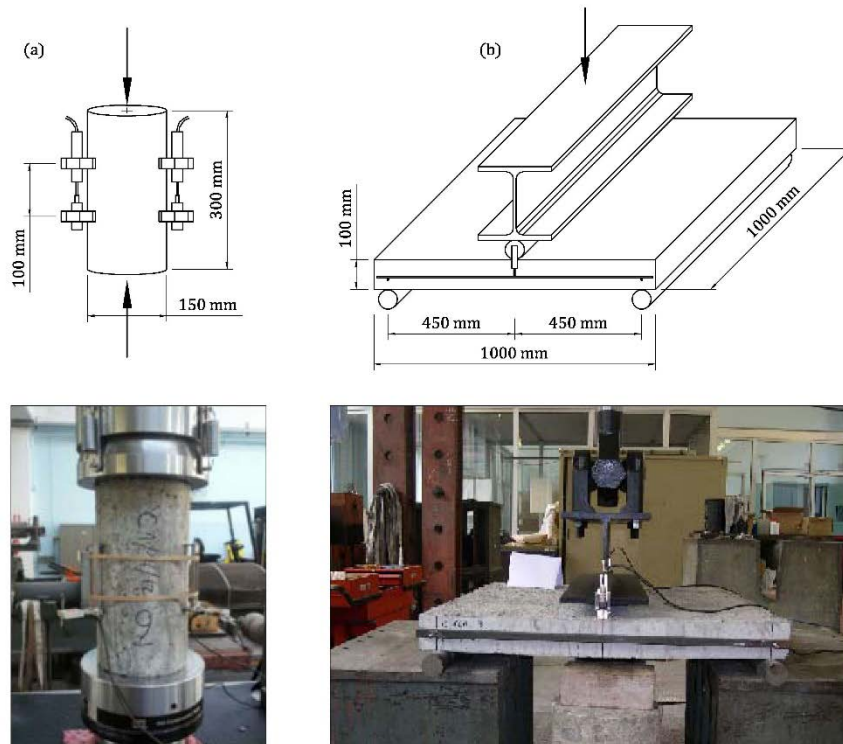


Figure 7.1: Experimental campaign on the six lightweight mixtures: (a) uniaxial compression tests; (b) three point bending tests.

Three $1,000 \times 1,000 \times 100$ mm plates [Figure 7.1(b)] were also cast by using all the TLC and RLC mixtures defined in Table 7.1 and Table 7.2, respectively. Such plates, which do not contain any steel rebar, correspond to the full-scale structure of the simply supported sidewalk analyzed by Fantilli et al. (2015). Accordingly, they were tested in three point bending [Figure 7.1(b)]. The load, distributed along the midsection through a steel beam, was applied by means of a MTS machine with a capacity of 100 kN. Two transducers were used to determine the midspan deflection (depurated by the support displacements), as the stroke increased at a constant velocity of 0.360 mm per minute.

7.3 Experimental results

7.3.1 Uniaxial compression tests

Figure 7.2 shows the stress vs. strain ($\sigma_{lc} - \varepsilon_{lc}$) curves of the compression tests on the concrete cylinders depicted in Figure 7.1(a). During the ascending branch the strains are computed with the measures of the two transducers, whereas in the softening stage the shortening of the whole specimen is assumed to be coincident

with the stroke of the loading machine. In addition, the main parameters of the $\sigma_{lc} - \varepsilon_{lc}$ curves are collected in Table 7.3.

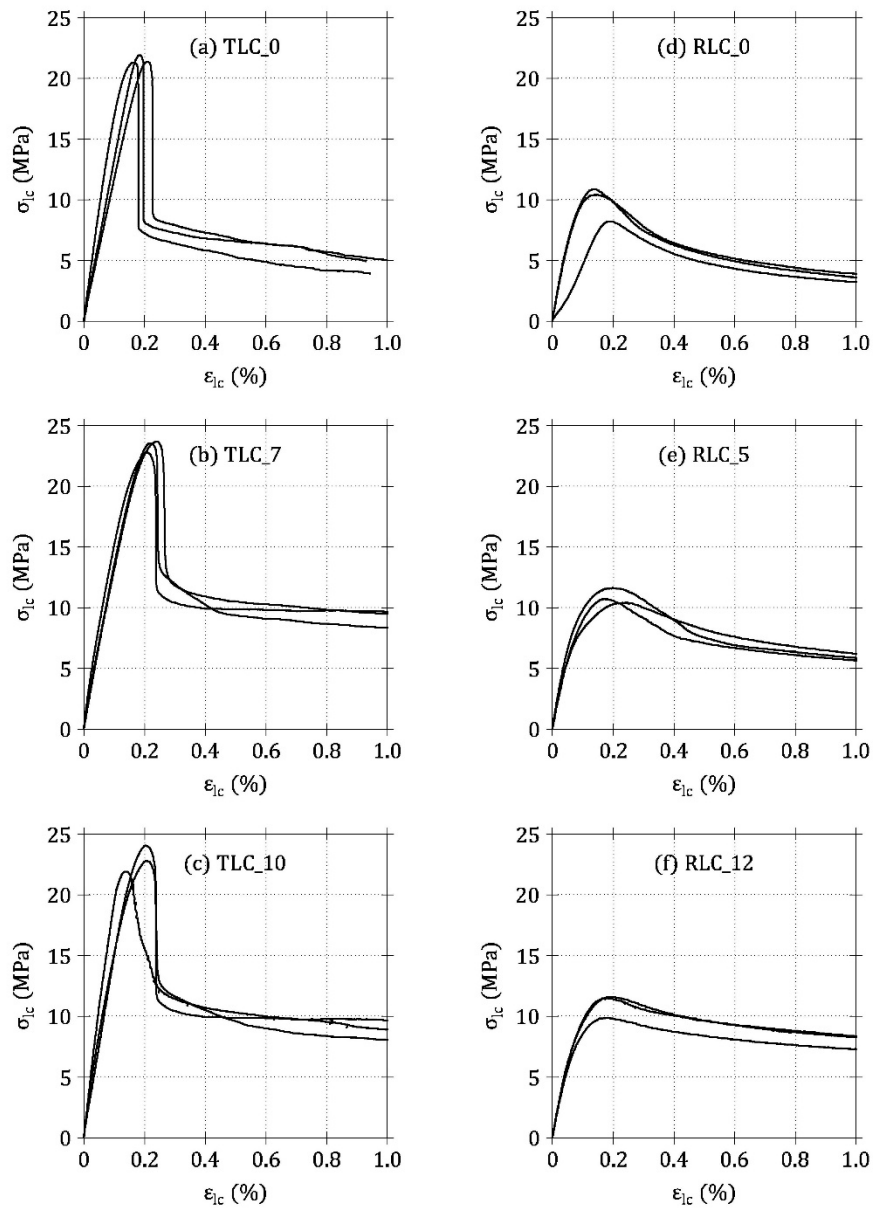


Figure 7.2: Stress vs. strain curves obtained from uniaxial compression tests: (a)-(c) TLC mixtures; (d)-(f) RLC mixtures.

Table 7.3: Average values of the concrete parameters obtained with the uniaxial compression tests.

Specimens	f_{lc} (MPa)	E_{lc} (MPa)	ε_{lc1} (‰)	k_{lc}
TLC_0	21.51	15070	1.8	1.3
TLC_7	23.36	15619	2.2	1.5
TLC_10	22.91	18868	1.8	1.5
RLC_0	9.84	12326	1.6	1.8
RLC_5	10.94	15667	2.0	2.9
RLC_12	10.99	15607	1.9	2.7

The parameters of Table 7.3 include the average compressive strength f_{lc} (i.e., the peak of the $\sigma_{lc} - \varepsilon_{lc}$ curves), the tangent modulus of elasticity E_{lc} (in the origin of the $\sigma_{lc} - \varepsilon_{lc}$ curves), the strain at the peak of stress ε_{lc1} , and the plasticity number $k_{lc} = E_{lc} / E_{lc1}$ (i.e., the ratio between E_{lc} and the secant modulus from the origin to the peak of stress $E_{lc1} = f_{lc} / \varepsilon_{lc1}$). The maximum strength experimentally measured is close to the strength class LC12 ($f_{lc} = 20$ MPa) defined by Model Code 2010 (*fib* 2012a), which also specify that LC8 ($f_{lc} = 16$ MPa) is the minimum concrete grade for structural applications. Accordingly, RLC mixtures cannot be used in structural applications (Table 7.3), especially in compressed elements.

In both the lightweight mixtures under investigation, the presence of fibers does not alter neither the maximum stress nor the deformability of the pre-peak stage of the stress-strain curves (Table 7.3 and Figure 7.2). Conversely, for the same type of concrete [i.e., TLC in Figure 7.2(a-c) and RLC in Figure 7.2(d-f)], the ductility of the post-peak branches (i.e., the area under the $\sigma_{lc} - \varepsilon_{lc}$ curves) increases with the fiber content. In other words, the confinement effect produced by the fiber-reinforcement in normal weight concrete under compression (Fantilli et al. 2011), also occurs in lightweight concrete made with rubber or expanded clay aggregates.

The values of E_{lc} , ε_{lc1} , and k_{lc} experimentally obtained for TLC mixtures (Table 7.3) are in good agreement with the estimations of Model Code 2010 (*fib* 2012a) for a lightweight concrete LC12 (i.e., $E_{lc} = 15,237$ MPa, $\varepsilon_{lc1} = 2.02$ ‰, and $k_{lc} = 1.3$). On the other hand, the parameters obtained in Table 7.3 for RLC mixtures substantially differ from the values suggested by Model Code 2010 (*fib* 2012a), even in the case of the minimum concrete grade LC8 (i.e., $E_{lc} = 18,756$ MPa, $\varepsilon_{lc1} = 1.33$ ‰, and $k_{lc} = 1.3$). Such differences can be ascribed to the type of

aggregates. Although rubber (having density = 900 kg/m^3) is more dense than expanded clay (density = 380 kg/m^3), the latter exhibits lower deformability.

7.3.2 Three point bending tests

The results of the bending tests on one-way plates are reported in Figure 7.3, where the load P vs. midspan deflection δ curves are depicted. In all the tests, the effective cracking load P_{cr^*} , at which the softening stage begins, is clearly evident. In the case of unreinforced plates [i.e., TLC_0 and RLC_0 in Figure 7.3(a) and Figure 7.3(d), respectively], P_{cr^*} is the absolute maximum. On the other hand, the P - δ curves of fiber-reinforced plates show two relative maximums [Figure 7.3(b-c) for TLC, and Figure 7.3(e-f) for RLC]. The first coincides with P_{cr^*} , and the second, at the onset of strain localization, is the ultimate load P_u . All these values are reported in Table 7.4. For each plate, P_{cr^*} is remarkably higher than the maximum design load $P_d = 8.60 \text{ kN}$. Such a value is obtained by factorizing the dead loads (equal to 2.0 kN/m^2) and the variable load (4.0 kN/m^2) with the partial safety factors $\gamma_G = 1.3$ and $\gamma_Q = 1.5$, respectively (*fib* 2012a).

The brittle behavior of unreinforced lightweight concrete can be observed in Figure 7.3, where the P - δ curves show a sharp drop after the peak, especially in TLC_0 plates of Figure 7.3(a). On the contrary, in the softening stage of RLC_0 plates [Figure 7.3(d)], residual loads can be detected also for large δ . If the plastic fibers are added to the cementitious matrix, the residual loads increase for both the lightweight mixtures. In particular, P_u grows with the fiber content [Figure 7.3(b-c) for TLC, and Figure 7.3(e-f) for RLC], whereas P_{cr^*} is nearly constant (Table 7.4). In some cases [i.e., the plates TLC_10 in Figure 7.3(c) and RLC_12 in Figure 7.3(f)], a very ductile response, with $P_u \cong P_{cr^*}$, can be observed.

Table 7.4: Average values of the structural parameters obtained with the three point bending tests on one-way plates.

Plates	P_{cr^*} (kN)	P_u (kN)	DI	SR
TLC_0	16.01	/	/	0.10
TLC_7	22.32	17.95	-0.20	0.13
TLC_10	21.59	22.93	0.06	0.13
RLC_0	20.24	/	/	0.28
RLC_5	20.96	15.84	-0.24	0.26
RLC_12	20.46	19.27	-0.06	0.25

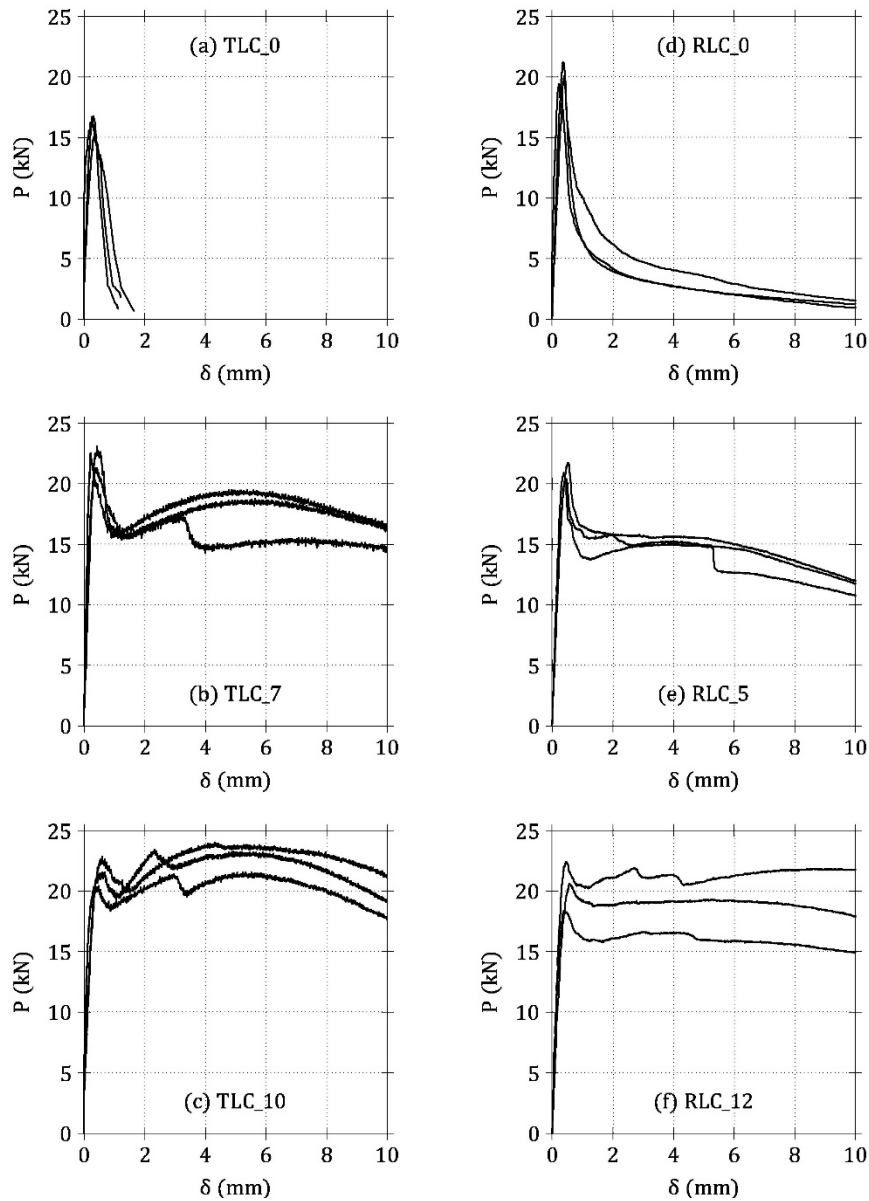


Figure 7.3: Load-deflection curves obtained from the three point bending tests: (a)-(c) TLC plates; (d)-(f) RLC plates.

Referring to the fiber-reinforced plates (i.e., TLC_7, TLC_10, RLC_5 and RLC_12), the brittle/ductile behavior can be assessed by means of the proposed approach. Hence, the average values of DI are computed with Eq.(1.6) and reported in Table 7.4. According to the results of Chapter 3, a linear increment of the ductility index with the fiber volume fraction is assumed for both TLC and RLC plates, as illustrated in Figure 7.4(a) and Figure 7.4(b), respectively.

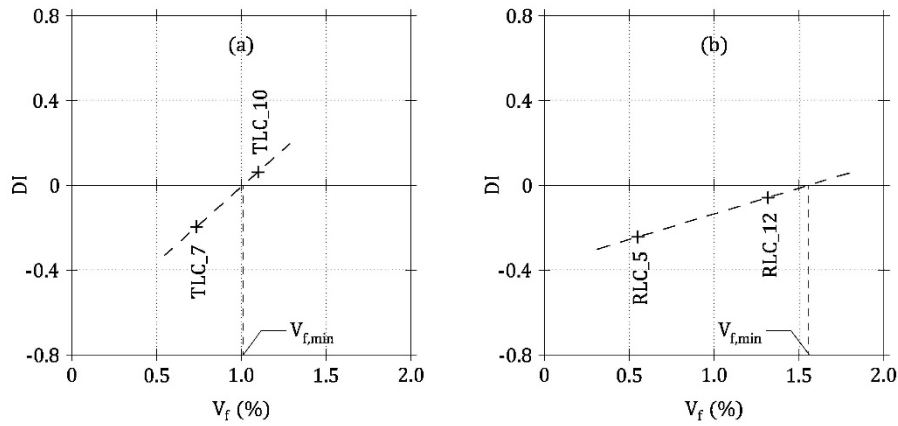


Figure 7.4: Average values of ductility index as a function of the amount of fibers and evaluation of the minimum fiber volume fraction: (a) TLC plates; (b) RLC plates.

Therefore, the minimum amount of fibers $V_{f,min}$ can be easily individuated at the brittle/ductile transition. As a result, a value $V_{f,min} = 1.01$ % is determined for TLC [Figure 7.4(a)], whereas a fiber content of 1.56 % in volume is necessary to attain the ductility in RLC plates [Figure 7.4(b)].

7.4 Comparative analyses

7.4.1 Analysis at the material level

As reported in Table 7.3, the value of f_{ic} experimentally measured in RLC specimens is about one half of the compressive strength referred to TLC. This is due to the different water/cement ratio between Table 7.1 and Table 7.2, and also to the different aggregate/cement paste interaction in the two mixtures (Ganjian and Khorami 2009). However, it is worth noting the large ductility showed by RLC, which is remarkably higher than that of TLC. Indeed, with respect to the compressive strength, higher values of residual stress can be observed in the $\sigma_{lc} - \varepsilon_{lc}$ curves of Figure 7.2(d-f) (i.e., in RLC), rather than in Figure 7.2(a-c) (i.e., in TLC). Thus, it can be argued that the rubber aggregates exert a sort of passive confinement in compression, which is not evident in the presence of expanded clay aggregates (Fantilli et al. 2016e). Obviously, the fracture toughness increases with the fiber content in both TLC and RLC mixtures.

7.4.2 Analysis at the structural level

Despite the lower compressive strength, RLC plates behaves in bending similarly to those made of TLC (Figure 7.3). Thus, the mechanical properties of TLC and RLC elements subjected to bending actions are not related in the same manner to the compressive strength. The values of P_{cr^*} , higher in RLC_0 than in TLC_0 plates (Table 7.4), generally increase when fibers are added to an ordinary concrete matrix (Naaman 2003). This further corroborates the conjecture that rubber aggregates contribute to increase concrete toughness, similarly to the presence of fibers (Fantilli et al. 2016e).

To quantify the beneficial effect of rubber, the flexural tensile strength $f_{lct,fl}$ of both the lightweight concretes can be elastically evaluated from the bending tests on plates. In this way, a direct comparison with the corresponding compressive strength can be performed by introducing the following strength ratio (SR):

$$SR = \frac{f_{lct,fl}}{f_c} = \frac{M_{cr^*}}{W} \cdot \frac{1}{f_c} \quad (7.1)$$

where $M_{cr^*} = P_{cr^*} \cdot L/4 =$ effective cracking moment in midsection [$L = 900$ mm in Figure 7.1(b)]; and $W = B \cdot H^2/6 =$ section modulus of the plate [$B = 1,000$ mm, and $H = 100$ mm in Figure 7.1(b)].

The average values of SR , computed according to Eq.(7.1), are reported in Table 7.4. The positive contribution of rubber aggregates to the flexural strength of lightweight concrete is particularly evident in such Table. Indeed, the values of SR referred to TLC plates are about the double of those of RLC plates. More precisely, $SR = 10 - 13 \%$ is obtained in TLC, and $SR = 25 - 28 \%$ in RLC (Table 7.4). This is due to the effect given by the rubber granulates, which seems to be macroscopically similar to the bridging action exerted by fibers crossing the crack surfaces (Fantilli et al. 2016e).

7.4.3 Combined ecological and mechanical assessment

By introducing the so-called ecological index (EI) and mechanical index (MI), a more comprehensive comparative analysis, including the environmental impact of the two lightweight mixtures, can be performed (Fantilli and Chiaia 2013c). The following equation estimates EI by combining the amount of the released carbon

dioxide (i.e., CF = carbon footprint) and the energy used in the product life-cycle (i.e., EE = embodied energy):

$$EI = CF \cdot EE \quad (7.2)$$

Both CF and EE are measured herein only for the most relevant concrete components, such as cement, lightweight aggregate (made with expanded clay or grained rubber from end-of-life tires) and polypropylene fibers. Superplasticizer is not considered in the computation of EI , because of the small amounts indicated in Table 7.1 and Table 7.2, with respect to the other components of TLC and RLC mixtures. Table 7.5 collects all the data necessary to compute EI in accordance with Eq.(7.1) (Ashby 2009, Ecopneus 2013, *fib* 2012b, Swiss Centre for Life Cycle Inventories 2012).

It must be remarked that Eq.(7.2) takes into account environmental aspects in a simple way. To carry out more complete sustainability analyses, including social and economic issues, other methods can be found in the literature (e.g., Aguado et al. 2016).

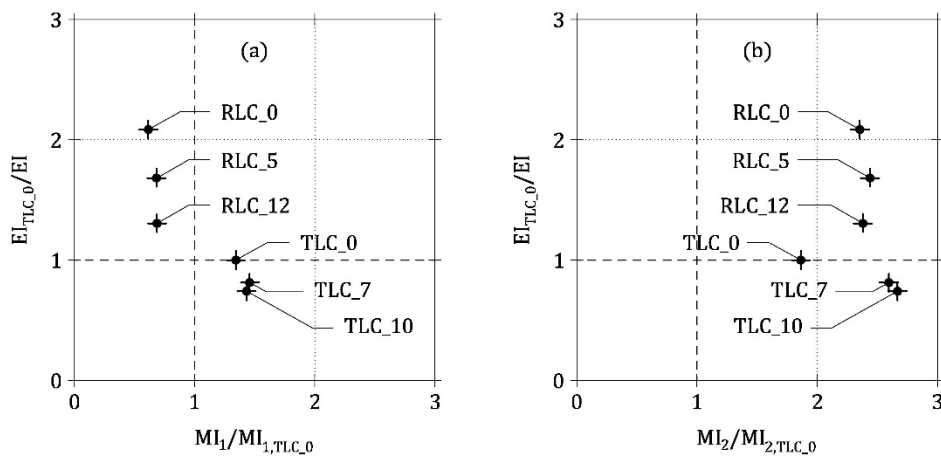
As the mechanical index can be related to different functional units, three analyses are carried out herein by assuming $MI_1 = f_{ic}$ at the material level, as well as $MI_2 = P_{\max} = \max(P_{cr*}; P_u)$ and $MI_3 = DI$ at the structural level (Table 7.6). In the first two cases, the ecological index of TLC_0 (Table 7.6) is used as the upper bound value of the environmental performances (EI_{TLC_0}), in the absence of specific rules. Conversely, the lower bound values of the mechanical index are assumed to be $MI_{1,TLC_0} = 16$ MPa [i.e., the minimum compressive strength for structural applications recommended by Model Code 2010 (*fib* 2012a)] and $MI_{2,TLC_0} = P_d = 8.60$ kN (i.e., the design load of the plates). Referred to these bounds, two combined ecological and mechanical analyses can be carried out for all the mixtures by means of the non-dimensional diagrams depicted in Figure 7.5 (Fantilli and Chiaia 2013c).

Table 7.5: Environmental impact referred to 1 kg of concrete components.

Component	CF (kg CO ₂)	EE (MJ)
Cement	0.8	5
Expanded clay aggregate	0.3	4
Rubber granulates	0.2	4
Polypropylene fibers	2.7	100

Table 7.6: Ecological and mechanical indexes of the six lightweight concretes.

Mixture	EI (kg CO2 GJ / m ³)	MI_1 (MPa)	MI_2 (kN)
TLC_0	1803	21.51	16.01
TLC_7	2219	23.36	22.32
TLC_10	2432	22.91	22.93
RLC_0	865	9.84	20.24
RLC_5	1070	10.94	20.96
RLC_12	1379	10.99	20.46

Figure 7.5: Results of combined ecological and mechanical analyses of TLC and RLC: (a) at material scale with $MI = MI_1$; (b) at structural scale with $MI = MI_2$.

With respect to $MI_1 = f_{ic}$, neither TLC nor RLC mixtures contemporarily fulfil the mechanical and environmental requirements [Figure 7.5(a)]. As a matter of fact, fiber-reinforced traditional lightweight concretes satisfy the mechanical condition $MI > MI_{1,TLC_0}$, but $EI > EI_{TLC_0}$ due to the environmental impact of fibers. Conversely, RLC only fits the ecological performances (with and without the fibers), but it does not achieve the minimum strength required for structural use (*fib* 2012a).

When $MI_2 = P_{max}$ [Figure 7.5(b)] TLC only meets the mechanical requirement (i.e., $MI > MI_{2,TLC_0}$), whereas both $EI < EI_{TLC_0}$ and $MI > MI_{2,TLC_0}$ are satisfied by all the rubber lightweight concretes investigated in this Chapter. Among them, RLC_0 seems to be the best cement-based composite to be used in one-way plates. Indeed, EI increases in presence of fibers, as it can be observed for RLC_5 and RLC_12 in Table 7.6, whereas the values of P_{max} are nearly the same for all the RLC plates (Table 7.4).

Nevertheless, the brittle behavior of RLC_0 plates [Figure 7.3(d)] cannot be accepted for structural applications (ACI 2014, CEN 2004a, *fib* 2012a), and a minimum ductility is required (i.e., $DI \geq 0$ according to the proposed approach). Therefore, the third comparative analysis involves the ideal TLC and RLC plates containing the minimum fiber volume fractions $V_{f,\min}$ previously evaluated in Figure 7.4(a) and Figure 7.4(b), respectively. They correspond to 9.2 kg/m^3 for TLC, and to 14.2 kg/m^3 for RLC. Under these conditions, the performances of the plates are only compared in terms of EI , because $MI_3 = DI = 0$ in both the cases. As a result, RLC (which shows $EI = 1493 \text{ kgCO}_2 \text{ GJ/m}^3$) should be preferred to TLC (with $EI = 2380 \text{ kgCO}_2 \text{ GJ/m}^3$) when the minimum amount of fibers is added to the mixtures. Finally, it should be remarked that the combined ecological and mechanical performances of concrete containing rubber aggregates are better than those of TLC also referring to the strength of the plates [Figure 7.5(b)].

7.5 Discussion of the results

When a comparative analysis between concrete mixtures is based on both ecological and mechanical performances, the results depend on the adopted functional unit. Specifically, in the case of the lightweight composites previously investigated, if the compressive strength (i.e., a material property) is used as the reference performance, RLC fits the proposed ecological requirements both with and without the fibers, but it does not achieve the minimum strength for structural applications (*fib* 2012a), especially in compressed elements.

On the contrary, if the analyses are referred to structural parameters, such as the maximum load or the ductility index of plates in bending, the substitution of expanded clay aggregates with rubber granulates appears to be convenient. In any case, the ductility index seems to be the more appropriate parameter for describing the mechanical performances of lightly reinforced members in bending, as it takes into account both the flexural strength, in M_{cr^*} , and the presence of fibers in the concrete, in M_u .

Finally, the above-mentioned differences suggest the necessity to properly define the functional unit to which the inputs and outputs of a life-cycle assessment must be referred, and the ecological benchmarks of concrete structures as well.

Chapter 8

Conclusions

8.1 Final considerations

In the previous Chapters, the flexural behavior of concrete members containing low amounts of rebar, fibers, or a combination, is analyzed in order to identify the brittle/ductile transition (i.e., the minimum reinforcement) by means of a new and unified approach. Numerical results obtained through general models and several experimental data are considered. To show the potentialities of the proposed approach, the latter is adopted in a structural application and in a simplified sustainability assessment. Based on the results of the above-mentioned numerical and experimental analyses, the following conclusions can be drawn.

1. Similar behaviors are observed for LRC, FRC and HRC members subjected to static bending actions. In all the cases, the brittle/ductile response can be evaluated through the ductility index DI , which is proportional to the difference between the ultimate bending moment M_u and the effective cracking moment M_{cr*} [Eq.(1.6)]. Therefore, as the brittle/ductile transition occurs when M_u equates M_{cr*} , the minimum reinforcement for static reasons (e.g., the minimum area of rebar $A_{s,min}$ in LRC beams, but also the minimum fiber volume fraction $V_{f,min}$ in FRC members) can be computed by imposing $DI = 0$.
2. If DI is assumed to linearly increase with the amount of reinforcement (rebar and/or fibers) [i.e., Eq.(1.7)], the corresponding slope ζ can be

estimated by means of a simplified formulae of M_u and M_{cr*} [i.e., Eq.(1.8)]. In a concrete beam, the amount of rebar and/or fibers can be expressed by the normalized reinforcement ratio $r = A_s/A_{s,min} + V_f/V_{f,min}$, i.e., a linear combination of the area of rebar A_s and of the fiber volume fraction V_f , normalized with respect to the corresponding minimum amounts, respectively. As a first approximation, the linear increment of DI on r is described by Eq.(2.4) for LRC beams (where $\zeta = 1$), and by Eq.(3.4) for FRC members (where $\zeta = 0.7$). Conversely, in the case of HRC elements, Eqs.(4.4) define a $DI-r$ envelope which is bordered by Eq.(2.4) and Eq.(3.4).

3. The numerical results of general models able to predict the flexural response of LRC, FRC and HRC ideal beams confirm that the values of DI linearly increase with the reinforcement ratio. To be more precise, 36 LRC members, 54 FRC members, and 108 HRC members having different geometrical and mechanical properties are analyzed. Moreover, 50 LRC beams, 61 FRC beams, and 25 HRC beams tested in some experimental campaigns corroborate the existence of the linear trend, which is generally valid, regardless of the geometrical size, and the mechanical properties of materials as well. This is due to the use of normalized variables (i.e., DI and r), in which the parameters affecting the brittle/ductile behavior of concrete members (e.g., concrete strength, rebar and fiber properties, beam size, etc.) are included in both numerator and denominator. Therefore, the linearity of the $DI-r$ relationships is not influenced by such parameters.
4. The $DI-r$ relationships separately valid for LRC, FRC, and HRC members can be superposed, and a unique envelope can be obtained. Specifically, Eqs.(5.1) are the upper bound relationships, which can be adapted to the safety format of building codes (ACI 2014, CEN 2004a, *fib* 2012a) [Eqs.(5.5)]. Therefore, a unified design-by-testing procedure for evaluating the minimum reinforcement of a concrete member can be proposed. It requires to perform few full-scale tests on LRC and/or FRC elements containing trial amounts of rebar or fibers, respectively. Then, Eqs.(5.4) [or Eqs.(5.6) for taking into account the structural safety] can be used to estimate $A_{s,min}$ and $V_{f,min}$, and the procedure can also be iterated for obtaining more precise values (Figure 6.10). In HRC members, the minimum reinforcement is defined by any linear combination of $A_{s,min}$ and $V_{f,min}$ [i.e., Eq.(4.5)]. Anyway, few tests on full-scale concrete beams are

always necessary, as the problem of the transition between the laboratory scale and the structural scale has not been completely solved until now (Grünewald et al. 2014). This made the proposed approach suitable for applications in the precast concrete industry, especially for the design of massive structural elements.

5. A unique linear relationship can be used to approximate the $DI-r$ envelope of all the LRC, FRC, and HRC members [i.e., Eq.(5.2) having $\zeta = 0.8$]. With a simple substitution, such relationship defines an inclined plane in the $DI-A_s/A_{s,min} - V_f/V_{f,min}$ space [i.e., Eq.(5.3)], which provides a three-dimensional interpretation to the proposed unified approach. To be more precise, the inclined plane represents the variation of DI with the amount of reinforcement, and its interception with the horizontal surface $DI=0$ corresponds to the condition of the brittle/ductile transition [i.e., Eq.(4.5)]. Moreover, the two interceptions of the proposed plane with the surfaces $V_f/V_{f,min} = 0$ and $A_s/A_{s,min} = 0$ are the $DI-r$ linear relationships for LRC and FRC beams, if a unique slope $\zeta = 0.8$ is assumed. The inclined plane described by Eq.(5.3) well approximates the results of both the 198 ideal beams and the 136 bending tests taken into account herein.
6. The proposed approach is successfully applied to design the minimum reinforcement of concrete segments for the lining of Brenner Base Tunnel (Caratelli et al. 2011). Indeed, the use of the general models for LRC and FRC members, and of Eqs.(5.4) as well, allows to identify $A_{s,min}$ and $V_{f,min}$. By combining those values, several flexural responses at brittle/ductile transitions can be obtained with the general model for HRC members. In addition, the behavior of such HRC segments is equivalent not only in pure flexure (i.e., in the transitory stages) but also under combined axial force and positive bending moment (i.e., in service conditions). Thus, the amounts of rebar and fibers can be designed to optimize the total manufacture cost and the workability of the concrete mixtures.
7. The ductility index can also be used to measure the combined ecological and mechanical performances of one-way plates in bending, realized with different fiber-reinforced lightweight concretes. In the specific case, a mixture containing expanded clay aggregates (TLC), and a non-conventional concrete with grinded rubber in partial substitution of the stone aggregates (RLC), are analyzed. Due to the remarkably different compositions of the mixtures, their mechanical performances are in turn

deeply discordant. Accordingly, if a combined ecological and mechanical analysis is performed, the results depend on the functional unit used to compare the concrete members. Based on the findings of the previous comparative analyses on concrete plates subjected to bending actions, the use of structural parameters as functional unit seems to be the more reasonable solution. Moreover, when such parameter is the ductility index, both the flexural strength of the concrete cross-section (i.e., M_{cr^*}) and the presence of reinforcement (i.e., M_u) are taken into account.

8. As a result, the ductility index herein introduced for describing the brittle/ductile behavior of concrete members containing low amounts of rebar and/or fibers, can also be adopted as functional unit of simplified sustainability analyses. This design strategy is in good agreement with the integrated approach which should be adopted to obtain more resilient and sustainable concrete structures (Bocchini et al. 2014).

8.2 Further researches

The results of the present thesis provide some suggestions for possible future researches. In addition, similar topics not considered herein could be dealt with in other studies.

1. The present design-by-testing approach for the evaluation of the minimum reinforcement for static reasons could be adapted to the safety format of the main building codes used in the design of reinforced concrete members (ACI 2014, CEN 2004a, *fib* 2012a). At this aim, it should be necessary to perform a probabilistic analysis of the experimental results available in the current literature, already considered in the previous Chapters, but also on new and specific experimental campaigns performed on concrete elements reinforced with low amounts of rebar and/or fibers.
2. The non-dimensional approach presented herein could also be applied to the maximum reinforcement for avoiding the concrete crushing (CEN 2004a) and to the minimum reinforcement for crack control, which is necessary in presence of steel rebar embedded in the cementitious matrix (i.e., in LRC and HRC members).
3. Since in this thesis only statically determined structural elements are considered, further theoretical and experimental studies should be devoted

to the extension of the proposed approach to the evaluation of the brittle/ductile flexural response of other concrete structures (e.g., two-way slabs, frames, etc.).

4. As different results related to the possible use of several functional units can be obtained in a combined ecological and mechanical analysis, it would be desirable to univocally define this parameter, as well as the bound values of the environmental performances showed by concrete structures.

References

Aguado, A., Gálvez, J. C., Fernández-Ordóñez, D., de la Fuente, A., 2016. Sustainability evaluation of the concrete structures. In: Proceedings of the 2nd International Conference on Concrete Sustainability ICCS16, Madrid (Spain), pp. 58-71.

Alberti, M.G., Enfedaque, A., Gálvez, J.C., 2014a. On the mechanical properties and fracture behavior of polyolefin fiber-reinforced self-compacting concrete. *Construction and Building Materials* 55, 274-288.

Alberti, M.G., Enfedaque, A., Gálvez, J.C., Cánovas, M.F., Osorio, I.R., 2014b. Polyolefin fiber-reinforced concrete enhanced with steel-hooked fibers in low proportions. *Materials and Design* 60, 57-65.

Alonso, C., Andrade, C., Rodriguez, J., Diez, J.M., 1998. Factors controlling cracking of concrete affected by reinforcement corrosion. *Materials and Structures* 31(7), 435-441.

American Concrete Institute (ACI), 2003. *Guide for Structural Lightweight-Aggregate Concrete*. ACI, Farmington Hills, Michigan (USA).

American Concrete Institute (ACI), 2014. 318-14: *Building Code Requirements for Structural Concrete and Commentary*. ACI, Farmington Hills, Michigan (USA).

American Concrete Institute (ACI), 2016. *Sustainability & Resilience – Concrete International* 38(11). ACI, Farmington Hills, Michigan (USA).

American Society for Testing and Materials (ASTM), 2010. *ASTM C1550-10: Standard Test Method for Flexural Toughness of Fiber Reinforced Concrete (Using Centrally Loaded Round Panel)*. In: *Annual Book of ASTM Standards*. ASTM International, West Conshohocken, Pennsylvania (USA).

- Armelin, H.S., Banthia, N., 1997. Predicting the Flexural Postcracking Performance of Steel Fiber Reinforced Concrete from the Pullout of Single Fibers. *ACI Materials Journal* 94 (1), 18-31.
- Ashby, M.F., 2009. *Materials and the Environment: Eco-Informed Materials Choice*. Butterworth-Heinemann (Elsevier), Burlington, Massachusetts (USA).
- Aydin, S., 2013. Effects of fiber strength on fracture characteristics of normal and high strength concrete. *Periodica Polytechnica - Civil Engineering* 57(2), 191-200.
- Balaguru, N., Shah, S.P., 1992. *Fiber-reinforced cement composites*. McGraw-Hill, New York (USA).
- Banthia, N., Gupta, R., 2004. Hybrid fiber reinforced concrete (HyFRC): fiber synergy in high strength matrices. *Materials and Structures* 37, 707-716.
- Barros, J.A.O., Cunha, V.M.C.F., Ribeiro, A.F., Antunes, J.A.B., 2005. Post-cracking behaviour of steel fibre reinforced concrete. *Materials and Structures* 38, 47-56.
- Barros, J.A.O., Figueiras, J.A., 1998. Experimental behaviour of fibre concrete slabs on soil. *Mechanics of Cohesive-Frictional Materials* 3, 277-290.
- Barros, J.A.O., Santos, S.P.F., Lourenço, L., Gonçalves, D., 2008. Flexural behaviour of steel fibre reinforced self-compacting concrete laminar structures. In: *Proceedings of the 1st Spanish Congress on Self-Compacting Concrete HAC 2008, Valencia (Spain)*, 567-578.
- Barros, J.A.O., Taheri, M., Salehian, H., 2015. A model to simulate the moment-rotation and crack width of FRC members reinforced with longitudinal bars. *Engineering Structures* 100, 43-56.
- Bayasi, M.Z., Soroushian, P., 1992. Effect of steel fiber reinforcement on fresh mix properties of concrete. *ACI Materials Journal* 89, 369-374.
- Bažant, Z.P., Cedolin, L., 1991. *Stability of Structures: Elastic, Inelastic, Fracture and Damage Theories*. Oxford University Press, New York (USA).
- Bažant, Z.P., Planas, J., 1998. *Fracture and Size Effect in Concrete and Other Quasibrittle Materials*. CRC Press, Boca Raton (USA).

- Beeby, A.W., 2004. The influence of the parameter ϕ/ρ_{eff} on crack widths. *Structural Concrete* 5(2), 71-83.
- Beeby, A.W., 2005. Discussion – The influence of the parameter ϕ/ρ_{eff} on crack widths. *Structural Concrete* 6(4), 155-165.
- Bentur, A., Mindess, S., 1990. *Fibre Reinforced Cementitious Composites*. Elsevier Applied Science, London (UK).
- Blanco, A., Pujadas, P., de la Fuente, A., Cavalaro, S., Aguado, A., 2013. Application of constitutive models in European codes to RC-FRC. *Construction and Building Materials* 40, 246-259.
- Bocchini, P., Frangopol, D., Ummenhofer, T., Zinke, T., 2014. Resilience and Sustainability of Civil Infrastructure: Toward a Unified Approach. *ASCE Journal of Infrastructure Systems* 20(2),
- Borosnyói, A., Balázs, G.L., 2005. Models for flexural cracking in concrete: the state of the art. *Structural Concrete* 6(2), 53-62.
- Bosco, C., Carpinteri, A., Debernardi, P.G., 1990. Minimum reinforcement in high-strength concrete. *ASCE Journal of Structural Engineering* 116(2), 427-437.
- Brandt, A.M., 2008. Fibre reinforced cement-based (FRC) composites after over 40 years of development in building and civil engineering. *Composite Structures* 86, 3-9.
- Brincker, R., Henriksen, M.S., Christensen, F.A., Heshe, G., 1999. Size effects on the bending behaviour of reinforced concrete beams. *European Structural Integrity Society* 24, 127-180.
- Burgers, R., Walraven, J., Plizzari, G.A., Tiberti, G., 2007. Structural behavior of SFRC tunnel segments during TBM operations. In: *Underground Space - the 4th Dimension of Metropolises – Proceedings of the World Tunnel Congress ITA-AITES 2007, Prague (Czech Republic)*, 1461- 1467.
- Caratelli, A., Meda, A., Rinaldi, Z., Romualdi, P., 2011. Structural behaviour of precast tunnel segments in fiber reinforced concrete. *Tunnelling and Underground Space Technology* 26, 284-291.

- Caratelli, A., Meda, A., Rinaldi, Z., 2012. Design according to MC2010 of a fibre-reinforced concrete tunnel in Monte Lirio, Panama. *Structural Concrete* 13, 166-173.
- Carpinteri, A., 1989. Minimum reinforcement in reinforced concrete beams. In: RILEM TC 90-FMA, Code Work, Cardiff (UK).
- Carpinteri, A., Cadamuro, E., Corrado, M., 2014. Minimum flexural reinforcement in rectangular and T-section concrete beams. *Structural Concrete* 15(3), 361-372.
- Carpinteri, A., Cadamuro, E., Ventura G., 2015. Fiber-reinforced concrete in flexure: a cohesive/overlapping crack model application. *Materials and Structures* 48, 235-247.
- Carpinteri, A., Cornetti, P., 2002. Size effects on concrete tensile fracture properties: an interpretation of the fractal approach based on the aggregate grading. *Journal of the Mechanical Behavior of Materials*, 13(3/4), 233-246.
- Carpinteri, A., Ferro, G., Bosco, C., Elkatieb, M., 1999. Scale effects and transitional failure phenomena of reinforced concrete beams in flexure. *European Structural Integrity Society* 24, 1-30.
- Chiaia, B., Fantilli, A.P., Vallini, P., 2007. Evaluation of minimum reinforcement ratio in FRC members and application to tunnel linings. *Materials and Structures* 40, 593-604.
- Chiaia, B., Fantilli, A.P., Vallini, P., 2009. Combining fiber-reinforced concrete with traditional reinforcement in tunnel linings. *Engineering Structures* 31, 1600-1606.
- Damineli, B.L., Kemeid, F.M., Aguiar, P.S., John, V.M., 2010. Measuring the eco-efficiency of cement use. *Cement and Concrete Composites* 32, 555-562.
- Dancygier, A.N., Berkover, E., 2012. Effect of steel fibers on the flexural ductility of lightly reinforced concrete beams. In: *Innovative Materials and Techniques in Concrete Construction*, Springer, Dordrecht (The Netherlands), 197-207.
- de Borst, R., 2002. Fracture in quasi-brittle materials: a review of continuum damage-based approaches. *Engineering fracture mechanics* 69(2), 95-112.

- de la Fuente, A., Escariz, R.C., de Figueiredo, A.D., Aguado, A., 2013. Design of macro-synthetic fibre reinforced concrete pipes. *Construction and Building Materials* 43, 523-532.
- de la Fuente, A., Pujadas, P., Blanco, A., Aguado, A., 2012. Experiences in Barcelona with the use of fibres in segmental linings. *Tunnelling and Underground Space Technology* 27, 60-71.
- de Montaignac, R., Massicotte, B., Charron, J.P., 2012. Design of SFRC structural elements: flexural behaviour prediction. *Materials and Structures* 45, 623-636.
- de Saint-Venant, A.J.C.B., 1856. Mémoire sur la flexion des prismes. *Journal de Mathématiques de Liouville* 1, 89-189.
- di Prisco, M., Colombo, M., 2012. FRC thin walled structures: opportunities and threats. In: *Proceedings of the 8th RILEM International Symposium on Fiber Reinforced Concrete: challenges and opportunities*, Guimarães (Portugal), 23-49.
- di Prisco, M., Colombo, M., Bonalumi, P., Beltrami, C., 2014. FRC structural applications according to the fib Model Code 2010: A unified approach. In: *Proceedings of the FRC 2014 Joint ACI-fib International Workshop*, Montreal (Canada), 224-234.
- di Prisco, M., Colombo, M., De Wilder, K., Vandewalle, L., 2016. A new FRC solution for a partially prefabricated industrial deck. In: *Proceedings of the 9th RILEM International Symposium on Fiber Reinforced Concrete BEFIB 2016*, Vancouver (Canada), 1407-1421.
- di Prisco, M., di Prisco, C., Dozio, D., Galli, A., Lapolla, S., 2008. Assessment and control of a SFRC retaining structure: mechanical issues. In: *On site assessment of concrete, masonry and timber structures - Proceedings of the International RILEM Symposium On Site Assessment of Concrete, Masonry and Timber Structures SACoMaTiS 2008*, Varenna (Italy), 593-604.
- di Prisco, M., Plizzari, G., Vandewalle, L., 2009. Fibre reinforced concrete: new design perspectives. *Materials and Structures* 42, 1261-1281.
- Dupont, D., 2003. Modelling and experimental validation of the constitutive law (σ - ε) and cracking behaviour of fibre reinforced concrete. Ph.D. Thesis, Katholieke Universiteit Leuven (Belgium).

Ecopneus, 2013. Ecopneus in the Green economy – Sustainability Report 2013. Available from: <<http://www.ecopneus.it/>>.

Elrakib, T.M., 2013. Performance evaluation of HSC beams with low flexural reinforcement. *HBRC Journal* 9, 49-59.

European Committee for Concrete (CEB), 1998. CEB Bulletin 242: Ductility of Reinforced Concrete Structures. CEB, Lausanne (Switzerland).

European Committee for Standardization (CEN), 2004a. EN 1992-1-1: Eurocode 2: Design of Concrete Structures - Part 1-1: General Rules and Rules for Buildings. CEN, Brussels (Belgium).

European Committee for Standardization (CEN), 2004b. EN 1998-1: Eurocode 8: Design of structures for earthquake resistance - Part 1: General rules, seismic actions and rules for buildings. CEN, Brussels (Belgium).

European Committee for Standardization (CEN), 2007. EN 14651: Test method for metallic fibre concrete - Measuring the flexural tensile strength (limit of proportionality (LOP), residual). CEN, Brussels (Belgium).

European Committee for Standardization (CEN), 2010. CEN/TS 14243: Materials produced from end of life tyres - Specification of categories based on their dimension(s) and impurities and methods for determining their dimension(s) and impurities. CEN, Brussels (Belgium).

Faconi, L., Minelli, F., 2017. Verification of structural elements made of FRC only: A critical discussion and proposal of a novel analytical method. *Engineering Structures* 131, 530-541.

Faconi, L., Minelli, F., Plizzari, G., 2016. Steel fiber reinforced self-compacting concrete thin slabs – Experimental study and verification against Model Code 2010 provisions. *Engineering Structures* 122, 226-237.

Falkner, H., Henke, V., 2005. Steel fibre reinforced concrete, from research to standards. *Concrete Structures - Annual Technical Journal - Hungarian Group of fib* 6, 39-46.

Fantilli, A.P., Cavallo, A.D., Pistone, G., 2015. Fiber-reinforced lightweight concrete slabs for the maintenance of the Soleri Viaduct. *Engineering Structures* 99, 184-191.

- Fantilli, A.P., Chiaia, B., 2013a. Golden ratio in the crack pattern of reinforced concrete structures. *ASCE Journal of Engineering Mechanics* 139(9), 1178-1184.
- Fantilli, A.P., Chiaia, B., 2013b. Eco-mechanical performances of cement-based materials: An application to self-consolidating concrete. *Construction and Building Materials* 40, 189-196.
- Fantilli, A.P., Chiaia, B., 2013c. The work of fracture in the eco-mechanical performances of structural concrete. *Journal of Advanced Concrete Technology* 11, 282-290.
- Fantilli, A.P., Chiaia, B., Gorino, A., 2016a. Minimum reinforcement and ductility index of lightly reinforced concrete beams. *Computers and Concrete* 18(6), 1175-1194.
- Fantilli, A.P., Chiaia, B., Gorino, A., 2016b. Fiber volume fraction and ductility index of concrete beams. *Cement and Concrete Composites* 65, 139-149.
- Fantilli, A.P., Chiaia, B., Gorino, A., 2016c. Unified Approach for Minimum Reinforcement of Concrete Beams. *ACI Structural Journal* 113(05), 1107-1116.
- Fantilli, A.P., Chiaia, B., Gorino, A., 2016e. Ecological and mechanical assessment of lightweight fiber-reinforced concrete made with rubber or expanded clay aggregates. *Construction and Building Materials* 127, 692-701.
- Fantilli, A.P., Ferretti, D., Iori, I., Vallini, P., 1999. Behaviour of R/C elements in bending and tension: the problem of minimum reinforcement ratio. *European Structural Integrity Society* 24, 99-125.
- Fantilli, A.P., Ferretti, D., Rosati, G., 2005. Effect of bar diameter on the behavior of lightly reinforced concrete beams. *ASCE Journal of Materials in Civil Engineering* 17(1), 10-18.
- Fantilli, A.P., Gorino, A., Chiaia, B., 2014. Precast plates made with lightweight fiber-reinforced concrete. In: *Proceedings of the FRC 2014 Joint ACI-fib International Workshop, Montreal (Canada)*, 224-234.
- Fantilli, A.P., Mihashi, H., Vallini, P., Chiaia, B., 2011. Equivalent Confinement in HPRCC Columns Measured by Triaxial Test. *ACI Materials Journal* 108, 159-167.

- Fantilli, A.P., Nemati, K.M., Chiaia, B., 2016d. Efficiency index for fiber-reinforced concrete lining at ultimate limit state. *Sustainable and Resilient Infrastructure* 1(1-2), 84-91.
- Fantilli, A.P., Vallini, P., 2003. Bond-slip relationship for smooth steel reinforcement. In: *Computational Modelling of Concrete Structures EURO-C 2003*, St. Johann Im Pongau (Austria), 215-224.
- Fayyad, T.M., Lees, J.M., 2015. Evaluation of a minimum flexural reinforcement ratio using fracture-based modelling, In: *Providing solutions to global challenges - Proceedings of the International Association for Bridge and Structural Engineering Conference IABSE2015*, Geneva (Switzerland), 735-742.
- Ferro, G., Carpinteri, A., Ventura, G., 2007. Minimum reinforcement in concrete structures and material/structural instability. *International Journal of Fracture* 146(4), 213-231.
- Gambarova, P.G., Rosati, G.P., 1996. Bond and splitting in reinforced concrete: test results on bar pull-out. *Materials and Structures* 29(5), 267-276.
- Ganjian, E., Khorami, M., Maghsoudi, A.A., 2009. Scrap-tyre-rubber replacement for aggregate and filler in concrete. *Construction and Building Materials* 23, 1828-1836.
- Giordano, L., Tondolo, F., 2011. Crack width evolution of R/C structures subject to corrosion and fatigue. *Key Engineering Materials* 452, 417-420.
- Giuriani, E., Plizzari, G.A., 1989. Propagation and distance of cracks in RC beams with a bending moment gradient. *Studi e Ricerche* 11, 61-106.
- Giuriani, E., Plizzari, G.A., 1998. Interrelation of splitting and flexural cracks in RC beams. *ASCE Journal of Structural Engineering* 124(9), 1032-1040.
- Gorino, A., Fantilli, A.P., Chiaia, B., Zampini, D., Guerini, A., Volpatti, G., 2016. Brittle vs. ductile behavior of concrete beams reinforced with steel rebars and fibers. In: *Proceedings of the 9th RILEM International Symposium on Fiber Reinforced Concrete BEFIB 2016*, Vancouver (Canada), 1263-1274.
- Grünewald, S., Bartoli, L., Ferrara, L., Kanstad, T., Dehn, F., 2014. Translation of test results of small specimens of flowable fibre concrete to structural behaviour:

- A discussion paper of fib Task Group 4.3. In: Proceedings of the FRC 2014 Joint ACI-fib International Workshop, Montreal (Canada), 555-564.
- Habert, G., Roussel, N., 2009. Study of two concrete mix-design strategies to reach carbon mitigation objectives. *Cement and Concrete Composites* 31, 397-402.
- Hededal, O., Kroon, I.B., 1991. Lightly Reinforced High-Strength Concrete. M.Sc. Thesis, University of Aalborg (Denmark).
- Hillerborg, A., Modéer, M., Petersson, P.E., 1976. Analysis of crack formation and crack growth in concrete by means of fracture mechanics and finite elements. *Cement and Concrete Research* 6(6), 773-781.
- International Federation for Structural Concrete (*fib*), 2000. *fib* Bulletin 10: Bond of Reinforcement in Concrete. *fib*, Lausanne (Switzerland).
- International Federation for Structural Concrete (*fib*), 2010. *fib* Bulletin, 57: Shear and punching shear in RC and FRC elements.” *fib*, Lausanne (Switzerland).
- International Federation for Structural Concrete (*fib*), 2012a. *fib* Bulletin 65-66: Model Code 2010 – Final Draft. *fib*, Lausanne (Switzerland).
- International Federation for Structural Concrete (*fib*), 2012b. *fib* Bulletin 67: Guidelines for Green Concrete Structures. *fib*, Lausanne (Switzerland).
- International Tunneling and Underground Space Association - Working Group 2 (ITA-WG2), 2000. Guidelines for the design of shield tunnel lining. *Tunnelling and Underground Space Technology* 15, 303-331.
- Jones, P.A., Austin, S.A., Robins, P.J., 2008. Predicting the flexural load-deflection response of steel fibre reinforced concrete from strain, crack-width, fibre pull-out and distribution data. *Materials and Structures* 41, 449-463.
- Kawai, K., Hoshino, S., Hirao, H., Tanaka, S., 2016. A study on an indicator for environmental impacts of cement industry. In: Proceedings of the 2nd International Conference on Concrete Sustainability ICCS16, Madrid (Spain), 884-890.

- Kormeling, H.A., Reinhardt, H.W., Shah, S.P., 1980. Static and Fatigue Properties of Concrete Beams Reinforced with Continuous Bars and with Fibers. *ACI Journal Proceedings* 77(1), 36-43.
- Kovar, M., Foglar, M., 2015. An analytical description of the force–deflection diagram of FRC. *Composites: Part B* 69, 550-561.
- Lange-Kornbak, D., Karihaloo, B.L., 1999. Fracture mechanical prediction of transitional failure and strength of singly-reinforced beams. *European Structural Integrity Society* 24, 31-66.
- Lee, M.K., Barr, B.I.G., 2004. A four-exponential model to describe the behaviour of fibre reinforced concrete. *Materials and Structures* 37, 464-471.
- Leonhardt, F., Mönnig, E., 1973. *Vorlesungen über Massivbau - Teil 1: Grundlagen zur Bemessung im Stahlbetonbau*. Springer-Verlag, Berlin (Germany).
- Levi, F., 1985. On minimum reinforcement in concrete structures. *ASCE Journal of Structural Engineering* 111(12), 2791-2796.
- Liao, L., de la Fuente, A., Cavalaro, S., Aguado, A., 2015. Design of FRC tunnel segments considering the ductility requirements of the Model Code 2010. *Tunnelling and Underground Space Technology* 47, 200-210.
- Liao, L., de la Fuente, A., Cavalaro, S., Aguado, A., 2016. Design procedure and experimental study on fibre reinforced concrete segmental rings for vertical shafts. *Materials and Design* 92, 590-601.
- Lim, T., Paramasivam, P., Lee, S., 1987. Behavior of Reinforced Steel-Fiber-Concrete Beams in Flexure. *ASCE Journal of Structural Engineering* 113(12), 2439-2458.
- Maldague, J.C., 1965. Établissement des Lois Moments-Courbures. *Annales de l'Institut Technique du Batiment et des Travaux Publics (ITBTP)* 213, 1170-1218.
- Massicotte, B., Faggio, L., Cordonni, N., Nour, A., Conciatori, D., 2014. Design and construction of SFRC bridge decks – Building on past experience and recent developments. In: *Proceedings of the FRC 2014 Joint ACI-fib International Workshop, Montreal (Canada)*, 134-153.

- McCormac, J.C., Brown, R.H., 2013. Design of reinforced concrete. Wiley, Hoboken, New Jersey (USA).
- Meda, A., Minelli, F., Plizzari, G.A., 2012. Flexural behaviour of RC beams in fibre reinforced concrete. *Composites: Part B* 43, 2930-2937.
- Meda, A., Rinaldi, Z., 2014. Steel fibers reinforcement for precast lining in tunnels with different diameters. In: *Proceedings of the FRC 2014 Joint ACI-fib International Workshop, Montreal (Canada)*, 522-531.
- Meda, A., Rinaldi, Z., Caratelli, A., Cignitti, F., 2016. Experimental investigation on precast tunnel segments under TBM thrust action. *Engineering Structures* 119, 174-185.
- Meng, G., Gao, B., Zhou, J., Cao, G., Zhang, G., 2016. Experimental investigation of the mechanical behavior of the steel fiber reinforced concrete tunnel segment. *Construction and Building Materials* 126, 98-107.
- Michels, J., Christen, R., Waldmann, D., 2013. Experimental and numerical investigation on postcracking behavior of steel fiber reinforced concrete. *Engineering Fracture Mechanics* 98, 326-349.
- Minelli, F., Plizzari, G., 2011. A New Round Panel Test for the Characterization of Fiber Reinforced Concrete: A Broad Experimental Study. *Journal of Testing and Evaluation* 39, 889-897.
- Minelli, F., Plizzari, G., 2015. Derivation of a simplified stress-crack width law for Fiber Reinforced Concrete through a revised round panel test. *Cement and Concrete Composites* 58, 95-104.
- Mobasher, B., Bakhshi, M., Barsby, C., 2014. Backcalculation of residual tensile strength of regular and high performance fiber reinforced concrete from flexural tests. *Construction and Building Materials* 70, 243-253.
- Mobasher, B., Yao, Y., Soranakom, C., 2015. Analytical solutions for flexural design of hybrid steel fiber reinforced concrete beams. *Engineering Structures* 100, 164-177.
- Mueller, H.S., Haist, M., Moffatt, J.S., Vogel, M., 2016. Environmental impact, performance and service lifetime - pillars of sustainable concrete construction. In:

- Proceedings of the 2nd International Conference on Concrete Sustainability ICCS16, Madrid (Spain), 23-34.
- Naaman, A.E., 2003. Strain hardening and deflection hardening fiber reinforced cement composites. In: Proceedings of the 4th Int. RILEM Workshop on High Performance Fiber Reinforced Cement Composites, Ann Arbor, Michigan (USA), 95-113.
- Naaman, A.E., Reinhardt, H.W., 2006. Proposed classification of HPFRC composites based on their tensile response. *Materials and Structures* 39(5), 547-555.
- Naaman, A.E., Shah, S.P., 1976. Pullout Mechanisms in Steel Fiber Reinforced Concrete. *ASCE Journal of the Structural Division* 102, 1537-1548.
- Najim, K. B. and Hall, M. R., 2010. A review of the fresh/hardened properties and applications for plain- (PRC) and self-compacting rubberised concrete (SCRC). *Construction and Building Materials* 24, 2043-2051.
- Nammur, G., Naaman, A.E., 1989. Bond Stress Model for Fiber Reinforced Concrete Based on Bond Stress-Slip Relationship. *ACI Materials Journal* 89(1), 45-57.
- Nilson, A., Darwin, D., Dolan, C., 2015. *Design of Concrete Structures*. McGraw-Hill Higher Education, Columbus, Ohio (USA).
- Ning, X., Ding, Y., Zhang, F., Zhang, Y., 2015. Experimental study and prediction model for flexural behavior of reinforced SCC beam containing steel fibers. *Construction and Building Materials* 93, 644-653.
- Oh, B. 1992. Flexural Analysis of Reinforced Concrete Beams Containing Steel Fibers. *ASCE Journal of Structural Engineering* 118(10), 2821-2835.
- Plizzari, G.A., Tiberti, G., 2006. Steel fibres as reinforcement for precast tunnel segments. *Tunnelling and Underground Space Technology* 21 (3-4), 438-439.
- Pouillon, S., Vitt, G., 2014. Hybrid concrete in heavy mat foundations. In: Proceedings of the FRC 2014 Joint ACI-fib International Workshop, Montreal (Canada), 511-521.

- Pujadas, P., Blanco, A., de la Fuente, A., Aguado, A., 2012. Cracking behavior of FRC slabs with traditional reinforcement. *Materials and Structures* 45, 707-725.
- Rao, G.A., Vijayanand, I., Eligehausen, R., 2008. Studies on ductility and evaluation of minimum flexural reinforcement in RC beams. *Materials and Structures* 41, 759-771.
- Rizk, E., Marzouk, H., 2011. Experimental Validation of Minimum Flexural Reinforcement for Thick HSC Plates. *ACI Structural Journal* 108(3), 332-340.
- Ruiz, G., Elices, M., Planas, J., 1999. Size effect and bond-slip dependence of lightly reinforced concrete beams. *European Structural Integrity Society* 24, 67-97.
- Said, M., Elrakib, T.M., 2013. Experimental verification of the minimum flexural reinforcement formulas for HSC beams. *International Journal of Civil Engineering and Technology* 4(5), 152-167.
- Salehian, H., Barros, J.A.O., 2015. Assessment of the performance of steel fibre reinforced self-compacting concrete in elevated slabs. *Cement and Concrete Composites* 55, 268-280.
- Salehian, H., Barros, J.A.O., 2017. Prediction of the load carrying capacity of elevated steel fibre reinforced concrete slabs. *Composite Structures* 170, 169-191.
- Salvador, R.P., Fernandes, J.F., de Figueiredo, A.D., 2015. Assessment of concrete reinforced with low content of fibres for structural purposes according to standard EN 14651-2007. *RevistaMatéria* 20(4), 961-974.
- Seguirant, S.J., Brice, R., Khaleghi, B., 2010. Making sense of minimum flexural reinforcement requirements for reinforced concrete members. *Precast/Prestressed Concrete Institute Journal* 55(3), 64-85.
- Shah, S.P., Swartz, S.E., Ouyang, C., 1995. *Fracture Mechanics of Concrete: Applications of Fracture Mechanics to Concrete, Rock and Other Quasi-Brittle Materials*. John Wiley & Sons, New York (USA).
- Siddique, R., Naik., T. R., 2004. Properties of concrete containing scrap-tire rubber – an overview. *Waste Management* 24, 563-569.

- Soetens, T., Matthys, S., 2014. Different methods to model the post-cracking behaviour of hooked-end steel fibre reinforced concrete. *Construction and Building Materials* 73, 458-471.
- Software e Servizi per l'Ingegneria (2S.I.), 2017. PRO_SAP - PROfessional Structural Analysis Program. Available from: <<http://www.2si.it/prosap.php>>.
- Swamy, R.N., Al-Ta'an, S.A., 1981. Deformation and Ultimate Strength in Flexure of Reinforced Concrete Beams Made with Steel Fiber Concrete. *ACI Journal Proceedings* 78(5), 395-405.
- Swiss Centre for Life Cycle Inventories, 2012. The Ecoinvent Database. Available from: <<http://www.ecoinvent.ch/>>.
- Tiberti, G., Minelli, F., Plizzari, G.A., 2014. Reinforcement optimization of fiber reinforced concrete linings for conventional tunnels. *Composites: Part B* 58, 199-207.
- Tiberti, G., Plizzari, G.A., 2008. Final concrete linings with optimized reinforcement. In: *Underground Facilities for better environment safety - Proceedings of the ITA-AITES World Tunnel Congress, Agra (India)*, 922-932.
- Timoshenko, S.P., Goodier, J.N., 1970. *Theory of Elasticity*. McGraw-Hill, New York (USA).
- Torroja, E., 1958. Statistical investigation of simple and compound bending tests. *CEB Bulletin d'Information* 9, Luxembourg, 1-21.
- Uchida, Y., Kawai, M., Rokugo, K., 2007. Back analysis of tensile stress-strain relationship of HPRCC. *Proceedings of the Fifth International RILEM Workshop on High Performance Fiber Reinforced Cement Composites, Mainz (Germany)*, 49-56.
- Vandewalle, L., 2000. Cracking behaviour of concrete beams reinforced with a combination of ordinary reinforcement and steel fibers. *Materials and Structures* 33, 164-170.
- Vidal, T., Castel, A., François, R., 2004. Analyzing crack width to predict corrosion in reinforced concrete. *Cement and Concrete Research* 34(1), 165-174.

- Wille, K., El-Tawil, S., Naaman, A.E., 2014. Properties of strain hardening ultra-high performance fiber reinforced concrete (UHP-FRC) under direct tensile loading. *Cement and Concrete Composites* 48 53-66.
- Winkler, A., Edvardsen, C., Kasper, T., 2014. Examples of bridge, tunnel lining and foundation design with steel fibre reinforced concrete. In: *Proceedings of the FRC 2014 Joint ACI-fib International Workshop, Montreal (Canada)*, 544-553.
- World Economic Forum (WEF), 2016. *Shaping the Future of Construction: A Breakthrough in Mindset and Technology*. Available from: <<https://www.weforum.org/>>.
- Wu, Y., 2002. Flexural Strength and Behavior of Polypropylene Fiber Reinforced Concrete Beams. *Journal of Wuhan University of Technology* 17(2), 54-57.
- Yasir Alam, S., Lenormand, T., Loukili, A., Regoin, J.P., 2010. Measuring crack width and spacing in reinforced concrete members. *Proceedings of the 7th International conference on Fracture Mechanics of Concrete and Concrete Structures FraMCoS-7*, 377-382.
- You, Z., Chen, X., Dong, S., 2011. Ductility and strength of hybrid fiber reinforced self-consolidating concrete beam with low reinforcement ratios. *Systems Engineering Procedia* 1, 28-34.
- Zhao, K., Janutolo, M., Barla, G., Chena, G., 2014. 3D simulation of TBM excavation in brittle rock associated with fault zones: The Brenner Exploratory Tunnel case. *Engineering Geology* 181, 93-111.

Notations

A_c	concrete cross-section of a member in bending;
A_{ct}	portion in tension of the concrete cross-section of a member in bending;
A_f	cross-sectional area of the fiber in an ideal tie [Figure 3.3(a)];
A_m	cross-sectional area of the cementitious matrix in an ideal tie [Figure 3.3(a)];
A_s	cross-sectional area of steel rebar in a concrete member;
A_s^*	trial cross-sectional area of steel rebar in a LRC member for the estimation of $A_{s,min}$ with Eq.(5.4).a;
$A_{s,eq}$	equivalent area of steel rebar corresponding to a certain V_f in a concrete member (Figure 3.1, Figure 4.2);
$A_{s,min}$	minimum cross-sectional area of steel rebar in a LRC member;
B	width of a concrete member cross-section;
C	resultant of the compressive stresses in a concrete cross-section at ultimate limit state (Figure 2.1, Figure 3.1, Figure 4.2);
c	concrete cover of steel rebar [Figure 2.3(a)];
c_{clear}	clear distance between the ribs of a steel rebar;
CF	carbon footprint of a concrete mixture [Eq.(7.2)];
d	effective depth of a concrete member cross-section (Figure 2.1);
DI	ductility index of a concrete member in bending [Eq.(1.6)];

DI_f	ductility index of a FRC member in bending containing V_f^* [Eq.(5.4).b];
DI_s	ductility index of a LRC member in bending containing A_s^* [Eq.(5.4).a];
$E_o \cdot A_o$	axial rigidity of the composite cross-section of an ideal tie [Eq.(3.6)];
$E_o \cdot I_o$	flexural rigidity of the composite cross-section of a concrete member [Eq.(2.5)];
E_c	tangent modulus of elasticity of concrete, at the origin of the stress vs. strain diagram [Figure 2.5(a)];
E_{c1}	secant modulus of elasticity of concrete, from the origin to the peak of compressive stress [Figure 2.5(a)];
EE	embodied energy of a concrete mixture [Eq.(7.2)];
E_f	modulus of elasticity of a fiber in an ideal tie;
EI	ecological index of a concrete mixture [Eq.(7.2)];
EI_{TLC_0}	upper bound value of the ecological index;
E_{lc}	tangent modulus of elasticity of lightweight concrete, at the origin of the stress vs. strain diagram;
E_{lc1}	secant modulus of elasticity of lightweight concrete, from the origin to the peak of compressive stress;
E_m	modulus of elasticity of the cementitious matrix in an ideal tie;
E_r	modulus of elasticity of the rock in BBT;
E_s	modulus of elasticity of steel rebar [Figure 2.5(b)];
f_c	cylindrical compressive strength of concrete;
f_{ct}	tensile strength of concrete;

f_{Ft}	residual tensile strength of FRC [Eq.(1.5)];
f_{fc}	cylindrical compressive strength of lightweight concrete;
$f_{lct,fl}$	flexural tensile strength of lightweight concrete;
f_R	residual tensile strength in a concrete cross-section containing fibers at ultimate limit state (Figure 3.1, Figure 4.2);
f_u	ultimate tensile strength of steel rebar or fibers;
f_y	yielding strength of steel rebar [Figure 2.5(b)];
G_F	fracture energy of concrete in tension;
H	depth of a concrete member cross-section;
h_w	cracked depth of a concrete member cross-section [Figure 2.3(a)];
i	subscript referred to the abscissa of a concrete member or ideal tie;
I_{FRC}	efficiency index of fiber-reinforcement in a concrete cross-section under combined axial and bending actions [Eq.(6.3)];
j	subscript referred to the vertical coordinate of a concrete member cross-section;
k	plasticity number of concrete [Eq.(2.12)];
k_{lc}	plasticity number of lightweight concrete;
L	span of a concrete member;
L_f	length of a fiber;
l_{tr}	transfer length of a concrete member or ideal tie (Figure 2.3, Figure 3.3);
M	internal bending moment acting on the cracked cross-section of a concrete member [Figure 2.3(d)];

M_1	internal bending moment acting on the Stage I cross-section of a concrete member [Figure 2.3(d)];
M_{cr}	first cracking bending moment of a concrete cross-section;
M_{cr*}	effective cracking bending moment of a concrete cross-section;
M_{Ed}	design value of the acting bending moment;
MI	mechanical index of a concrete mixture or member;
MI_1	mechanical index at material level;
MI_{1,TLC_0}	lower bound value of the mechanical index at material level;
MI_2	mechanical index at structural level in terms of strength;
MI_{2,TLC_0}	lower bound value of the mechanical index at structural level in terms of strength;
MI_3	mechanical index at structural level in terms of ductility;
M_{Rd}	design value of the resisting bending moment;
M_u	ultimate bending moment of a concrete cross-section;
$M_{u,1}, M_{u,2}$	negative resisting bending moments, for a given axial force, of concrete cross-sections [Eq.(6.3)];
$M_{u,2}$	ultimate bending moment of a concrete cross-section;
N	axial force acting on an ideal tie [Figure 3.3(a)];
n	number of strips in the depth of a concrete member cross-section;
N_{Ed}	design value of the acting axial force;
N_{Rd}	design value of the resisting axial force;
P	applied load of a concrete member in bending (Figure 1.1, Figure 6.1);
P_{cr}	first cracking load of a concrete member [Figure 1.1(b)];

P_{cr^*}	effective cracking load of a concrete member [Figure 1.1(b), Figure 6.1(b)];
P_d	design load of a concrete member;
p_f	cross-sectional perimeter of a fiber;
P_{max}	maximum load of a concrete member (Figure 1.2);
p_s	cross-sectional perimeter of steel rebar;
P_{sls}	service load of a concrete member (Figure 1.2);
P_u	ultimate load of a concrete member [Figure 1.1(b), Figure 6.1(b)];
r	normalized reinforcement ratio of a concrete member;
R	resultant of the cross-sectional stresses acting on a concrete member in bending [Eq.(2.8), Eq.(3.25)];
R_c	cubic compressive strength of concrete;
s	slip at the interface between concrete in tension and steel rebar or fiber in a member in bending or ideal tie;
s_0	slip in the cracked cross-section of a concrete member or ideal tie [Figure 2.3(b), Figure 3.3(b)];
s_1, s_2, s_3	limit values of s in the bond-slip models [Figure 2.6(b), Figure 3.4(b)];
SR	strength ratio of lightweight concrete [Eq.(7.1)];
T	resultant of the tensile stresses in a concrete cross-section at ultimate limit state (Figure 2.1, Figure 3.1);
T_{FRC}	resultant of the tensile stresses carried by the fiber-reinforcement in an HRC cross-section at ultimate limit state (Figure 4.2);
T_{LRC}	resultant of the tensile stresses carried by the steel rebar in an HRC cross-section at ultimate limit state (Figure 4.2);

V_f	fiber volume fraction in a concrete member;
V_f^*	trial fiber volume fraction in a FRC member for the estimation of $V_{f,\min}$ with Eq.(5.4).b;
$V_{f,\min}$	minimum fiber volume fraction in a FRC member;
w	crack width in a concrete member or ideal tie [Figure 2.4(a), Figure 3.3(a)];
W	section modulus of a member in bending;
\bar{w}	crack width at the bottom level of a concrete member [Figure 2.4(a), Figure 6.1(a)];
w_1, w_c	limit values of w in the cohesive models for cracked concrete [Figure 2.6(a), Figure 3.4(a)];
x	distance from the top edge to neutral axis in a concrete cross-section at ultimate limit state (Figure 2.1, Figure 3.1, Figure 4.2);
x_0	distance from the top edge to neutral axis in the cracked cross-section of a concrete member [Figure 2.4(a)];
x_1	distance from the top edge to neutral axis in Stage I cross-section of a concrete member [Figure 2.4(b)];
y	vertical coordinate of a concrete member cross-section [Figure 2.3(a), Figure 3.7(b)];
z	abscissa of a concrete member or ideal tie (Figure 2.3, Figure 3.3);
Z_{FRC}	internal lever arm of a FRC cross-section at ultimate limit state (Figure 3.1, Figure 4.2);
Z_{LRC}	internal lever arm of a LRC cross-section at ultimate limit state (Figure 2.1, Figure 4.2);
α	exponent in the bond-slip models [Eq.(2.17).a, Eq.(3.14).a];
β	coefficient in the bond-slip model for fibers [Eq.(3.14).b];

γ	partial safety factor in the design $DI - r$ relationships [Eqs.(5.5)]
γ_c	specific load of concrete;
γ_G	partial safety factor of dead loads;
γ_r	specific load of the rock in BBT;
γ_Q	partial safety factor of variable loads;
δ	midspan deflection of a concrete member in bending (Figure 1.1);
Δh	depth of the strips in a concrete member cross-section [Figure (3.7).b];
Δl	portion of the transfer length;
δ_{peak}	deflection at the maximum load of a FRC member (Figure 1.2);
δ_{sls}	deflection at the service load of a FRC member (Figure 1.2);
δ_u	ultimate deflection of a FRC member (Figure 1.2);
ε_c	concrete strain, or equivalent strain in cracked concrete [Eq.(3.23) and Eq.(6.1)], of a member in bending;
$\varepsilon_{c,0}$	concrete strain at level of reinforcement in the cracked cross-section of a member in bending [Figure 2.3(c)];
$\varepsilon_{c,1}$	concrete strain at level of reinforcement in the Stage I cross-section of a member in bending [Figure 2.3(c)];
ε_{c1}	concrete strain at the peak of compressive stress [Figure 2.5(a)];
ε_{ct}	concrete strain at the peak of tensile stress [Figure 2.5(a)];
ε_{cu}	ultimate equivalent strain in tension of a concrete cross-section under combined axial and bending actions [Figure 6.7(b)];
ε_f	strain of the fiber in an ideal tie;

$\varepsilon_{f,0}$	strain of the fiber in midsection of an ideal tie [Figure 3.3(c)];
$\varepsilon_{f,1}$	strain of the fiber in Stage I cross-section of an ideal tie [Figure 3.3(c)];
ε_{lc}	strain of a lightweight concrete in compression;
ε_{lc1}	strain at the peak of compressive stress of a lightweight concrete;
ε_m	strain of the cementitious matrix in an ideal tie;
$\varepsilon_{m,0}$	strain of the cementitious matrix in midsection of an ideal tie [Figure 3.3(c)];
$\varepsilon_{m,1}$	strain of the cementitious matrix in Stage I cross-section of an ideal tie [Figure 3.3(c)];
ε_s	strain of steel rebar in a member in bending;
$\varepsilon_{s,0}$	strain of steel rebar in the cracked cross-section of a member in bending [Figure 2.3(c)];
$\varepsilon_{s,1}$	strain of steel rebar in the Stage I cross-section of a member in bending [Figure 2.3(c)];
ε_u	ultimate strain of steel rebar [Figure 2.5(b)];
ε_y	yielding strain of steel rebar [Figure 2.5(b)];
ζ	slope of the proposed $DI - r$ linear functions [Eq.(1.7), Figure 1.3];
η	normalized compressive strain of concrete [Eq.(2.12)];
ϑ	coefficient of Eq.(4.6);
κ	coefficient of Eq.(1.5);
λ	strain at the origin of the coordinate y in a concrete cross-section of a member in bending [Figure 3.7(c)];

μ	curvature referred to a concrete cross-section of a member in bending [Figure 3.7(c)];
ν_c	Poisson's ratio of concrete;
ν_r	Poisson's ratio of the rock in BBT;
σ_c	concrete stress of a member in bending;
$\sigma_{c,0}$	stress of concrete in the cracked cross-section of a member in bending;
$\sigma_{c,max}$	maximum compressive stress in a concrete cross-section at ultimate limit state (Figure 2.1, Figure 3.1, Figure 4.2);
σ_f	stress of the fiber in an ideal tie;
$\sigma_{f,0}$	stress of the fiber in midsection of an ideal tie;
σ_{lc}	stress of a lightweight concrete in compression;
σ_m	stress of the cementitious matrix in an ideal tie;
$\sigma_{m,0}$	stress of the cementitious matrix in midsection of an ideal tie;
σ_s	stress of steel rebar in a concrete member in bending;
$\sigma_{s,0}$	stress of steel rebar in the cracked cross-section of a concrete member in bending;
τ	bond at the interface between concrete in tension and steel rebar or fiber in a member in bending or ideal tie;
τ_f, τ_{max}	limit values of τ in the bond-slip models [Figure 2.6(b), Figure 3.4(b)];
$\tau_{u,split}^2$	maximum value of τ in the bond-slip model for steel rebar in case of splitting failure [Figure(2.6).b];
ϕ_f	cross-sectional diameter of a fiber;

ϕ_s	nominal cross-sectional diameter of steel rebar;
χ	similarity coefficient of Eqs.(2.10);
ω	coefficient of Eq.(1.2).